FORMATION OF MAGNETIC MOMENTS IN SMALL GAS-PHASE CLUSTERS

Albert Diaz Bachs

FORMATION OF MAGNETIC MOMENTS IN SMALL GAS-PHASE CLUSTERS

PROEFSCHRIFT

ter verkrijging van de graad van doctor
aan de Radboud Universiteit Nijmegen
op gezag van de rector magnificus prof. dr. J.H.J.M. van Krieken,
volgens besluit van het college van decanen
in het openbaar te verdedigen op donderdag 4 april 2019
om 14:30 uur precies

door

Albert Diaz Bachs

geboren op 28 november 1983
te Barcelona

Promotor: Prof. dr. A. I. Kirilyuk

Manuscriptcommissie:

Prof. dr. J. Oomens   (voorzitter)

Prof. dr. V. Dupuis   (Claude Bernard University Lyon, Frankrijk)

Prof. dr. J. T. Lau   (Helmholtz-Zentrum Berlin, Duitsland)

Preface

This thesis is a resume of 4 and a half years of hard work, and closes one of the best chapters of my life. Besides work, I have had plenty of fun, even though sometimes it was a windy road, especially in the lab, where issues happened continuously, but it was all worth it, and this thesis is the proof of it. These lines are meant to thank everyone who has contributed one way or another.

Thanks Andrei for giving me the chance to join this awesome group, for always having your door open and for allowing me to make the living by playing with lasers, turbo-pumps and magnets...I enjoyed learning from you, especially in the lab, where the magic happens. Thanks Theo for being a good group leader. I still remember when I first came to Nijmegen, you asked me: "this is a hard PhD, are you sure to be willing to do so?" I was and after 4 years fighting the setup I am happy and proud I did. Thanks Alexey for the awesome party you gave after becoming professor. Thanks Huub for your advises.

Thanks to all the cluster Machotes. Thanks Dennis for your help, coding always should take half a millisecond! Thanks Luca for showing me how to tame the old chopper! Thanks Jeroen for your thesis, it was my main guide through this journey. Thanks to the Russian tank, Valeriy, I enjoyed a lot doing stuff together, even when you knocked my door one hour earlier than agreed and I was still in bed. Thanks Lars for helping me with theory and for translating me the Samenvatting, in return I taught you about jamón ibérico! I am glad to be colleagues at ASML. Thanks Remko for helping me with theory, besides I enjoyed a lot spending time with you abroad and discovering the funnier side of you. Maria, I hope you enjoyed your bachelor project, I wish you the best. From Joost I learned that is possible to enjoy the beach while working, that is to swim a bit and after it correct a paper while laying on the sun, legend.

I must thank all the technicians, without your help nothing would had been possible. Erwin, we spent a lot of time in the lab, thanks for all your help and fun. Thanks Tonnie for coming every time I needed help, you can build anything. Thanks Sergey for all your help with the lasers and for teaching me some 'nice' Russian words.

Thank you, Marilou, for all the help with paperwork and with settling. Listening to you singing made some of the colder days of winter a bit warmer.

I also would like to thank Prof. Misha Katsnelson, it was awesome to have such an impressive and renowned coauthor.

I would like to thank the manuscript committee members: Prof. Veronique Dupuis, Prof. Tobias Lau and Prof. Jos Oomens for taking their time to read this thesis and improve it with their comments.

Thanks Thomas for those 10 days in a summer-school in Romania, what can be better than 10 hours/day of magnetism with no air-co at 40 degrees? I enjoyed a lot, in return I introduced you to Steel Panther, you're welcome! You created terminology such as Jalapenhõ, so it was worth it losing a couple of times to you at the football table. Thanks to Qiao, who had to survive some months sitting

Contents

Contents

1 Introduction

In this chapter an introduction is given into clusters research. The first issue to address is to explain what are atomic clusters. Then it will be shown why cluster research is both intriguing and important. After that we will go through some examples of cluster research in different fields. The focus is set on the most relevant works on clusters magnetism, that directly relate to the main topic of this thesis. The last issue reviewed in this introduction is the interest to study doping in clusters, as the clusters are the smallest particles where the effects of doping can be studied and also because this will be a major part of this work. Finally the scope of the thesis is given.

1.1   What is a cluster and why are clusters interesting

In this thesis we will study the magnetic properties of clusters. The first issue to address, however, is to give a definition of a cluster, which is not trivial nor free of controversy. The easiest definition is that it is a bunch of atoms bonded somehow together, with sizes ranging from a couple of atoms to tens of thousands [1].

However this definition also applies for molecules, i.e. it can be argued both ways whether the famous so-called bucky ball, C_{60} [2], is a cluster or a molecule. So, what is it that makes a cluster different from a molecule? One can say that a molecule is sort of a finished product, as a molecule is a bunch of atoms chemically bonded together to attain chemical and electrical stability. While a cluster is in this case an unfinished product, often with open electronic shells, and as consequence they can be an extremely reactant entities only existing in the gas phase. Brought in contact with any surface or particle it will likely react and thus transform into something else, resulting in a significant change of its properties.

Next, one might guess what is the difference between a cluster and a nanoparticle and where is the crossover between the two. First, it is important to see that a cluster consisting of just a few atoms is typically smaller than a single nanometer. In other words, clusters are usually much smaller than the nanoparticles. While there is no delimitation between larger clusters and nanoparticles, in this thesis we will only study the smallest ones, the range where the subtraction or addition of a single atom can lead to strong changes of properties. This definitely does not apply to nanoparticles, as usually the radius, and not the number of atoms, is used to define the size of nanoparticles. And one last important distinction between clusters and nanoparticles is the approach. Nanoparticles are often considered as top-down approach, as their properties are followed in going smaller and smaller from the bulk limit. Opposite to this, gas-phase clusters are regarded as bottom-up approach, when one wants to see how the properties change while increasing size, from a single atom to tens or hundreds of them.

From a fundamental point of view, the main reason to study clusters is to gain a fundamental insight in the properties of matter in the transition regime. The atomic properties definitely belong to the quantum world. However, increasing the number of atoms leads to a gradual extinguishing of the quantum phenomena, to the merging of the electronic levels into bands and so on. Following this transition contributes to our understanding of electron and spin correlations, that govern the majority of phenomena characterizing the condensed matter. The large (dominating) fraction of surface atoms in clusters brings also certain peculiarities in their properties. Such processes as for example melting, always starts at the surface, this was studied theoretically by using the Lennard-Jones potential [3] and then experimentally demonstrated on lead surfaces [4]. This can strongly affect the thermodynamics of clusters.

From a technological point of view, the interest in clusters stems from the fact that nowadays, the miniaturization trends force us to create smaller and smaller elements for information technology, data storage, sensors, etc. Another import-

ant example where clusters may significantly contribute, is the understanding of catalysis on an atomic scale, and the design of catalysts [5, 6].

In this thesis we studied only gas phase clusters, by means of the well-known Stern-Gerlach technique [7, 8] adapted for cluster measurements. In 1920s, the magnetic deflection experiments of Ag atoms by O. Stern and W. Gerlach pointed out the existence of the electron spin, which brought new insights in the development of Quantum mechanics. In our experiment atomic beams are only used for calibration purposes. The main advantage to study the clusters in the gas phase is that they do not interact with any matrix, and thus are studied in a perturbation-free manner. Another advantage of this method is that many cluster sizes can be studied simultaneously in the very same experiment.

1.2 Clusters research: when and how it started

Clusters field is quite new and it took off not so long ago, as it started to be relevant in the 1960's. Nevertheless, the first examples of the use of clusters come from distant times. Probably the first example is calomel, Hg_2Cl_2, which was known in India already in the 12th century and later used to treat diseases and as a laxative for George III [9].

In the Middle Ages people already knew how to produce stained glasses for church windows, where Au, Ag and Cu clusters are present [10]. Rayleigh in the 19th century performed what could be the first investigation in clusters and revealed the secret behind color-changeable stained glasses due to light scattering by embedded small metal particles [11]. This was followed by Mie who proposed the study of clusters in 1908 using electrodynamics: "Gold atoms sure optically behave differently than small gold beads, so it would be very interesting to study their optical absorptions and track the process on how to build the gold particles from the atoms" [12].

But it was not before the 1960's when the real developments started. Some examples of these are the investigation on ionization potentials of alkali clusters [13] or the investigation of the electromagnetic properties of small metal particles in glasses [14].

And it was in the 1980's when cluster research really took off. Gas phase cluster sources were improved so they could produce clusters consisting in only few atoms. As a result, it was discovered that their properties are quite different from those of the bulk, causing a wave of interest. Among many directions, Knight et al. were pioneers in applying the famous Stern-Gerlach method to clusters, in order to study the magnetic properties of potassium clusters between 1 and 100 atoms [15].

A classic work of Knight et al. on sodium clusters has shown the relation of the cluster abundance spectra to their electronic shell structure. It was demonstrated that clusters with valence electrons that matched the spherical shell-closing numbers were produced more abundantly, that was called "magic numbers" [16], as
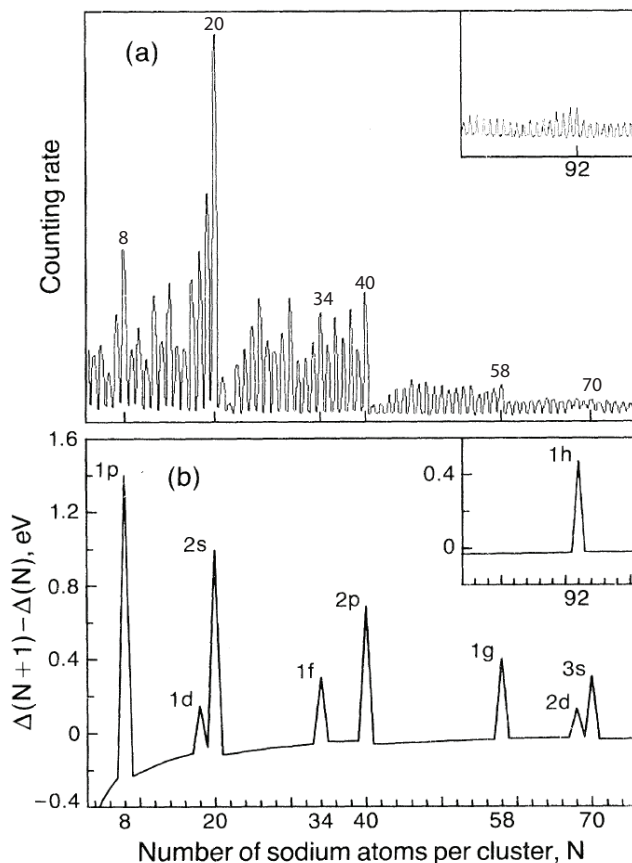
Figure 1.1: a) Mass spectrum of Sodium clusters, b) Calculated change in the electronic energy difference. [16].

shown in Fig. 1.1.

Similarly, the magic numbers were previously used to refer to xenon clusters by Echt et al. [17], where the closure was of geometrical reason. At the same time, Smalley group developed and improved their source, which was of capital importance in the field [18]. In 1984, Ekardt predicted a shell model for metal clusters [19] using jellium approach adopted from nuclear shell theories in which the cluster was considered to be a uniformly positive charged ionic sphere core filled with delocalized valence electrons. The jellium model happened to be useful even for clusters containing several thousand atoms [20].

Since then, cluster research has been widened and spread to various areas. Lots of studies focused on the structure of clusters [21, 22]. Another interesting and complementary subfield in cluster research is the electronic properties, for
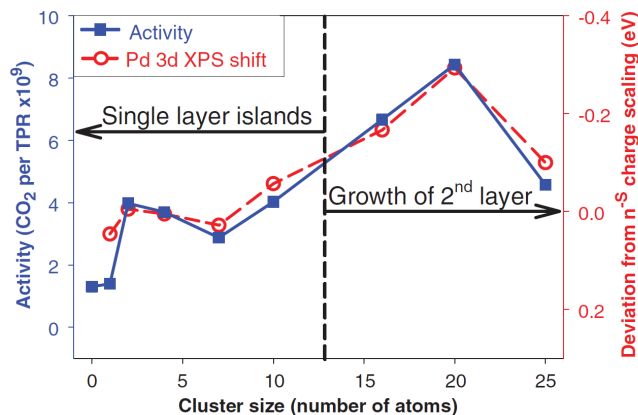
Figure 1.2: CO oxidation activity observed during temperature-programmed reaction (TPR) (left axis, solid squares) compared with shifts in the Pd 3d binding energy, relative to expectations from smooth bulk scaling (right axis, open circles), as a function of cluster size. [27].

example the work of Busani et al. who studied the band-gap closure in Hg clusters [23]. Interesting phenomena on the junction of the two, such as phonon-electron coupling, have also been addresses for clusters [24].

From the point of view of applications, the catalytic properties of clusters are of course a hot topic within the cluster research, as such studies allow to understand the fundamental properties of catalysis [25, 26]. For instance the catalytic activity of Pd clusters proved to be size dependent, also adsorbed on TiO_2 [27], as shown in Fig. 1.2.

1.3 Magnetism in clusters

The research on clusters magnetism started in the late 70's of the last century. As previously mentioned, Knight et al. were pioneers in applying the old Stern-Gerlach technique to clusters [15]. The magnetic moment of potassium atom is 1 μ_B, as it was already measured half a century earlier by Taylor [28] and can easily be derived from Hund's rules. That a similar behavior could be observed in clusters, came as a surprise.

For bulk matter, everything is much more complicated. The magnetic moments per atom are usually significantly decreased compared to the atomic values. The orbital contribution is in most cases quenched. Regarding spin magnetic moments, their values are also decreased, and the main reasons for such decrease is the increase in the coordination number. For instance, iron atom has an atomic magnetic moment of 6 μ_B, 4 μ_B are due to its spin magnetic moment while the

remaining 2 μ_B come from the orbital contribution. In contrast, in the bulk, its magnetic moment is just 2.2 μ_B per atom [29]. The non-integer magnetic moment is a consequence of partial delocalization of the 3d electrons [30].

When talking about magnetic materials, Fe and Co usually are the first elements to come to our thought. This is because together with Ni they are the most common magnetic materials. Therefore, several groups studied the magnetic properties of clusters made from these elements. Among them, probably the most relevant work is the one from Billas et al. [31], which proved that even for clusters containing about 700 atoms, the magnetic moments per atom for these three materials are larger than those of the bulk.
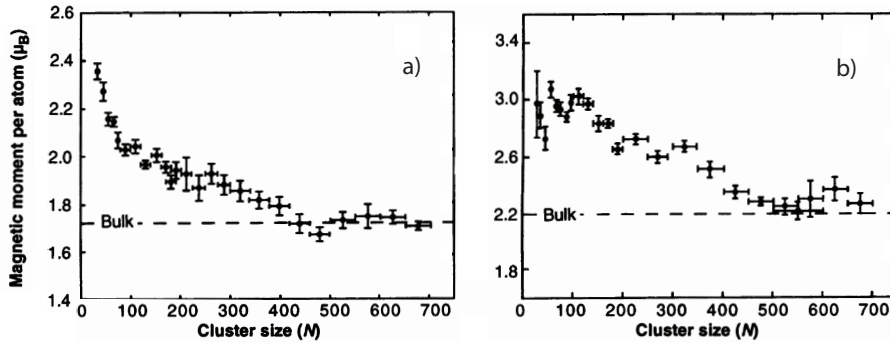
Figure 1.3: Magnetic moments of a) Co and b) Fe clusters. Adapted from Billas et al. [31].

In Fig. 1.3 it is shown that both Co and Fe clusters exhibit considerably higher magnetic moments per atom than for the bulk. Similar results were found for Ni. This triggered research on magnetism in clusters, particularly related to transition metals, in order to understand the crossover between the large magnetic moments of free atoms and the lower bulk values. Several studies focused on the magnetic properties of such materials [32–36].

But not only originally magnetic materials have been studied. For example, rhodium is paramagnetic in the bulk, but it was found to be magnetic for small clusters [37, 38].

Later, also the magnetic properties of rare earth clusters have been studied [39, 40]. Note that because of their tiny sizes, magnetocrystalline anisotropy is not sufficient to hold the magnetization of the clusters fixed to the crystal frame. Therefore, all (or practically all) of the studied clusters are superparamagnetic, at all used temperatures (typically ≥25 K). An exception to this can sometimes be seen in rare-earth clusters, such as Tb [41].

1.4   Doping in clusters

Doping of host materials has been widely used in the semiconductor technology since the early stages. The electronic states of the dopants are of utmost importance in the operation of semiconductor devices, from old-time transistors and to the multi-core processors of our days. The low dimensionality of clusters and the discrete electronic structure related to this, makes the study of the dopant states in clusters a particularly intriguing topic. The effect of the impurity on the lattice or vice-versa, can be studied at the most fundamental level. Further, gas phase clusters deflection experiments allow the study of the effect of the doping as function of the exact cluster size, and related to the evolution of a certain property.

In an example particularly relevant to the study in this thesis, Hirsch et al. recently investigated the magnetic properties of Cr doped Au ionized clusters [42]. They elegantly related the existence of a local magnetic moment on the Cr impurity with the energy gap of the Au_n host in the geometry of $CrAu_n^+$. In other words, a large energy gap in the host is translated in large spin magnetic moment of the impurity. In contrast, the clusters with a smaller gap have a partially quenched magnetic moment. Further they have shown that the smaller the Cr-Au interaction, the larger is the magnetic moment, as can be seen in Fig. 1.4.

Yin et al. studied the effects of doping bismuth clusters with manganese [43]. While pure Bi clusters show weak magnetism for odd-numbered clusters and a total absence of net magnetic moment for even-numbered clusters, the addition of a single Mn atom or more, resulted in clear magnetic properties. The local magnetic moments of Mn atoms in these clusters are inferred to be about 3 μ_B. Hence they concluded that the Bi atoms affect the magnetism in $Bi_N Mn_M$ clusters in two ways: either they bond with Mn atoms covalently and change their local magnetic moment, or they affect the inter-atomic distances between the Mn atoms which in turn affects the magnetic order.

Rohrmann et al. studied in detail the magnetic and electric properties of Mn doped Sn clusters [44, 45]. They found size dependent magnetic moments and a crucial contribution of molecular vibrations to the spin relaxation in $Mn@Sn_{12}$. In its vibrationally ground state the cluster behaves magnetically like a paramagnetic atom, with quantized spin states. However, excited molecular vibrations induce spin orientation in the magnetic field, as can be seen in Fig. 1.5.

In parallel to the experiments, and more often even ahead of them, theoretical research on clusters gained a very broad popularity. Related to the cases of doped clusters, Yuan et al. employing first-principles methods, reported the ground state geometric and electronic structures of gold clusters doped with platinum group atoms, $Au_N M$ (N=1-7, M=Ni, Pd, Pt) [46]. The stability and electronic properties of Ni-doped gold clusters were found to be similar to that of pure gold clusters with an enhancement of bond strength. Due to the strong $d - d$ or $s - d$ interplay between impurities and gold atoms originating in the relativistic effects and unique properties of dopant delocalized s-electrons in Pd- and Pt-doped
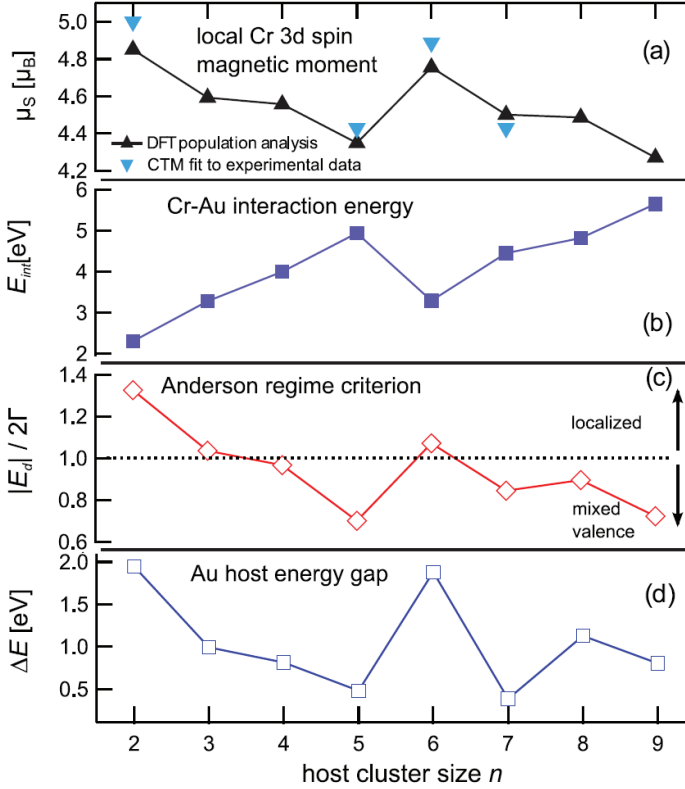
Figure 1.4: (a)Local spin magnetic moments of Cr 3d in Au_nCr^+ cluster, from DFT analysis (black upwards triangles) and experimental data (blue downwards triangles). (b) Cr-Au interaction energy. (c) Anderson regime criterion $|E_d|/2\Gamma$. (d) energy gap of the Au_n host in the geometry of Au_nCr^+. Adapted from Hirsch et al. [42].

gold clusters, the dopant atoms markedly change the geometric and electronic properties of gold clusters, including the bond energies.

Häkkinen et al. studied gold clusters on oxide surfaces, proving the former to exhibit unique catalytic activity [47]. Moreover, if doped with strontium, the nanocatalytic properties of these clusters were shown to drastically increase.

1.5 Outline of this thesis

The goal of this thesis is to gain fundamental understanding of the magnetic properties of transition metal and rare earth clusters. In particular, we would
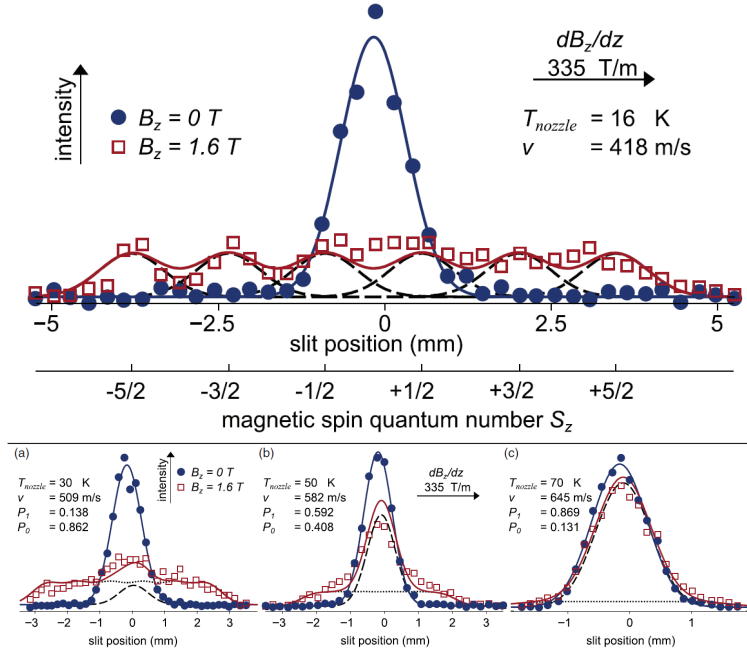
Figure 1.5: Magnetic deflections of Mn@Sn$_{12}$. Top figure shows deflection at 16 K, while a) shows deflection at 30 K, b) at 50 K and c) at 70 K. Adapted from Rohrmann et al. [44].

like to address the effects of doping. The nature of doping can be of two different kinds. The first is to dope a paramagnetic/non-magnetic material with a magnetic impurity and to study its effect on the host, while the second consists of doping a ferromagnetic material with an impurity which is not magnetic and study the influence of the impurity on the magnetic interactions in the host.

In Chapter 2 a detailed description of the experimental techniques and setups used for this research is provided.

In Chapter 3 the magnetic properties of vanadium, niobium and tantalum clusters are studied. The atomic-like deflection patterns will be discussed using the Kramers degeneracy theorem. Furthermore it will be shown that the quantum relaxation processes of both Raman and Orbach type can also be studied in these quasi-macroscopic systems.

In Chapter 4 the magnetic properties of cobalt doped niobium and vanadium clusters are studied. Magnetic deflection experiments were used to determine the magnetic moments of these clusters. We established the ground state geometry of the clusters by experimentally obtaining their vibrational spectra in collaboration with the Free Electron Laser for Infra-red eXperiments (FELIX) facility, and then comparing them with a density functional theory study in collaboration with the

Theory of Condensed Matter department. Using these results, we discussed the behavior from the point of view of the Anderson impurity model and the Kondo effect.

In Chapter 5 the magnetic properties of terbium doped vanadium and niobium clusters are studied. The results are quite different from the ones obtained in the previous chapter, despite of the same host material, which is clearly due to the different electronic states of Tb, and thus impossibility of both hybridization with matrix and Kondo screening.

In Chapter 6 the magnetic properties of oxygen doped samarium clusters are studied. Samarium does not possess a magnetic moment in its atomic ground state. In the bulk, however, trivalent Sm is magnetic. Recent theory has shown a possible transition from non-magnetic divalent to magnetic trivalent state when clusters become larger than 8 atoms. While the goal of our research was the experimental verification of these predictions, only clusters containing a single oxygen dopant were observed. Probably because of this, magnetic behavior was different from the predicted one.

In Chapter 7 the magnetic properties of pure Co clusters were compared to the Rh doped ones. The combination of the two metals can be interesting from the point of view of novel magnetic materials, as Co has large magnetic moment, while Rh has a large spin-orbit coupling that should result in strong magnetic anisotropy. We would also like to compare the behavior of neutral clusters with a recent study on the $Co_n Rh$ cations. The results on the neutrals happen to be quite different from those on cations.

The thesis is concluded with a summary as well as an outlook for future experiments and other developments on this subject.

References

[1] A. W. Castleman and S. N. Khanna, "Clusters, Superatoms, and Building Blocks of New Materials," J. Phys. Chem. **113**, 2664 (2009).

[2] R. F. Curl and R. E. Smalley, "Probing C_{60}," Science **244**, 1017 (1988).

[3] J.-P. Hansen and L. Verlet, "Phase Transitions of the Lennard-Jones System," Phys. Rev. **184**, 151 (1969).

[4] J. W. M. Frenken and J. F. van der Veent, "Observation of Surface Melting," Phys. Rev. Lett. **54**, 134 (1985).

[5] S. N. Khanna and A. W. Castleman *Quantum Phenomena in Clusters and Nanostructures*, (Springer, Berlin 2003).

[6] M. Karkare, *Nanotechnology Fundamentals and Applications*, (I. K. International Publishing House Pvt. Ltd., New Delhi, 2008).

[7] W. Gerlach and O. Stern, "Das magnetische Moment des Silberatoms," Z. Phys. A. **9**, 353 (1922).

[8] O. Stern and W. Gerlach, "über die richtungsquantelung im magnetfeld," Ann. Phys. **74**, 673 (1924).

[9] www.wikipedia.org

[10] U. Kreibig and M. Vollmer, *Optical Properties of Metal Clusters*, (Springer-Verlag Berlin Heidelberg, 1995).

[11] J. Strutt *On the scattering of light by small particles*, (Philosophical Magazine 41(4) 447-454, 1871).

[12] G. Mie, "Beiträge zur Optik trüber Medien," Ann. Phys. **25**, 377 (1908).

[13] P. J. Foster, R. E. Leckenby, and E. J. Robbins, "The ionization potentials of clustered alkali metal atoms," J. Phys. B: Atom. Mole. Phys. **2**, 478 (1969).

[14] U. Kreibig, "Kramers Kronig Analysis of the Optical Properties of Small Silver Particles," Z. Phys. **234**, 307 (1970).

[15] W. D. Knight, R. Monot, E. R. Dietz, and A. R. George, "Stern-Gerlach Deflection of Metallic-Cluster Beams," Phys. Rev. Lett. **40**, 1324-1326 (1978).

[16] W. D. Knight, K. Clemenger, W. A. de Heer, W. A. Saunders, M. Y. Chou, and M. L. Cohen, "Electronic Shell Structure and Abundances of Sodium Clusters," Phys. Rev. Lett. **52**, 2141 (1984).

[17] O. Echt, K. Sattler, and E. Recknagel, "Magic Numbers for Sphere Packings: Experimental Verification in Free Xenon Clusters," Phys. Rev. Lett. **52**, 1121 (1981).

[18] T. G. Dietz, M. A. Duncan, D. E. Powers, and R. E. Smalley, "Laser production of supersonic metal cluster beams," J. Chem. Phys. **74**, 6511 (1981).

[19] W. Ekardt, "Dynamical Polarizability of Small Metal Particles: Self-Consistent Spherical Jellium Background Model," Phys. Rev. Lett. **52**, 19251 (1984).

[20] J. L. Persson, R. L. Whetten, H.-P. Cheng, and R. S. Berry, "Evidence for

quantized electronic level structure for 100-1300 electrons in metal-atomic clusters," Chem. Phys. Lett. **186**, 215 (1991).

[21] A. Fielicke, A. Kirilyuk, C. Ratsch, J. Behler, M. Scheffler, G. von Helden, and G. Meijer, "Structure Determination of Isolated Metal Clusters via Far-Infrared Spectroscopy," Phys. Rev. Lett. **93**, 023401 (2004).

[22] P. Gruene, D. M. Raymer, B. Redlich, A. F. G. van der Meer, J. T. Lyon, G. Meijer, and A. Fielicke, "Structures of Neutral Au_7, Au_{19} and Au_{20} Clusters in the Gas Phase," Science **321**, 674 (2008).

[23] R. Busani, M. Folkers, and O. Cheshnovsky, "Direct Observation of Band-Gap Closure in Mercury Clusters," Phys. Rev. Lett. **81**, 3836 (1998).

[24] V. Chernyy, R. Logemann, J. M. Bakker, and A. Kirilyuk, "The repopulation of electronic states upon vibrational excitation of niobium carbide clusters," J. Chem. Phys. **145**, 024313 (2016).

[25] S. Vajda, M. J. Pellin, J. P. Greeley, C. L. Marshall, L. A. Curtiss, G. A. Ballentine, J. W. Elam, S. Catillon-Mucherie, P. C. Redfern, F. Mehmood, and P. Zapol, "Subnanometre platinum clusters as highly active and selective catalysts for the oxidative dehydrogenation of propane," Nat. Mate. **8**, 213-216 (2009).

[26] O. Lopez-Acevedo, K. A. Kacprzak, J. Akola, and H. Häkkinen, "Quantum size effects in ambient CO oxidation catalysed by ligand-protected gold clusters," Nat. Chem. **2**, 329-334 (2010).

[27] W. E. Kaden, T. Wu, W. A. Kunkel, S. L. Anderson, "Electronic structure controls reactivity of size-selected Pd clusters adsorbed on TiO_2 surfaces," Science **326**, 826 (2009).

[28] J. B. Taylor, "Magnetic Moments of the Alkali Metal Atoms," Phys. Rev. **28**, 576 (1926).

[29] M. B. Stearns, *in Magnetische Eigenschaften von Metallen*, Landolt and Börnstein, (Springer-Verlag, Berlin, 1986), New Series Ill/1 9a, p. 24.

[30] D. C. Mattis, *The Theory of Magnetism*, (Springer-Verlag, Berlin, ed. 2, 1988).

[31] I. M. Billas, A. Châtelain, and W. A. de Heer, "Magnetism from the atom to the bulk in iron, cobalt, and nickel clusters," Science **265**, 1682 (1994).

[32] J. P. Bucher, D. C. Douglass, and L. A. Bloomfield, "Magnetic Properties of

Free Cobalt Clusters," Phys. Rev. Lett. **66**, 3052 (1991).

[33] S. E. Apsel, J. W. Emmert, J. Deng, and L. A. Bloomfield, "Surface-Enhanced Magnetism in Nickel Clusters," Phys. Rev. Lett. **76**, 1441 (1996).

[34] F. W. Payne, W. Jiang, J. W. Emmert, J. Deng, and L. A. Bloomfield, "Magnetic structure of free cobalt clusters studied with Stern-Gerlach deflection experiments," Phys. Rev. B **75**, 094431 (2007).

[35] S. Peredkov, M. Neeb, W. Eberhardt, J. Meyer, M. Tombers, H. Kampschulte and G. Niedner-Schatteburg, "Spin and Orbital Magnetic Moments of Free Nanoparticles," Phys. Rev. Lett. **107**, 233401 (2011).

[36] M. Niemeyer, K. Hirsch, V. Zamudio-Bayer, A. Langenberg, M. Vogel, M. Kossick, C. Ebrecht, K. Egashira, A. Terasaki, T. Möller, B. v. Issendorff and J. T. Lau, "Spin Coupling and Orbital Angular Momentum Quenching in Free Iron Clusters," Phys. Rev. Lett. **108** 057201 (2012).

[37] A. Cox, J. Louderback, and L. Bloomfield, "Experimental observation of magnetism in rhodium clusters," Phys. Rev. Lett. **71**, 923-926 (1993).

[38] L. Ma, R. Moro, J. Bowlan, A. Kirilyuk, and W. A. de Heer, "Multiferroic Rhodium Clusters," Phys. Rev. Lett. **113**, 157203 (2014).

[39] C. N. van Dijk, Th. Rasing, A. Kirilyuk, J. Bowlan, A. Liang, and W. A. de Heer, "The effect of oxygen doping on the magnetism of Tb and Pr clusters," J. Appl. Phys. **107**, 09B526 (2010).

[40] L. Peters, I. Di Marco, M. S. Litsarev, A. Delin, M. I. Katsnelson, A. Kirilyuk, B. Johansson, B. Sanyal, and O. Eriksson, "Valence and spectral properties of rare-earth clusters," Phys. Rev. B **92**, 035143 (2015).

[41] L. Peters, S. Ghosh, B. Sanyal, Ch. van Dijk, J. Bowlan, W. de Heer, A. Delin, I. Di Marco, O. Eriksson, M. I. Katsnelson, B. Johansson, and Andrei Kirilyuk, "Magnetism and exchange interaction of small rare-earth clusters; Tb as a representative," Sci. Rep. **6**, 19676 (2016).

[42] K. Hirsch, V. Zamudio-Bayer, A. Langenberg, M. Niemeyer, B. Langbehn, T. Möller, A. Terasaki, B. v. Issendorff, and J. T. Lau, "Magnetic Moments of Chromium-Doped Gold Clusters: The Anderson Impurity Model in Finite Systems," Phys. Rev. Lett. **114**, 087202 (2015).

[43] S. Yin, X. Xu, R. Moro, and W. A. de Heer, "Measurement of magnetic moments of free $Bi_N Mn_M$ clusters," Phys. Rev. B **72**, 174410 (2005).

[44] U. Rohrmann, and R. Schäfer, "Stern-Gerlach Experiments on Mn@Sn$_{12}$: Identification of a Paramagnetic Superatom and Vibrationally Induced Spin Orientation," Phys. Rev. Lett. **111**, 133401 (2013).

[45] U. Rohrmann, P. Schwerdtfeger, and R. Schäfer, "Atomic domain magnetic nanoalloys: interplay between molecular structure and temperature dependent magnetic and dielectric properties in manganese doped tin clusters," Phys. Chem. Chem. Phys. **16**, 23952 (2014).

[46] D. W. Yuan, Y. Wang, and Z. Zenga, "Geometric, electronic, and bonding properties of Au$_N$M (N=1-7, M=Ni, Pd, Pt) clusters," J. Chem. Phys. **122**, 114310 (2005).

[47] H. Häkkinen, S. Abbet, A. Sánchez, U. Heiz, and U. Landman, "Structural, Electronic, and Impurity-Doping Effects in Nanoscale Chemistry: Supported Gold Nanoclusters," Angw. Chem. **42**, 1297-1300 (2003).

2 Experimental details

To study various properties of clusters, experiments of different nature need to be carried out. In order to understand the electronic properties the photoelectron spectra are required; to derive the geometrical conformation of the clusters we need their vibrational spectra. In order to obtain the net magnetic moments there are two options. The first one is to perform Stern-Gerlach deflection experiments on gas phase clusters, which allows to obtain the total net moments of neutral clusters, without making any distinction between spin magnetic moment and orbital one. The second option is to perform X-ray magnetic circular dichroism (XMCD), which allows to obtain the spin and orbital contributions separately, but can only be applied to charged clusters (cations). Thus, both methods have their limitations and their advantages.

The main aim of this thesis is to study the magnetic properties of small clusters, comparing their sizes. The technique used in this thesis is therefore the Stern-Gerlach deflection of cluster beam. The reason why this technique is used is because it offers the chance to study in one single experiment a broad distribution of clusters. Further we used the Free Electron Laser to measure the vibrational spectra of clusters that are further used to determine their geometrical structure.

2.1 Stern-Gerlach deflection setup: Overview

The experimental setup used in this thesis for the magnetic deflection measurements, consists of several parts. The operation of the setup is pulsed at 10 Hz repetition rate, which makes the timing scheme an important issue. Here, we look briefly at what the separate parts are, and in the following discuss them in more details.

In our experiments, the clusters are formed by means of laser ablation of a metal target rod. The ablation laser used is a Nd:YAG-laser which frequency is doubled to emit at 532 nm, with pulses of energy ranging between 5 and 40 mJ. The vaporized material interacts with the He carrier gas, condensing and forming clusters. Afterwards the mixture supersonically expands into the vacuum. The cluster cloud then passes through a skimmer.

Right after this, there is a small chamber where we have a simple time of flight (TOF) mass-spectrometer. Its mission is to assist the optimization of the cluster signal as close as possible to the source. It is important to notice that this TOF can only detect cations, as there is no laser to ionize the clusters here. Even though the conditions to create cations and neutral clusters might differ, it gives a good starting point for finding the signal.

After it at the very end of the same chamber there is a mechanical chopper. The chopper has two functions. The first one is to measure the velocity of the clusters, to be able to evaluate the magnetic moments from the deflections. The second mission is the velocity selection.
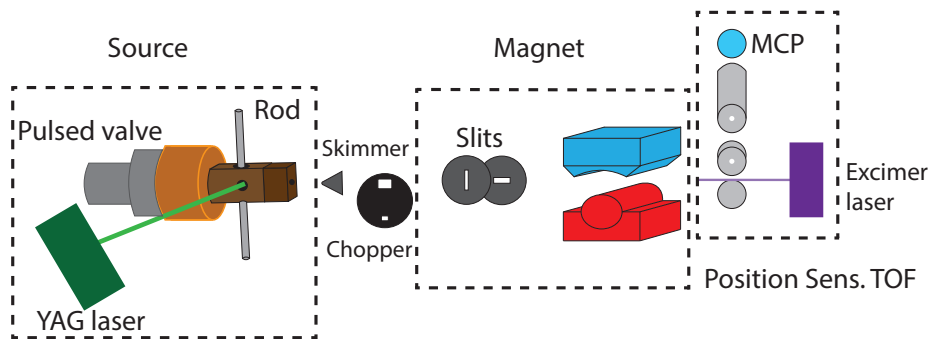
Figure 2.1: General overview of the setup. The clusters are formed in the source by laser ablation of rod target, and injection of cold He gas. Afterwards the cluster beam is skimmed. The chopper is used to select and measure the velocity of the clusters. Before entering the deflection magnet, the cluster beam is shaped using two slits. 80 cm after the magnet, clusters enter the ionization region in the time of flight spectrometer (TOF), where they are ionized by an excimer laser at 193 nm wavelength.

In our experiment, next, the clusters are deflected in a gradient magnetic field, created by an electromagnet. After interacting with the magnet, the clusters fly for another 0.8 m, before entering the position sensitive time of flight mass spectrometer (PSTOFMS), the 3rd and last part of the setup.

2.2 The source
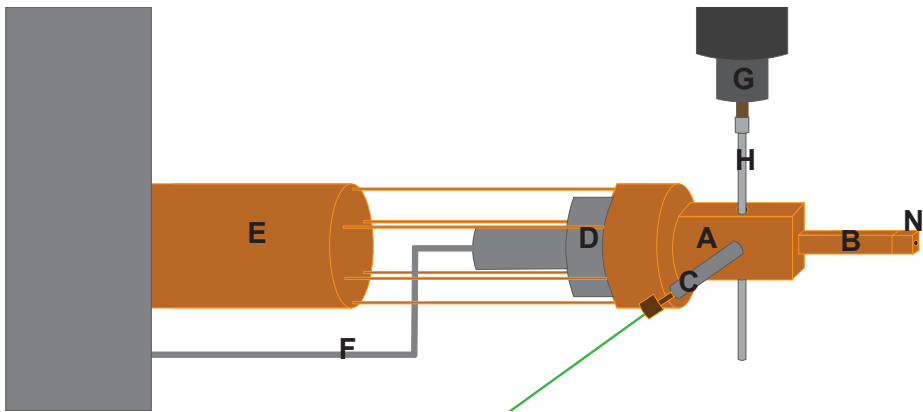
Figure 2.2: General overview of the cluster source. A is the main block where the cluster formation takes place. B is the extension tube where the nozzle, N, is located at its end. C is the tube where the YAG laser is focused through; inside of it, a small chamber is located where the clusters are formed. D is the pulsed valve; E is the cold head; F is the tube connected to the carrier gas tank; G is the stepper motor; H is the rod.

The construction of our source is shown in Fig. 2.2. A previously mentioned, the method used to create clusters is laser ablation of target metal. The reason to use this technique instead of others such as sputtering, ion bombardment or electric arc, is because it offers the possibility to create clusters of any desired material.

The first ablation sources mainly consisted of a mirror to focus the laser beam into a target [1]. These sources were further developed by confining the laser ablated plume in a small cavity filled with a carrier gas, which can cool down the plume and assist the nucleation of clusters. Among these sources the design from Smalley [2] was one of the most successful ones. In it, the target material was located near the nozzle of the pulsed valve in a straight channel. The main disadvantage of this source for our purposes is that in it a poor thermalization of the clusters is achieved. This design was improved by the addition of a waiting chamber where the clusters can nucleate and thermalize with the source before

leaving the cavity through the nozzle [3]. This new source had a small exit nozzle which restricts the flow of gas and helps to keep a higher pressure in the cavity.

The design of our source is similar to the one of Fielicke et al. [4]. It was chosen because of its capability of cooling down the clusters, while creating clusters in the size range which we are interested in. Our source is shown in Fig. 2.3. The main part of the source, the block A, holds the target rod and has entry holes for the ablation laser and the gas pulse. It is in this block where the vaporization and expansion of the cluster plume take places. The entry of the carrier gas has a diameter of 1.5 mm. The volume of the cavity can be varied according to the needs of the experiment, but the standard value is 0.2 cm^3 (4 mm x 15 mm).

An extension tube can be attached to the main block tube A, B in Fig. 2.3, whose role is to make the clusters travel longer time inside the cold source, for better thermalization [5]. The length of the available extension tubes range from 10 mm to 60 mm. At the end of the extension tube there is a bi-angle nozzle, N in Fig. 2.3, which is responsible for the supersonic expansion into the vacuum; the nozzle has two different angles in order to achieve the best expansion, the inner one has 90 degrees, while the outer one is up to 45 degrees, as there are several available, but the typically used has an angle of 30 degrees. These two angles are also parameters of importance in order to study the magnetic properties, which again will be discussed in chapter 3. D is the pulsed valve for He gas, produced by General Valve (Parker series 9).
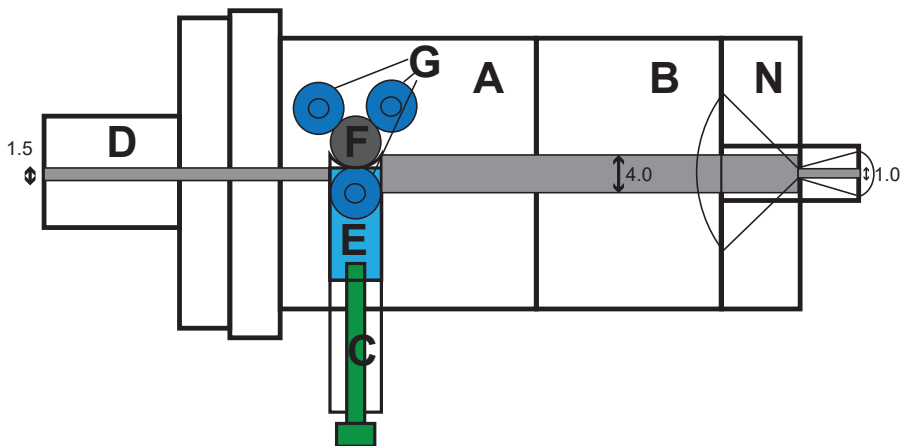
Figure 2.3: Top view of the source. A is the block where everything is coupled to. B is the extension tube. The nozzle, N, is located on its end; both angles can be changed, the one closest to the rod can be up to 90 degrees, while the exit one can be up to 45 degrees. D is the pulsed valve. C is the plunger where the YAG beam impinges. E is a separate chamber inside the plunger. G are the screws which are responsible to fix the rod to keep it rotating.

The opening time of the valve, which has a typical pulse width of 1 ms and the pressure of the carrier gas, which in the setup can achieve values between 0 and 6.4 bar, are both very important parameters for the operation of the source. It is interesting to note that the most important part of the inner valve is the poppet, the tip of which is ultimately responsible for closing and opening the valve. The poppet is made of Vespel, which is a suitable material to work at cryogenic temperatures, in the order of 25 K, as it does not deform much with temperature.

In order to avoid too much play of the rod while rotating, or the rod to get stuck, there are three screws coupled to springs, G, which assist the rotation of the rod.

The pressure in the source chamber is around 5×10^{-7} mbar when the setup is not running; while running the pressure is increased usually to around 8×10^{-5} mbar.

2.2.1   Temperature of the source: Closed-cycle refrigerator

For the purposes of deflection experiment, it is of capital importance to be able to carry it out at low temperatures. First, at low temperature a magnetic system is more susceptible to the applied magnetic field, making it easier to align the magnetic moments of the clusters. Second, the velocity of the cold cluster beam is lower that improves the sensitivity of the detection. And third, internal cluster excitations can affect the actual magnetic order of the cluster.

Our cluster source is therefore cooled by using a cold head, powered by a closed-cycle refrigerator (Oerlikon coolpak 2000). Before entering the source, the carrier gas is separately cooled via a contact with the cold head, which also offers an advantage of gas purification. The lowest limit is 20 K, even though when running the setup only about 25 K can be reached, because of the heat created by the ablation laser. In order to make the temperature stable there is a heater in the bottom part of the source, which can be externally driven by a temperature controller (Lake Shore 332).

2.2.2   Velocity of the clusters

It was mentioned previously that to measure the velocity a chopper is installed at the end of the second chamber. It selects a small portion of the cluster cloud, setting the start-of-the-flight time (t_1). The final time is coming from the excimer laser pulse (t_2) which is used to ionize the clusters. Thus the velocity is $v = \frac{t_2 - t_1}{d}$, where d is the distance between the chopper and the ionization region, in our case 1.68 meters. The velocities of the clusters in all the experiments used for this thesis range between 380 and 1000 $\frac{m}{s}$.

2.3 The magnet

A gradient magnet is a central part of the Stern-Gerlach experiment [6]. After the cluster beam is skimmed and leaves the chopper, it passes through the magnet. There are 2 rectangular slits before it, one for each direction, which are finely adjustable with a maximum size of 5 mm x 10 mm. In most of the experiments that took place for this thesis the sizes used were 0.5 mm x 2 mm. In order to assure good collimation, the clusters travel in total about 1 m after the skimmer and before passing through the slits.

The magnet is of a Rabi two-wire design, where the iron pole faces follow the equipotential surfaces of a traditional Rabi two-wire magnet [7]. It is shown in Fig. 2.4. The magnet was designed using the Finite Element Method Magnetics (FEMM) software [8] in such a way that in the region where the clusters go through, the gradient for x-direction is constant, while the field is constant for y-direction, as can be seen in Fig. 2.5. There are several sets of poles for the magnet, so different magnetic field and gradient values can be achieved. The magnetic field values are up to 2.4 T, with the gradients up to 0.65 Tmm^{-1}.
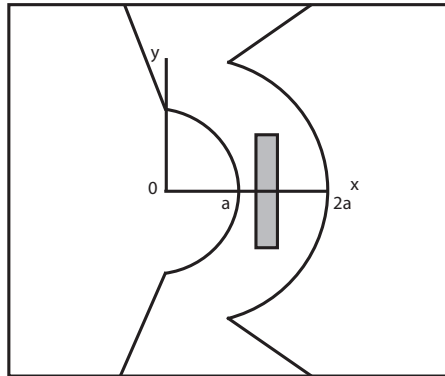
Figure 2.4: Schematic of the interior of the magnet. The poles can be exchanged, as different sets of poles are available with different curvatures. The gray square is the cross-section of the cluster beam.

Both features, the magnetic field and the gradient are important, as they both play a role in the deflections. While the magnetic field is responsible for aligning the magnetization of clusters, the gradient is the ultimate responsible for the deflection. The force experienced by a particle traveling through an inhomogeneous magnetic field is written as follows:

$$\mathbf{F} = \vec{\mu}\frac{\partial \mathbf{B}}{\partial \mathbf{z}},$$

(2.1)

where $\vec{\mu}$ is the time-averaged magnetic moment. The force will deflect the particle
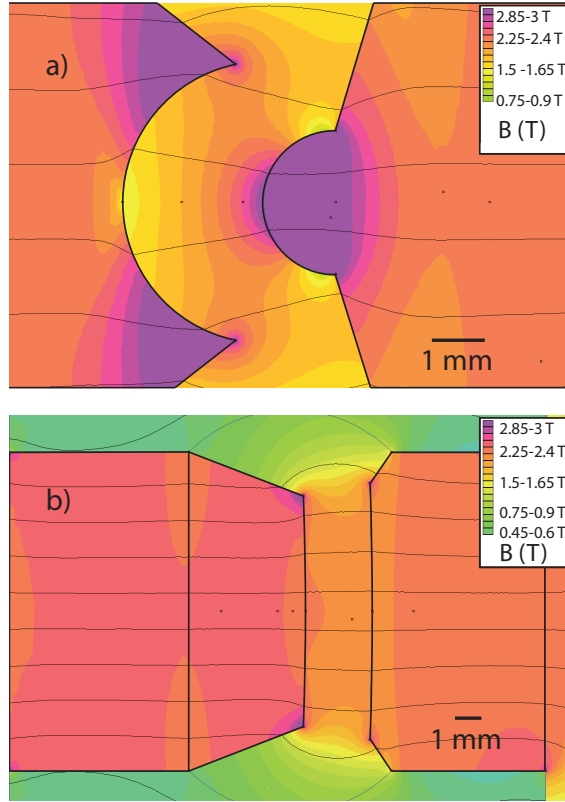
Figure 2.5: Plot of the magnetic field between the magnet poles. As can be seen, in a) the magnetic field is almost constant for y-direction while changing rapidly for x-direction. In b) the gradient is much smaller than in a). The intensity used for these plots is 8 A, which is the highest value which we can achieve in the laboratory.

perpendicularly to the propagation direction.

The forces can be very small, down to 5×10^{-21} N, which is the force felt by one single spin, 1 Bohr magneton, under the strongest achievable gradient of 650 T m^{-1}. Even though, the clusters undergo an acceleration of hundreds of g's, depending on their mass, e.g. Nb$_{11}$ in such a gradient will feel a force close to 200 g. The length, L, of the magnet is 12.5 cm, and the velocity of the clusters is between 400 $\frac{m}{s}$ and 1000 $\frac{m}{s}$. Thus, the time that the clusters interact with the magnet ranges between 300 μs and 125 μs, depending of the velocity. This is the main reason why the clusters are forced to travel a distance, D, of 0.8 m after the magnet to the ionization region, as deflections otherwise would be very small

and could not be detected. The deflection x is

$$x = \frac{\mathbf{F}(DL + L^2/2)}{m\mathbf{v}^2},$$
(2.2)

which in combination with previous equation can be rewritten as

$$x = K\frac{\vec{\mu}}{m\mathbf{v}^2}\frac{\partial \mathbf{B}}{\partial \mathbf{x}},$$
(2.3)

where K is the constant which depends on the geometry of the setup. As it is more convenient to work with magnetic fields rather than gradients we rewrite the equation as

$$x = K'\frac{\vec{\mu}\mathbf{B}}{m\mathbf{v}^2}.$$
(2.4)

Using this equation we can calibrate the setup, by estimating K'.

2.3.1 Calibration of the magnet

To calibrate the magnet we use a beam of atoms whose magnetic moment is known, or straightforward to deduce by using the Hund's rules for total spin S, total orbital moment L, and their sum J.

In combination with the Landé g-factor

$$g_J = \frac{3}{2} + \frac{S(S+1) - L(L+1)}{2J(J+1)},$$
(2.5)

and:

$$\mu_J = Jg_J\mu_B.$$
(2.6)

we obtain the maximal measurable z-component of the total magnetic moment of any atom.

Aluminium atoms were chosen to calibrate the setup because of the ease with which they are produced in the laser-ablation source. The magnetic properties of the Al atom are thus determined by: $S=\frac{1}{2}$, $L=1$, $J=\frac{1}{2}$, $g_J=\frac{2}{3}$, $\mu_J=\frac{1}{3}\mu_B$.

In order to obtain the calibration we measured the deflection profiles using different temperatures of the source, from 25 to 100 K, and different magnetic fields from 0 to 2.4 T. The obtained profiles are shown in Fig. 2.6. They show how the undeflected peak at 0 T broadens due to the magnetic field and eventually splits in two for $m_J=+\frac{1}{2}$ and $m_J=-\frac{1}{2}$.

In the inset in Fig. 2.6 a), the values of the deflections are plotted as a function of the magnetic field for 25 and 40 K. It can be seen that the deflections for Al atoms tend to saturate; the saturation takes place at a value slightly lower than 2 T for the atoms deflecting in the lowest magnetic field direction (positive values), while the saturation takes places at values slightly higher than 2 T for the
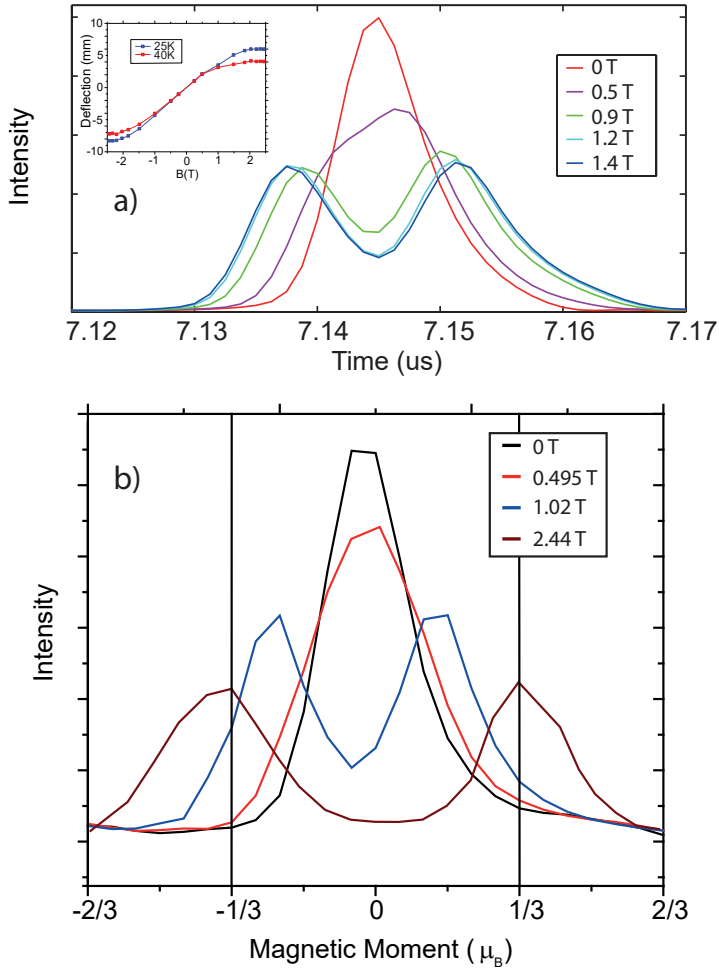
Figure 2.6: a) Deflection profile for aluminium atoms at 70 K. Inset: deflection as function of magnetic field for 25 K and 40 K. b) Deflection profile for aluminium atoms at 25 K with calibration on x-axis for magnetic moment μ_B for the 2.44 T deflection.

strongest magnetic field direction (negative values). Another interesting feature is that the deflections are somewhat larger towards the strongest magnetic field direction. The explanation can actually be found in Fig. 2.5a), where the change in the magnetic field values (the magnetic gradient) is clearly abrupter when going from the center of the flying region towards the right side of the electromagnet

than towards the left one.

Such data allowed us to obtain the calibration constant K′ as a function of the applied magnetic field. The K′ values range from 23.09 m to 32.49 m, the higher values corresponding for the lowest magnetic fields used because of the saturation behavior.

In order to check the quality of the calibration, a beam of Y atoms was used. Yttrium magnetic properties are: $S=\frac{1}{2}$, $L=2$, $J=\frac{3}{2}$, $g_J=\frac{4}{5}$ and $\mu_J=\frac{6}{5}\mu_B$. This is translated in 4 m_J states, $m_J=+\frac{3}{2}$, $m_J=+\frac{1}{2}$, $m_J=-\frac{1}{2}$ and $m_J=-\frac{3}{2}$, so 4 peaks are expected instead of 2, as it happens for Al. As can be seen in Fig. 2.7, the peaks of yttrium match the expected value very well.
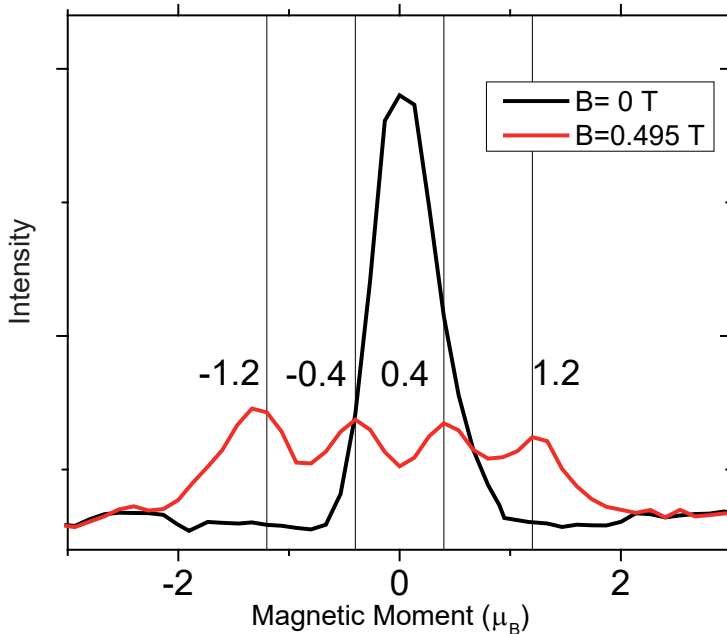
Figure 2.7: Deflection profile for yttrium atoms at 25 K, changing the x-axis to the magnetic moment using the calibration from Al measurements.

2.4 Time of flight mass spectrometry

The last part of the setup is the detection of the clusters after the deflection. The main principle of the time-of-flight mass-spectrometer (TOFMS) is that a charged particle in the presence of an electric field is accelerated, according to the second

Newton's law:

$$\mathbf{F} = m\mathbf{a} = e\mathbf{E} \tag{2.7}$$

where $\mathbf{a}$ is the acceleration of the particle, e is the elementary charge unit and $\mathbf{E}$ is the electrical field. Thus all the particles with the same charge experience the same force, and acquire the same kinetic energy. This means that all the particles having the same mass will have the same time of flight; the smaller the mass the larger the acceleration, and vice versa. Therefore, clusters with different masses will be separated after a certain distance.

Thus the simplest TOFMS consists of two plates with a certain voltage drop between them, followed by a field free region. A microchannel plate (MCP) serves as a detector. All the clusters studied in this thesis are neutrals, therefore the TOF is complemented with an excimer laser, which ionizes the clusters at the extraction region. For all the experiments used in this thesis the wavelength used was 193 nm, achieved with ArF mixture.

2.4.1 Linear two-stage TOFMS

For better focusing of clusters, TOFMS usually consists of two regions with gradients of electric field, formed by the electrodes called repeller, extractor, and ground plate, as shown in Fig. 2.8. The full mathematical derivation of the flight time can be found in references [9, 10]. It can be shown that

$$t_{TOF} = \sqrt{\frac{2a}{\xi_{RE}}} + \frac{\sqrt{2a\xi_{RE} + 2b\xi_{EG}} - \sqrt{2a\xi_{RE}}}{\xi_{EG}} + \frac{c}{\sqrt{2a\xi_{RE} + 2b\xi_{EG}}} \tag{2.8}$$

where

$$\xi_{RE} = \frac{e(V_x - V_b)}{mx}, \tag{2.9}$$

$$\xi_{EG} = \frac{e(V_b)}{mb}, \tag{2.10}$$

where ξ_{RE} is the acceleration in the repeller-extraction region, ξ_{EG} is the acceleration in the extraction-ground, while the parameters a, b, c, x, V_x and V_b are defined in Fig. 2.8.

By expanding the flight time from Eq. 2.8 as a Taylor series with respect to the position where the ions are formed (a_0) we obtain:

$$t_{TOF}(a) = t_{TOF}(a_0) + \frac{dt_{TOF}(a_0)}{da}(a - a_0) + \frac{1}{2!}\frac{d^2t_{TOF}(a_0)}{da^2}(a - a_0)^2 + ... \tag{2.11}$$

Not all the clusters enter the ionization region at the same exact position and the spread in starting positions results in loss of resolution. This can be avoided by selecting the parameters in a way that a number of terms in the Taylor series is
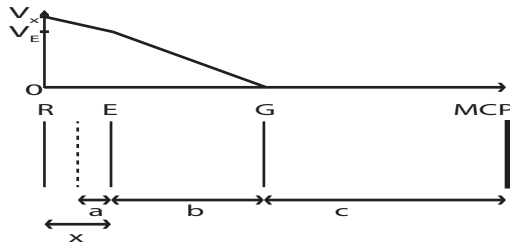
Figure 2.8: Geometry of the two stage linear TOFMS [9].

canceled. A single stage TOFMS which uses one single electric field gradient can correct the linear term, which is called *first order space focusing* [9]. Correspondingly, adding the second stage as in Fig. 2.8 cancels the quadratic term and it is referred as *second order space focusing*.

2.4.2   Position sensitive TOFMS

While normally one should take care to optimize the focusing of the clusters with a given mass, we would still need to determine their initial position changed by the deflection. The key point of the *position-sensitive TOFMS (PS-TOFMS)* is thus to be able to relate the different starting positions of the particles (deflections, in space units), with their times of flight detected at the MCP. The trade-off is thus between the position sensitivity and mass resolution.

In order to obtain a better resolution the addition of a second extractor plate was proposed [11]. In addition, a flying tube is installed between the extractors and the MCP and instead of having it grounded, a negative voltage value was set on it, which in addition to the negative voltage of the MCP leads to a better configuration to achieve a reasonable resolution.

For the given geometry of the PS-TOFMS we used the SIMION [12] electro-optic simulation package in order to find the optimal operation conditions. The distances between the electrodes were set to D_{R-E1}=30 mm, D_{E1-E2}=9 mm, D_{E2-FT}=20 mm, D_{FT}=800 mm, where R stands for repeller, E1 for the first extractor 1, E2 for the second extractor, FT for the flying tube and MCP for the Micro Channel Plate. Fig. 2.9 shows the results for the repeller voltage fixed at 5 kV, the flying tube at 0 kV and the MCP at -3 kV, varying the voltage of the extractors between 2.5 kV and 4.6 kV. The simulation showed that the best resolution for this set of voltages is at the extractor voltage of 4 kV. It is important to mention that the best resolution implies that there is no position sensitivity at all. This sets the starting point for the voltages in the laboratory. The voltage of the repeller cannot be increased further as it is the limit of the power supply. The voltage on the MCP of -3 kV corresponds to the optimum signal-to-noise ratio. Fig. 2.10 shows a typical mass-spectrum obtained experimentally with these conditions, for V_n clusters,

with V_{20} shown in the inset.
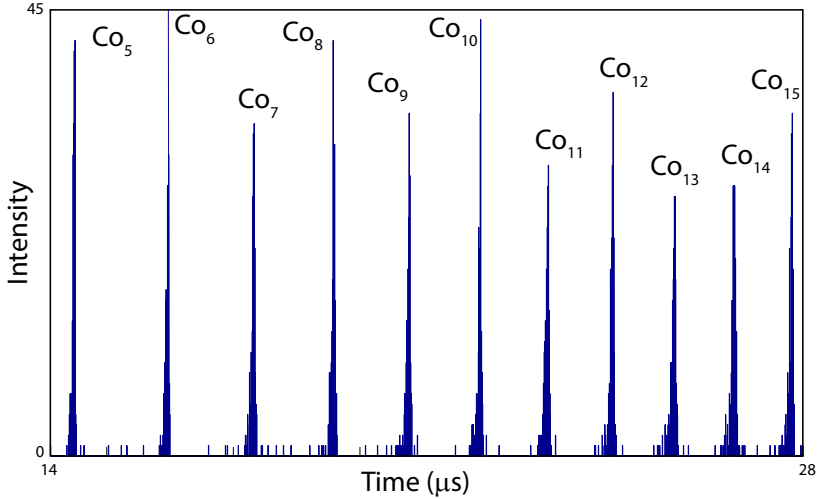
Figure 2.9: Simion electro-optical simulation for the time-of-flight distribution of cobalt clusters from Co_5 to Co_{15}, using 2200 particles, with voltages V_R=5 kV, V_E=4 kV, V_{FT}=0 kV and V_{MCP}=-3 kV.
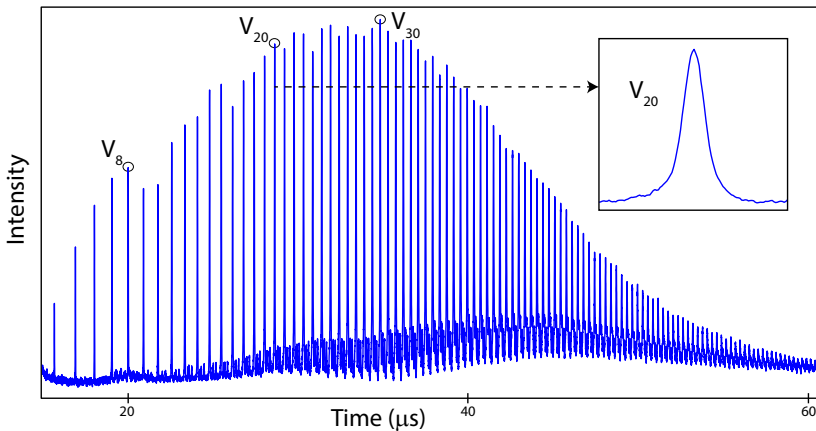
Figure 2.10: Typical experimental spectra obtained for vanadium clusters at 25 K. The inset is V_{20}, where it can be seen that it has a symmetric Gaussian profile.
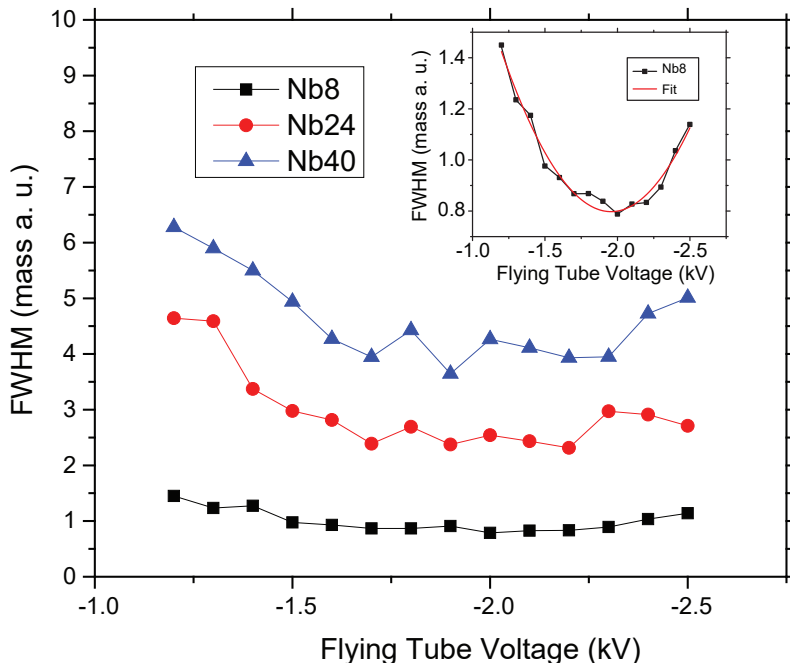
Figure 2.11: Evolution of Full Width at Half Maximum (FWHM) of measured cluster peaks as function of the voltage at the flying tube for Nb_8, Nb_{24} and Nb_{40}. The FWHM clearly depends on the mass, the heavier the cluster is the larger the FWHM is. The inset shows Nb_8 with more detail and a Gaussian fit is applied.

2.4.3 Calibration of the PSTOFMS

While the PSTOFMS resolution has been tested in simulations, it still needs to be verified experimentally. The starting conditions are the ones mentioned in the previous subsection. The only parameter available to improve the resolution is then the value of the voltage on the flight tube. This parameter is not of capital importance, but by changing it from -1.2 kV until -2.5 kV some improvement of the resolution among these values can be found. In Fig. 2.11 the evolution of the FWHM of three different clusters, Nb_8, Nb_{24} and Nb_{40} is shown. As can be seen the FWHM depends strongly on the mass. The selected voltage for the flight tube was therefore -2 kV, as it is the value obtained by fitting the curve with a Gaussian fit, as can be seen in the inset in Fig. 2.11.

After improving the quality of the signal the last step is to calibrate the PS-TOFMS in units of the deflection. This was done by measuring the spectra using a narrow slit, of 0.5 mm width, which was placed in the path of the excimer beam, providing a very narrow laser beam. The position of the slit was changed
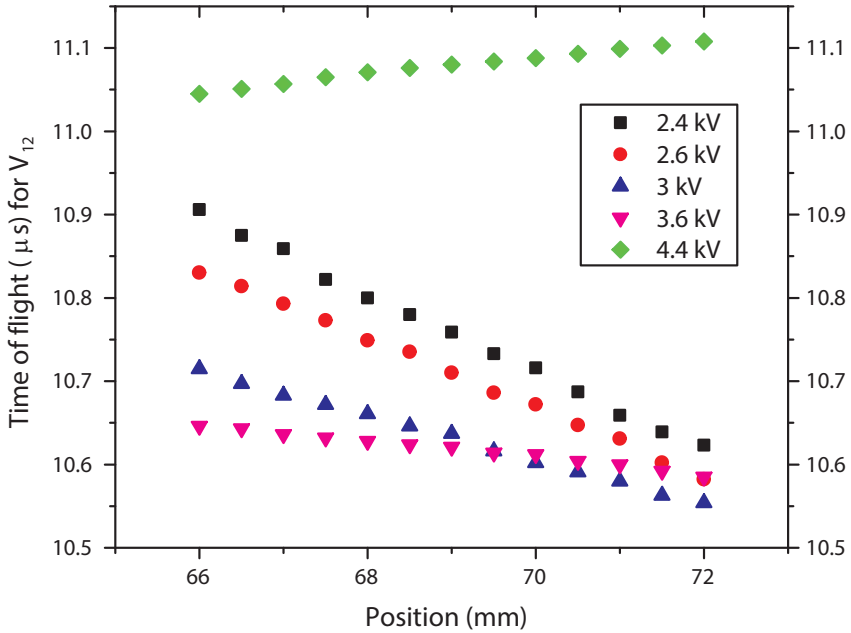
Figure 2.12: Evolution of the time of flight for V_{12} as function of the voltage applied on the extractors. The rest of the voltages were V_R=5 kV, V_{FT}=-2 kV and V_{MCP}=-3 kV.

in steps of 0.5 mm, covering the whole ionization region. This procedure gives us the time of flight of particles ionized at different positions in the spectrometer.

As can be seen in Fig. 2.12, the slope increases while going away from the optimal 4 kV voltage, as expected. Note that for a voltage of 4.4 kV the slope is positive while for all the other voltages it is negative. It also can be seen that for 4.4 kV and 3.6 kV the slope is the very similar, but of opposite sign, which is roughly expected as the difference in voltage from the *time focusing* voltage is the same.

Practically all the measurements performed in this thesis were obtained using V_R=5 kV, V_E=3.6 kV, V_{FT}=-2 kV and V_{MCP}=-3 kV, because it has enough sensitivity to detect small changes in deflections while keeping sufficiently good resolution. For V_{12} the sensitivity with this set of voltages is 9.79 $\frac{ns}{mm}$. The sensitivity versus the extractor voltage for V_{12} is shown in Fig. 2.13.

Further, the sensitivity scales with the square root of the mass. This can be easily seen because the kinetic energy is

$$E_K = \frac{mv^2}{2} \qquad (2.12)$$
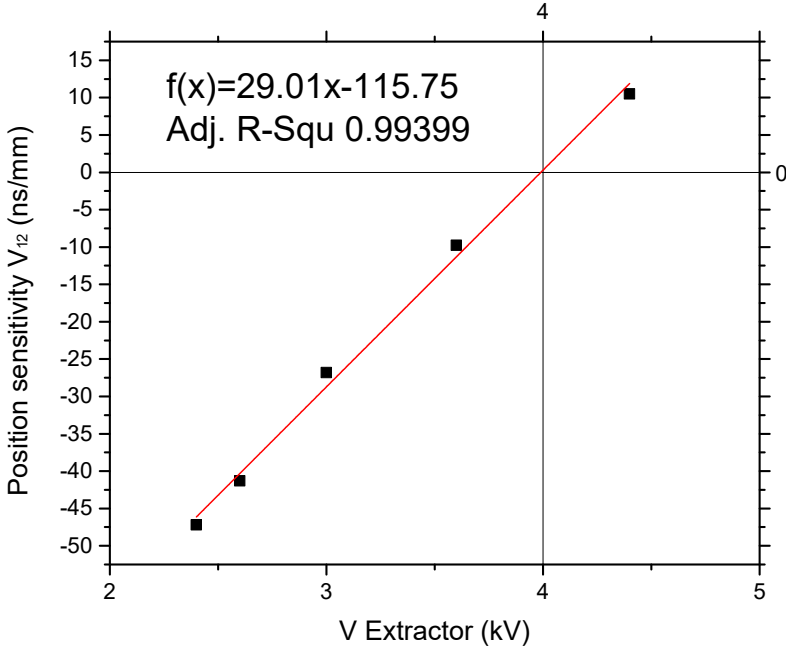
Figure 2.13: Evolution of the position sensitivity for V_{12} as function of the voltage applied on the extractor plates. The rest of the voltages were V_R=5 kV, V_{FT}=-2 kV and V_{MCP}=-3 kV. It proves what was found in the SIMION simulation, that is that for V_E=4 kV there is no sensitivity.

and the velocity is

$$v = \frac{x}{t} \tag{2.13}$$

so the times measured change as

$$t^2 = m\frac{x^2}{2E_K} \tag{2.14}$$

and thus the measured flight times depend on the $\sqrt{m}$. In Fig. 2.14, the square of the position sensitivity is plotted as a function of the cluster size. It can be seen that the values fit nicely within the error bars and that for the smallest masses the performance is the best, which is in fact the best outcome for the purposes of this thesis. From this, the position sensitivity of any desired mass can be found.
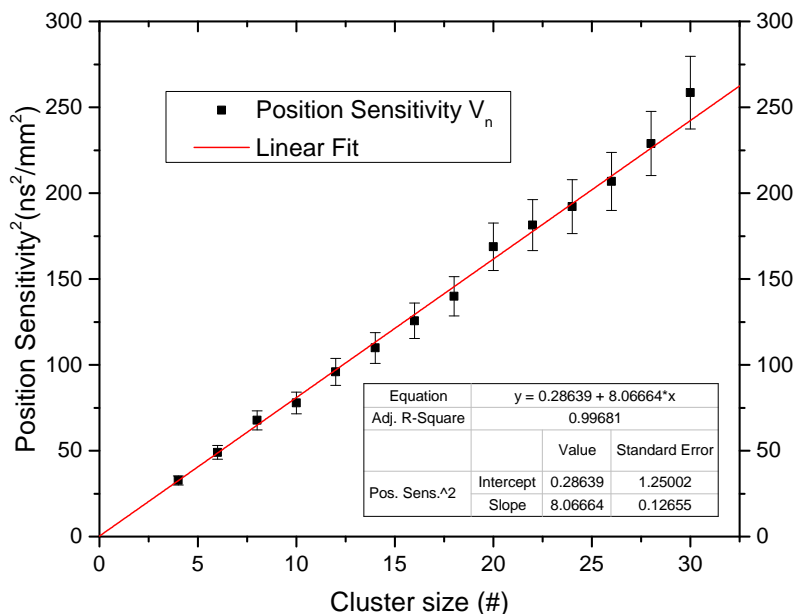
Figure 2.14: Evolution of the square of the position sensitivity of the PSTOFMS for V_n as function of the cluster size. The voltage set is the same as used for all the measurements: V_R=5 kV, V_E=3.6 kV, V_{FT}=-2 kV and V_{MCP}=-3 kV.

2.5 Free electron laser

We used the FELIX Free Electron Laser laboratory in Nijmegen. It was used as a source of infrared radiation in order to populate vibrational excited states, which in turn helped to reveal the geometric structure of clusters. The main principle of such laser is the emission of electromagnetic waves by relativistic electrons when passing through an array of magnets of alternated polarity. These pairs are located inside the laser cavity and alternate with a period λ_u creating the undulator which is shown in Fig. 2.15 (a).

Thanks to the Lorentz force the electrons oscillate perpendicularly to the magnetic field which in turn causes the emission of radiation. The wavelength emitted at each undulator period interferes if they differ by integer number of wavelengths: $\lambda_n = n \cdot \lambda_1, n = 1, 2, 3...$ λ_n are defined as "resonant". The time required for an electron to travel one undulator period is $\tau_{bunch} = \lambda_u / \bar{v}_z$, where $\bar{v}_z$ is the average speed (along the undulator). For the wavefront this time is $\tau_{light} = (\lambda_u + n \cdot \lambda_n)/c$, where c is the speed of light in vacuum. By equating these
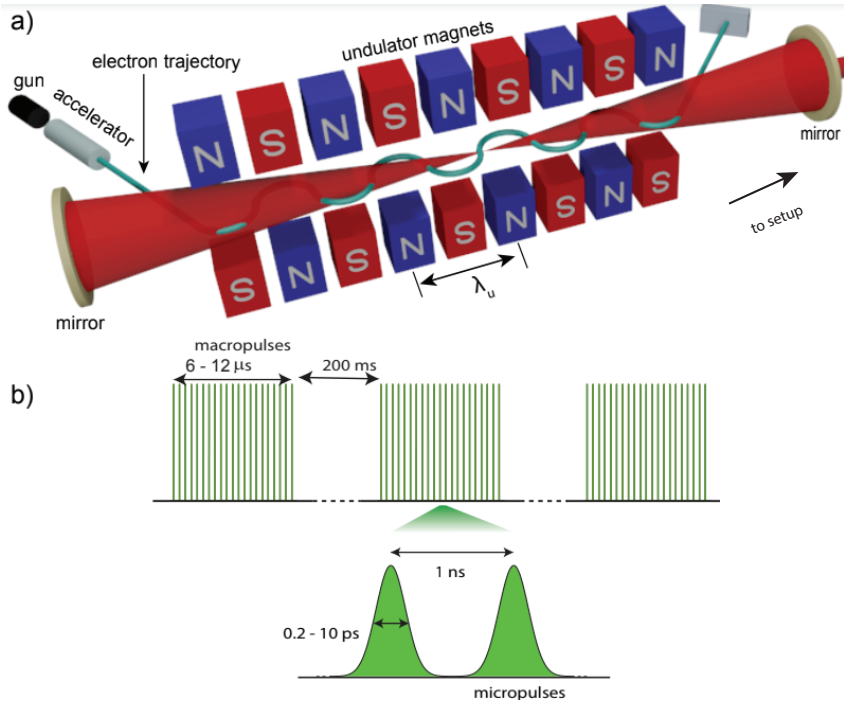
Figure 2.15: a) Schematic of a FEL cavity. Electrons produced by the gun after acceleration enter the undulator that consists of equally spaced magnets of alternating polarity with period λ_u; FELIX and FELICE pulse structures at the repetition rate of 1 GHz micro- and 5 Hz macropulses. Adapted from V. Chernyy, Ph.D. thesis [13].

two times, λ_n can be expressed as [14]

$$\lambda_n = \frac{\lambda_u}{2n\gamma^2}(1 + \bar{a}_u^2), \tag{2.15}$$

where $\bar{a}_u^2$ is a dimensionless parameter proportional to the undulator period and magnetic field, and γ is the Lorentz factor.

The wavelength can be tuned by varying either the energy of the electron beam or the magnetic field. During the wavelength scan the latter is performed via the variation of the gap between the two rows of magnets.

The undulators of the FELs used in this work are contained within optical cavities formed by mirrors at each end of the undulator. The light emitted by a bunch of electrons after the round trip in the cavity stimulates emission interacting with the electron beam of the next cycle and gets amplified. For this to happen, the round trip time of the light pulse must coincide with the repetition

period of the electron bunches t_a [14]:

$$\frac{2L}{c} = rt_a, \tag{2.16}$$

where r is a rational number and L is the cavity length. This equation determines the structure of the IR beam. The light is emitted in a macropulse of 6-12 μs duration (determined by the time over which the accelerator operates) that consists of micropulses 1 ns apart at 1 GHz repetition rate, see Fig. 2.15 (b).

In the case of FELIX [14], radiation produced in the cavity is outcoupled through a hole in one of the mirrors and is further guided in vacuum into the experimental instrument. FELIX produces IR radiation in the range 66-3600 cm^{-1}. The spectral bandwidth is transform-limited and is adjustable between 0.2-5 %RMS of the central frequency by changing the overlap between the electron bunch and the wavefront. In the experimental setup coupled to FELICE [15], the cluster beam passes through the laser cavity and crosses the IR beam axis at 35° angle. The pulse energy is thus 10-30 times higher for FELICE than for FELIX. FELICE produces IR radiation in the range 100-2000 cm^{-1}.

The maximum macropulse energy provided by FELIX is 100-120 mJ. The pulse energy can be varied over four orders of magnitude with fixed-value attenuators before the light enters the experimental setup.

In FELICE's case, a small fraction of IR radiation, outcoupled through a small hole in one of the cavity mirrors, is measured for the power and wavelength calibration. The laser beam inside the FELICE cavity is assumed to be Gaussian and can be fully characterized by the Rayleigh range z_0, the wavelength λ and the intensity at the center of the beam at the focus position I_0. The radial intensity distribution in the laser beam is given by [16]

$$I(x,z) = I_0 exp\left(-\frac{2x^2}{w^2(z)}\right), \tag{2.17}$$

where $w(z)$ is the spot radius at distance z along the laser propagation direction. Note that for Gaussian beams the diameter $2w(z)$ is measured at 13.5 % (or 1/e^2) of the peak intensity (industry standard [16, 17]).

As a function of the distance from the local point, $w(z)$ is defined as

$$w(z) = w_0\sqrt{1 + (z/z_0)^2}, \tag{2.18}$$

where w_0 is the beam radius at focus, or *waist*

$$w_0 = \sqrt{z_0\lambda/\pi}. \tag{2.19}$$

The molecular beam instrument was designed such that $z_0 = 55$ mm, which simplifies the expression for w_0 (expressed in mm) to $w_0 = 0.13\sqrt{\lambda}$ for λ given in μm. To relate the power inside the cavity, P_{in}, to the power measured P_{out} through a hole with radius r, Eq. 2.17 should be integrated from $x = 0$ to r, which gives,

$$P_{out} = P_{in} \left[1 - exp \left(\frac{-2r^2}{w^2(z)} \right) \right].$$ (2.20)

With this equation it is possible to reconstruct the pulse energy inside the laser cavity by measuring its fraction outcoupled through a hole with radius r.

2.6 Analysis of the deflection profiles

In order to study the magnetic properties of clusters we thus record the spectra with and without magnetic field, I_{on} and I_{off}. The flight times are converted to the deflection using the calibration, and then used in Eq. 2.4 in order to obtain the magnetic moments. So far, however, we have only discussed the deflection of atoms. For the majority of magnetic clusters, in contrast, the deflection behavior is very different. Because of the coupling between the magnetic moments and the cluster lattice, the measured deflections reflect the *average* magnetic moments of clusters in given magnetic field. This still needs to be converted to the real magnetic moments. In order to do so, the Langevin formula[18] is used

$$M = \mu \left(coth \left(\frac{\mu B}{k_B T} \right) - \frac{k_B T}{\mu B} \right)$$ (2.21)

where M is the measured magnetization, k_B is the Boltzmann constant, T is temperature, B is the applied magnetic field and μ is the magnetic moment defined by $\mu = g\mu_B J$, where J is the total angular momentum assumed to be sufficiently large. We always worked in the low-field limit, that is when $\mu B \ll k_B T$ ($1\mu_B \cdot 1T \approx 1K$). In such conditions Eq. 2.21 can be approximated by

$$M = \frac{1}{3} \frac{\mu^2 B}{k_B T}$$ (2.22)

which is referred to as the Langevin-Debye limit. In the high field limit $M = \mu$, but the high field conditions were never satisfied in the experiments described in this thesis.

The deflection profiles studied in this thesis were of various kinds, depending on the magnetic behavior of the studied cluster. In Fig. 2.10 it can be seen that V_{12}'s peak has a Gaussian profile and it is quite symmetric, in the absence of the magnetic field. All the undeflected peaks had a similar profile. For the deflected peaks the situation is quite different, as most of them are not symmetric when the magnetic field is applied. Some clusters deflect in a similar way to atoms, as shown for Fig. 2.6; in this case, to get the magnetic moments, we calibrate the x axis to magnetic moment units, by using the calibration from Al atoms and then to apply as many Gaussian curves as number of visible peaks present in the spectra, as can be seen in Fig. 2.16.
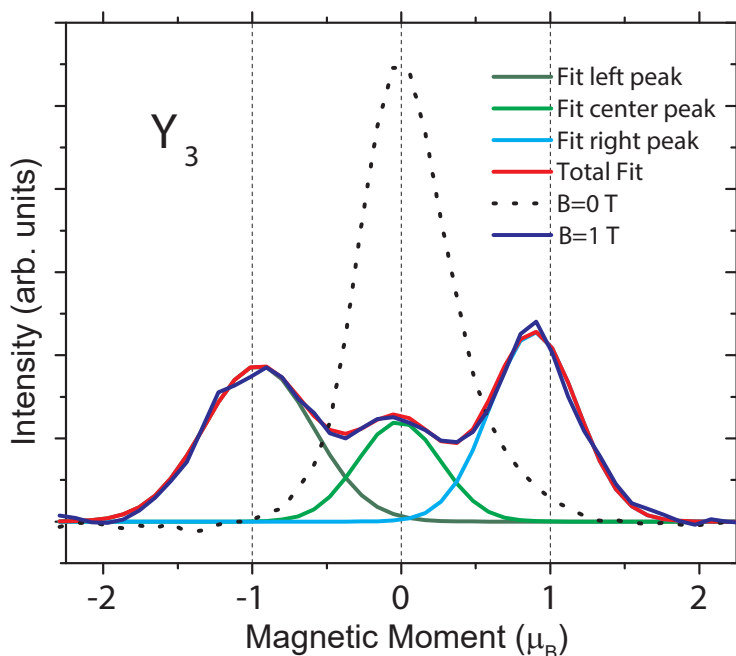
Figure 2.16: Example of fit for multiple Gaussian profile deflection, Y_3. Spectra obtained at 25 K. It can be seen that there are two peaks located at ± 1 μ_B and another at 0 μ_B.

Another possibility is that the deflected peak is shifted and asymmetrically distorted into the field direction. In this situation we integrated the whole area under the peak and take the mean value instead of the maximum. This was done for peaks like the one shown at Fig. 2.17. This is the most common situation for magnetic clusters, as most of them are superparamagnetic and therefore deflect in the direction of the strongest magnetic field, as well as broaden in that direction.

2.7 Summary

The first goal of this thesis was to design and build both the magnet and the time of flight mass spectrometer in order to improve the performance achieved with the previously existing experimental setup.

Then it was necessary to calibrate both of them and search for the better possible conditions which allow to study the magnetic properties of 3d/4d and rare earth metal clusters.

In this chapter we have described all the details and the method to study
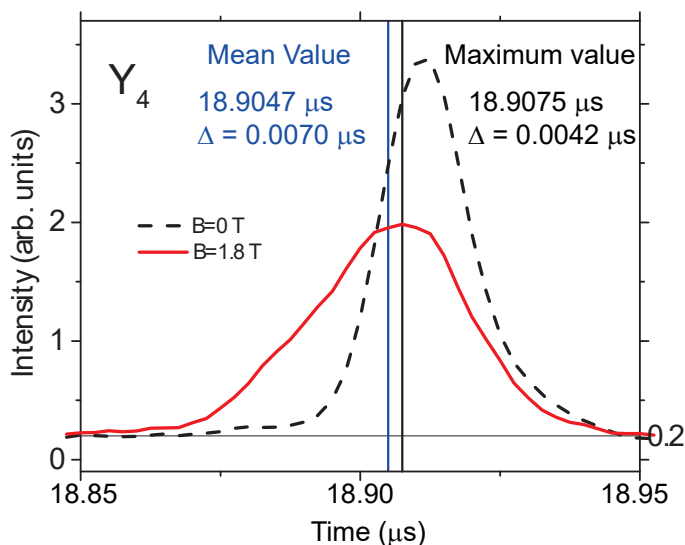
Figure 2.17: TOF spectra for Y_4 (Yttrium). This is an example of a non-symmetric deflection, where the left side of the peak is wider than the right one. For this kind of peaks it is better to integrate the peak and calculate the mean value of deflection than taking its maximum, as it gives a better estimation of the average behavior of the particles. Both values are shown.

the magnetic properties of clusters. All the data shown in the following chapters dealing with the magnetic moments of clusters are obtained with this setup.

References

[1] R. Bingham and P. Salter, "Analysis of solid materials by laser probe mass spectrometry," Anal. Chem. **48**, 1735 (1976).

[2] R. E. Smalley, "Laser Studies of Metal Cluster Beams," Laser Chem. **2**, 167-184 (1983).

[3] S. Maruyama, L. R. Anderson, and R .E. Smalley, "Direct Injection Supersonic Cluster Beam Source for FT-ICR Studies of Clusters," Rev. Sci. Instrum. **61**, 3686 (1990).

[4] A. Fielicke, G. von Helden, and G. Meijer, "Far-Infrared spectroscopy of isolated transition metal clusters," Eur. Phys. J. D. **34**, 83-88 (2005).

[5] F. W. Payne, Wei Jiang, J. W. Emmert, Jun Deng, and L. A. Bloomfield, "Magnetic structure of free cobalt clusters studied with Stern-Gerlach deflection experiments," Phys. Rev. B. **75**, 094431 (2007).

[6] O. Stern and W. Gerlach, Ann. Phys. **74**, 672-699 (1924).

[7] I. I. Rabi, J. M. B. Kellogg, and J. R. Zacharias, "The Magnetic Moment of the Proton," Phys. Rev. **46**, 157 (1934).

[8] D. C. Meeker, Finite Element Method Magnetics (FEMM) Version 4.0.1, http://www.femm.info (2006)

[9] W. C. Wiley and I. H. McLaren, "Time-of-Flight Mass Spectrometer with Improved Resolution," Rev. Sci. Instrum. **26**, 1150 (1955).

[10] R. Weinkauf, K. Walter, C. Weickhardt, U. Boesl, and E. Schlag, "Laser Tandem Mass Spectrometry in a Time of Flight Instrument," Naturforsch. Teil A. **44**, 1219 (1989).

[11] W. A. de Heer and P. Milani, "Large ion volume time-of-flight mass spectrometer with position- and velocity-sensitive detection capabilities for cluster beams," Rev. Sci. Instrum. **62**, 670 (1991).

[12] SIMION 8.0.4 (Scientific Instrument Services, Inc. (SIS), 2008).

[13] V. Chernny, Ph.D. thesis, "The interplay between electronic and vibrational excitations in atomic clusters" Radboud University, Nijmegen, The Netherlands (2017).

[14] D. Oepts, A. van der Meer, and P. van Amersfoort, "The Free-Electron-Laser User Facility FELIX," Infrared Phys. and Techn., **36**, 297-308 (1995).

[15] J. M. Bakker, V. J. F. Lapoutre, B. Redlich, J. Oomens, B. G. Sartakov, A. Fielicke, G. von Helden, G. Meijer, and A. F. G. van der Meer, "Intensity-resolved IR multiple photon ionization and fragmentation of C_{60}," J. Chem. Phys., **132**, 1-9 (2010).

[16] D. Hill, *How to Convert FWHM Measurements to 1/e-Squared Halfwidths*. Radiant Zemax Knowledge Base, 2007.

[17] Data Ray Inc., WinCam, "Beam Profiling Cameras," User Manual.

[18] S. N. Khanna and S. Linderoth, "Magnetic behavior of clusters of ferromagnetic transition metals," Phys. Rev. Lett. **67**, 742 (1991).

3 Kramers degeneracy theorem and relaxation in V, Nb, and Ta clusters

In this chapter we investigate the magnetic properties of vanadium, niobium and tantalum clusters. All these materials belong to the group V of the periodic table, and thus possess a similar electronic structure. None of these materials is ferromagnetic in the bulk. Despite of this, magnetism of V clusters was predicted by some theoretical publications, but no experimental data has been published so far that corroborates this. Thus, in this chapter first vanadium cluster deflections will be measured and from them the magnetic moments will be derived.

The magnetic properties of niobium clusters were already studied before. We nevertheless re-measure them here, to directly compare the results with the ones from vanadium. In addition, tantalum clusters will also be studied. Tantalum is a much heavier material than vanadium or niobium, which makes it more challenging for precise deflection measurements.

While only a few of the clusters show small magnetic moments, all odd-numbered clusters deflect due to the presence of a single unpaired electron. Surprisingly, for majority of V and Nb clusters an atomic-like deflection behavior is found, namely a splitting of the cluster beam in two, corresponding to $\pm 1\ \mu_B$. This is a direct indication of the absence of spin-lattice interaction, and is in agreement with Kramers degeneracy theorem for systems with a half-integer spin. This purely quantum phenomenon is surprisingly observed for large systems of more than 20 atoms, and also gives access to various quantum relaxation processes, via Raman two-phonon and Orbach high-spin-state mechanisms. In heavier, Ta clusters, the spin relaxation is always present, probably due to larger masses and thus lower phonon energies. [*]

3.1   Introduction

Kramers degeneracy theorem [1] states that every energy eigenstate of a time-reversal symmetric system with non-integer total spin is at least doubly degenerate. The basis states of the system are Kramers-conjugate, i.e. they are related to each other by the time-reversal operator. The immediate consequence of this is that for such a system, spin-lattice coupling is prohibited, because any spin-phonon operator is invariant under time reversal, and therefore has zero matrix elements for the transitions between such states. This selection rule, also known as the Van Vleck cancellation [2], implies that the lattice excitations cannot be responsible for the relaxation between two Kramers conjugated states. Therefore, S_z is a good quantum number similar to that of an isolated atom.

The relaxation can nevertheless happen via either Raman or Orbach mechanisms [3]. The first one includes excited vibrational states and is thus temperature dependent. The second type of relaxation involves excited spin states and is active in systems with the total spin larger than 1/2. Moreover, there are other, more material-dependent mechanisms of the relaxation, such as for example the electronuclear spin entanglement [4].

In the absence of the relaxation, a system with the minimum half-integer spin may represent the smallest possible magnetic bits thus creating a new paradigm in magnetic storage technology. The understanding of the exact behavior of the relaxation mechanisms is therefore very important, both for the possible applications and for the fundamental understanding of the quantum decoherence processes. The majority of studies are focused on the behavior of single magnetic ions [5]. In larger system, the decoherence processes are usually considered too strong for any realistic appearance of the spin blocking. This is particularly true when a non-isolated system is considered.

Gas-phase atomic clusters represent ideal model systems [6, 7], used to understand various phenomena in totally different areas of science, from nuclear physics to crystal growth. The condensed matter properties such as magnetism [8, 9], are combined with the molecular reproducibility of their structure. All energy levels in the clusters are discrete and tunable by simply varying their size, leading to the unique possibility to tune the microscopic correlations and from this the macroscopic properties, to our needs.

It is known that the smallest clusters of the magnetic 3d metals, Fe, Co and Ni [9–11], are magnetic, and their magnetic moment per atom is higher than that in the bulk. It could therefore be expected that other transition metals can also posses some magnetic moments in the cluster regime. The atomic vanadium, in particular, has the same orbital and spin magnetic moment as cobalt, $3\mu_B$ each, only here the 3rd Hund's rule results in a small total magnetic moment of just $0.6\mu_B$, far from the $6\mu_B$ of cobalt. In the bulk, cobalt is a ferromagnet, while vanadium is a paramagnet. It may thus be expected that vanadium clusters can become magnetic as well, as orbital magnetic moments becomes quenched [12]. Several theoretical studies predicted rather different, but non-zero, values for the

magnetic moments in some of V clusters. However, the experiments are lacking.

While the magnetic properties of niobium clusters were already studied by the group of de Heer [13], we still re-measured them in our setup, in order to have a complete picture and a possibility of a direct comparison with V and Ta. The latter was mentioned in [13] to have a similar set of properties as Nb, but no results were shown.

Another significant interest to study these clusters stems from the fact that each of these atoms has an odd number of electrons, and thus in all odd-numbered clusters the total spin will unavoidably be non-integer. Would that lead to the absence of the spin-lattice relaxation, at least in the smallest of the clusters?

Here we demonstrate that the Kramers degeneracy indeed leads to the spin blocking in small gas-phase clusters of early d-metals, such as vanadium and niobium. In such clusters, the interaction with external bath appears to be fully excluded. Due to the odd number of electrons per atom, there is always a non-zero total spin in the clusters with odd number of atoms. Several of the clusters with the total spin 1/2 showed the blocked-spin behavior on the time scale of the experiment (~0.1 ms), in spite of the highly populated rotational states. Clusters with larger magnetic moments, though also corresponding to the half-integer spin, showed the clear superparamagnetic behavior, indicating the Orbach relaxation mechanism. Moreover, introducing vibrational excitation in a cluster also leads to the appearance of relaxation via Raman mechanism.

3.2 Vanadium clusters

Vanadium clusters attracted a certain interest for a while, which was translated in a number of publications, practically all results of computational studies. While taking into account that the orbital contribution to the magnetic moment tends to quench, it could still be expected that some ferromagnetic ordering of the spins could take place, leading to magnetic moments. As a result, these computational studies predicted magnetic moments of V clusters of many sizes, but without much of agreement between themselves [14–19]. In Fig. 3.1 we summarize the values that were found. To cite some examples, Liu et al., [14] found a magnetic moment of 2.89 μ_B for V_9, while no magnetic moment at all for V_{15}. In the same work it was also predicted that for a chain between 2 and 7 atoms of vanadium, the net magnetic moment would be closer to 4 μ_B per atom. Dorantes-Dávila et al. [15] studied the magnetic moment as function of the parameter J/W, where J is the exchange integral and W the bulk band width. They found a total magnetic moment between 0-4 μ_B for V_9, in the case of ferromagnetic order, and moments between 0-3 μ_B for an antiferromagnetic one. For V_{15} they reported a magnetic moment of 0-4 μ_B for a ferromagnetic cluster and not net magnetic moment for an antiferromagnetic one. Lee et al. [16] found different values for the magnetic moment of V_9 depending on the interatomic distance, varying from 0.33 to 2.78 μ_B per atom, achieving larger values as the lattice parameter increases, while they
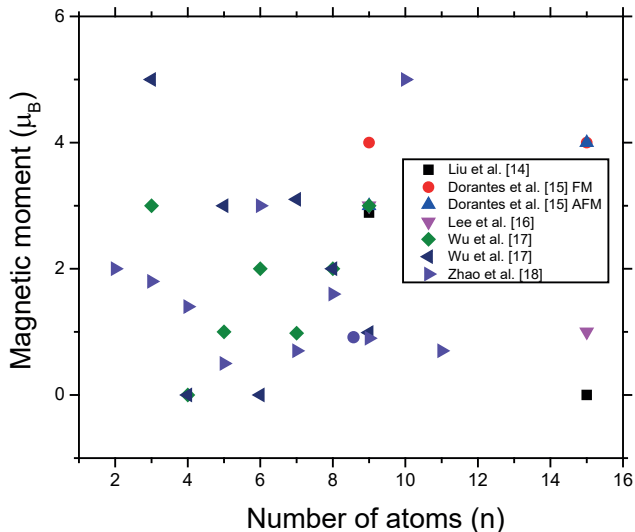
Figure 3.1: Magnetic moments of V clusters predicted by references [14–18].

found a value for the magnetic moment of 0.07 μ_B per atom for V_{15}. Alvarado et al. [19] found that the magnetic moment for V_{13} varies between 3 μ_B and 4 μ_B, depending on the geometry.

Zhao et al. [18] studied vanadium clusters between V_2 and V_{15}, with values ranging from 0.5 μ_B for V_5 and 5 μ_B for V_{10}. Their predicted magnetic moments decrease significantly for clusters larger than V_{11}, showing values lower than 1 μ_B for all of them. Wu et al. [17] calculated magnetic moments for 2 geometrical structures lower in energy, for all vanadium clusters between 3 and 9 atoms. Only two among all of them had the same magnetic moment for both cases, 0 μ_B for V_4 and 2 μ_B for V_8.

It is thus clear that there is a very large scattering of the calculated values, that calls therefore for the experimental verification.

There was an attempt to do so by Douglass et al., [20] who tried to measure the magnetic deflections of V_n clusters; however, no deflections were observed. Taking into account the (rather poor at the time) resolution of their experiment they were able to estimate a maximum possible value for the magnetic moment per atom for V_9 of 0.59 μ_B, and 0.18 μ_B for V_{99}.

3.2.1 Deflection profiles and magnetic moments of V_n clusters

If the Douglass et al. [20] experiment is taken into account, two observations can be made. The first is that if the magnetic moments of V_n clusters are very small, the magnetic field and its gradient have to be sufficiently strong, in order to be able to observe any deflection. The second observation is that the temperature at which the experiment takes place is of importance, as soon as the temperature of 89 K was probably not low enough for sufficient sensitivity.

Under these two premises we measured V_n. The first measurement which took place for V_n clusters was at a source temperature of 25 K, the lowest that could be achieved in our setup. The magnetic field used was the maximum that could be achieved, 2.4 T. The carrier gas pressure employed was 2 bar. The results are shown in Fig. 3.2, were the x axis is calibrated in magnetic moment units, by using the deflection profile of Al atoms as described in the experimental chapter.

It can clearly be seen that approximately half of the clusters deflect, while the other half does not. All V_n odd-numbered clusters deflect when going through the electromagnet, while most of V_n even-numbered clusters do not. Among the clusters containing an odd number of atoms there are two different types of behavior. The most common one is that of the clusters which show 3 peaks patterns, with two peaks at ± 1 μ_B and another at 0 μ_B. This kind of behavior is obviously atomic-like, similar to the ones shown in Chapter 2, at Fig. 2.6, Fig. 2.7 and Fig. 2.16. This is not what is actually expected for clusters, as superparamagnetic particles usually deflect only towards the strong direction of the magnetic field. This latter behavior is shown by some vanadium clusters as well.

These peaks at ± 1 μ_B are thus due to a single unpaired electron. It is interesting to note that at this low temperature the unpaired spin is apparently not coupled to the lattice. The peak at 0 μ_B is apparently due to some relaxation. We will discuss its properties later.

As previously mentioned, there are also clusters that exhibit superparamagnetic behavior, and the profile for their spectra shows deflections towards the direction of the strong magnetic field, i.e. deflections towards the left side. This behavior is exhibited by V_{13}, V_{15} and V_{33}. We convert the deflections into magnetic moments by using the Brillouin formula taking into account small values of J [21]:

$$M = \mu B_J(x) \tag{3.1}$$

where x is the ratio of the Zeeman energy of the magnetic moment in the external field to the thermal energy $k_B T$:

$$x = \frac{\mu B}{K_B T} \tag{3.2}$$

and $B_J(x)$ is the Brillouin function,
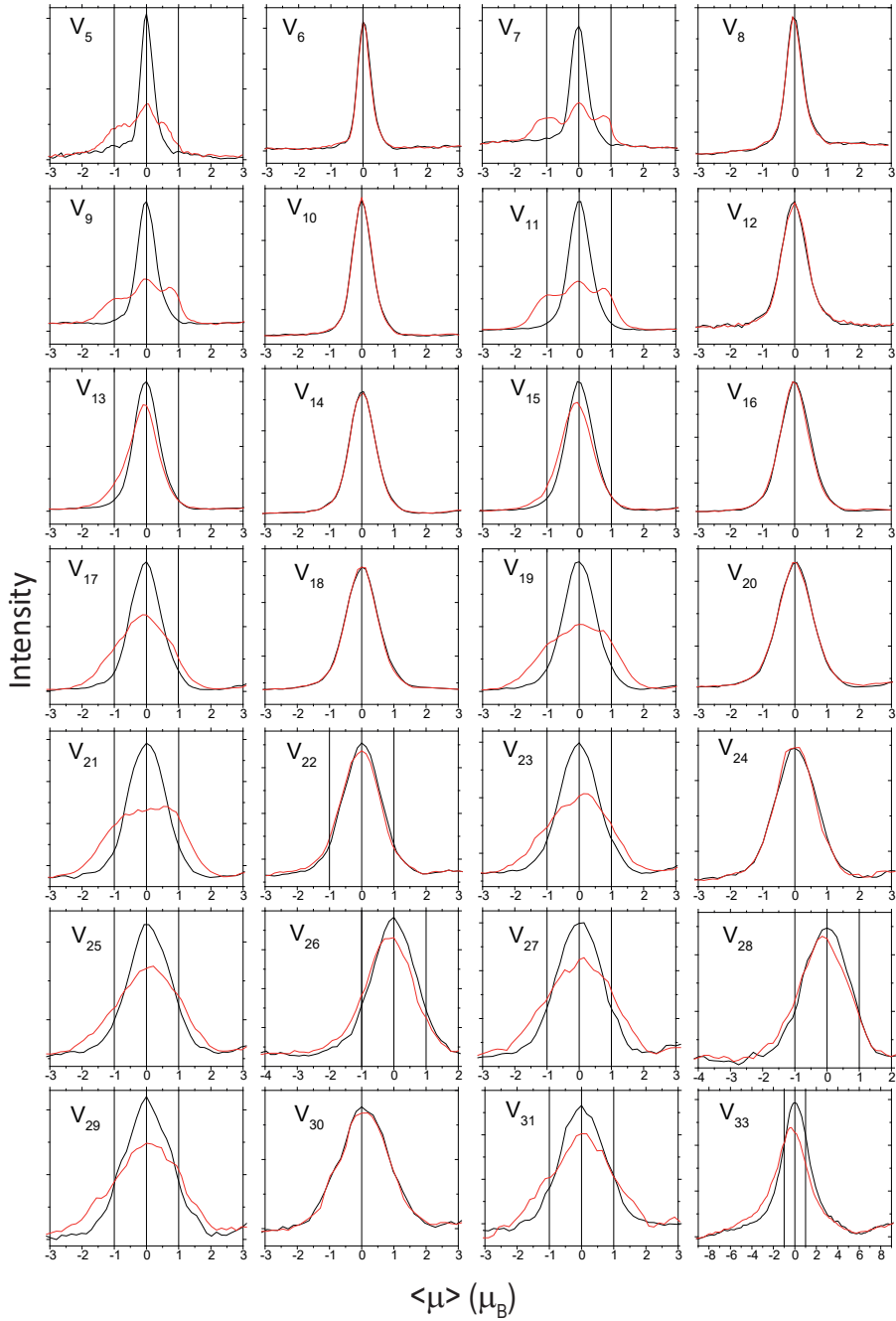
Figure 3.2: Magnetic deflections of V_n clusters at 25 K. Black line for magnetic field off, red line for magnetic field 2.4 T. Pressure of the carrier gas was 2 bar.
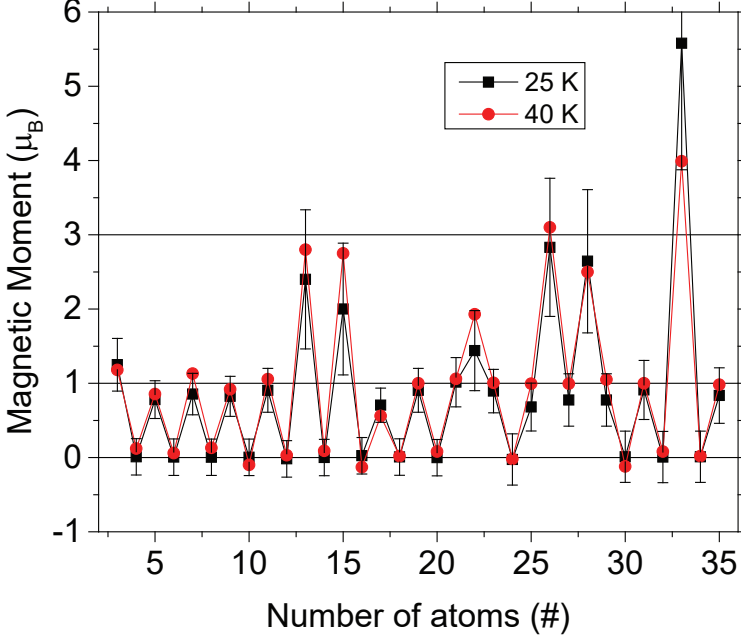
Figure 3.3: Magnetic moments of V_n clusters as function of size. In black values obtained at 25 K, while in red the values were obtained at 40 K.

$$B_J(x) = \frac{2J+1}{2J} coth\left(\frac{2J+1}{2J}x\right) - \frac{1}{2J} coth\left(\frac{1}{2J}x\right)$$ (3.3)

where J is total angular momentum, positive integer or half-integer. For low fields can be approximated by the Curie law, and for large J (J→ ∞) the approximation is equivalent to the one for the Langevin formula, in the case of low fields, described in the previous chapter, in Eq.2.22[22, 23]:

$$M = \frac{1}{3}\frac{\mu^2 B}{k_B T}$$ (3.4)

The resulting magnetic moments obtained for V_{13} and V_{15} are around 3 μ_B, while for V_{33} the magnetic moment is around 5 μ_B. It is interesting to note that the origin of the 3 μ_B is not clear, but the spin magnetic moment of vanadium atoms is 3 μ_B, and taking into account that the orbital part of the magnetic moments gets quenched fast with size, it could be that the 3 μ_B are coming from the spin contribution of a single atom.

Table 3.1: Magnetic moments predicted by references [14–18] as compared to the results of our measurements. Note that in Ref. [15] values depend on the exchange integral and also on the arrangement, AFM or FM. Ref. [17] showed the two lowest in energy magnetic configurations.

(n)	[14]	$[15]_{FM}$	$[15]_{AFM}$	[16]	$[17]_a$	$[17]_b$	[18]	This work
2	-	-	-	-	-	-	2	-
3	-	-	-	-	3	5	1.8	1.2
4	-	-	-	-	0	0	1.4	0.01
5	-	-	-	-	1	3	0.5	0.78
6	-	-	-	-	2	0	3	0.01
7	-	-	-	-	0.98	3.1	0.7	0.86
8	-	-	-	-	2	2	1.6	0.004
9	2.89	0-4	0-3	3	3	0.99	0.9	0.83
10	-	-	-	-	-	-	5	0.003
11	-	-	-	-	-	-	0.7	0.91
15	0	0-4	0-4	1	-	-	0.6	2.4

When it comes to the V_n clusters containing an even number of atoms, the most common is no net magnetic moment at all. There are however some exceptions, such as V_{22}, V_{26} and V_{28}, which have magnetic moments of around 3 μ_B for V_{26} and V_{28}, and only 1.5 μ_B for V_{22}. In Fig. 3.3 the evolution of the magnetic moments for all studied V_n clusters is represented, both for 25 K and 40 K. In addition, table 3.1 compares our measured values with the calculated ones.

Note that in some cases, such as that of V_5 in Fig. 3.2, a loss of cluster signal in the deflected profile can be noticed. Most probably this happens due to insufficient detection area in the mass spectrometer. In all such cases, deflections were re-measured in lower fields. Thus, in Fig. 3.4 the deflection profiles for V_3 and V_5 clusters are shown, this time using a smaller magnetic fields. Interestingly, for V_3 the undeflected component is much larger than it was for the rest of small clusters shown in Fig. 3.2 above.

3.2.2 Influence of source parameters

An important question to check was the behavior of spin relaxation as a function of temperature as well as other source parameters, responsible for thermalization of the cluster beam. Therefore, in the next step, we have studied the deflection profiles at different temperatures, such as 40 K, 70 K and 100 K. In Fig. 3.5 the obtained profiles at 40 K are shown, again using the maximum magnetic field of 2.4 T. This time not all the clusters are shown, as there are no major changes from what was observed in Fig. 3.2.

Oppositely to this, at 70 K the effects of temperature are noticeable. In Fig. 3.6
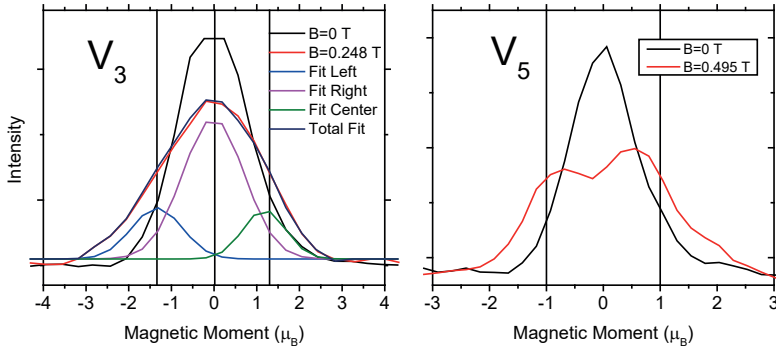
Figure 3.4: Magnetic deflections of V_3 and V_5. As for V_3 the splitting is not obvious the Gaussian fits are shown.

it can be seen that superparamagnetic clusters barely deflect, which in part is due to the higher velocity. For the smaller atomic-like clusters the deflections are much smaller than for the previous temperatures, but for larger clusters we barely see any deflection. This clearly hints why Douglass et al. did not measure any deflection as their magnetic field was smaller and their temperature was even higher.

The deflections are even more decreased if the temperature is increased to 100 K as shown in Fig. 3.7. For the smallest clusters deflections can be observed, but they are really small. It is important to note that for this measurement the velocity of the cluster beam is 900 m/s, which gives the particles less than half of the time to interact with field, as compared to 25 K, where the velocity was around 400 m/s. This results in almost non detectable deflections.

To conclude this part, a comparison between the relaxation at 40 K and 100 K is shown for V_7 at Fig. 3.8. It can be seen that the relaxation is clearly increased as the temperature increases. At 40 K all three peaks are comparable in size, while at 100 K the difference between the undeflected peak and the peaks for ± 1 μ_B is very strong. This evidences that the coupling between the magnetic moment and the lattice is a temperature dependent process.

Thermalization in the source

As previously mentioned, we studied V clusters extensively to characterize the performance of the setup, and many experiments were carried out. Thus, increasing the He pressure to 6 bar, which is about the maximum value allowed in the setup, showed quite some changes in the detected profiles. Results are shown in Fig. 3.9.

It can be clearly seen that the value of the undeflected peak has clearly de-

Figure 3.5: Magnetic deflections of V_n clusters at 40 K. Black line for magnetic field off, red line for magnetic field 2.4 T. Pressure was 2 bar.

creased; even a cluster as large as V_{21} has 2 peaks at ± 1 μ_B, while nothing at 0 μ_B. If we compare this with profiles of Figs. 3.2 and 3.5, the difference is clear. Moreover, also for clusters behaving superparamagnetically the deflections have somewhat increased. This shows a clear dependence of the cluster thermalization on the He pressure, as the higher pressure means that the clusters interact more with the walls of the source, exchanging energy, cooling down their degrees of freedom.

For more quantitative comparison, in Fig. 3.10 the deflections of V_{11} at 25 K are shown, at the left for a He pressure of 2 bar while at the right at a He pressure of 6 bar. To ease the comparison, the three-Gaussian fits are shown as well. It can be seen that the central peak decreases by many times when the pressure is increased to 6 bar.

As for the superparamagnetic clusters it has to be mentioned that the derived magnetic moments measured at 6 bar for the smaller ones somewhat increased

Figure 3.6: Magnetic deflections of V_n clusters at 70 K. Black line for magnetic field off, red line for magnetic field 2.4 T. Pressure was 2 bar.

Figure 3.7: Magnetic deflections of V_n clusters at 100 K. Black line for magnetic field off, red line for magnetic field 2.4 T. Pressure was 2 bar.

when compared to the measurement at 2 bar. Thus, V_{13} showed a magnetic moment of 2.40 μ_B at 2 bar, and 3.09 μ_B at 6 bar. This represents an increase around 25%. Similarly V_{15} shows an increase from 2.00 μ_B to 2.40 μ_B, around 20% increase. While both numbers still fall inside the error bar, it has to be noted that this increase is certainly due to a better thermalization. Such an increase is not observed for larger clusters, where the values oscillate, but not in such a significant manner.

Figure 3.8: Magnetic deflections of V_7 cluster at 40 K and 100 K. Black line for magnetic field off, red line for magnetic field 2.4 T. Pressure was 2 bar.

The reduced spin relaxation in better thermalized clusters clearly indicate a Raman process of spin relaxation via excited vibrational states [2, 24]. This will be discussed in more details at the end of the Chapter, in the Discussion section.

Another interesting feature of the source is the shape of the nozzle. We thus tested two different shape: a simple conical one and a nozzle with a more parabolic shape, similar to rocket engines. Though the difference is not that crucial as for different pressure values, the curved nozzle seems to improve thermalization a bit, as Fig. 3.11 shows.

The last parameter of the source which we studied was the length of the extension tube. All the previous measurements took place with an extension tube of 25 mm. In Fig. 3.12 we show the comparison between this and another one of 20 mm. Both experiments took place at 25 K, using a He pressure of 2 bar. It can be seen that the relaxation is larger for the shorter tube, which is in agreement with what one would expect. It is still interesting that such a small difference produced noticeable effect.

3.3   Niobium clusters

Niobium is a 4d metal, with electronic configuration $[Kr]4d^4 5s^1$. Niobium clusters have already been topic of interest in earlier works. One of the most relevant experimental works on pure Nb clusters is the electric deflection experiment, which showed that clusters may attain an anomalous component with sizeable electric dipole moments [25]. Further, magnetic deflection experiments on pure Nb clusters showed that at very low temperatures the clusters with an odd number of atoms deflect due to a single unpaired spin that is uncoupled from the
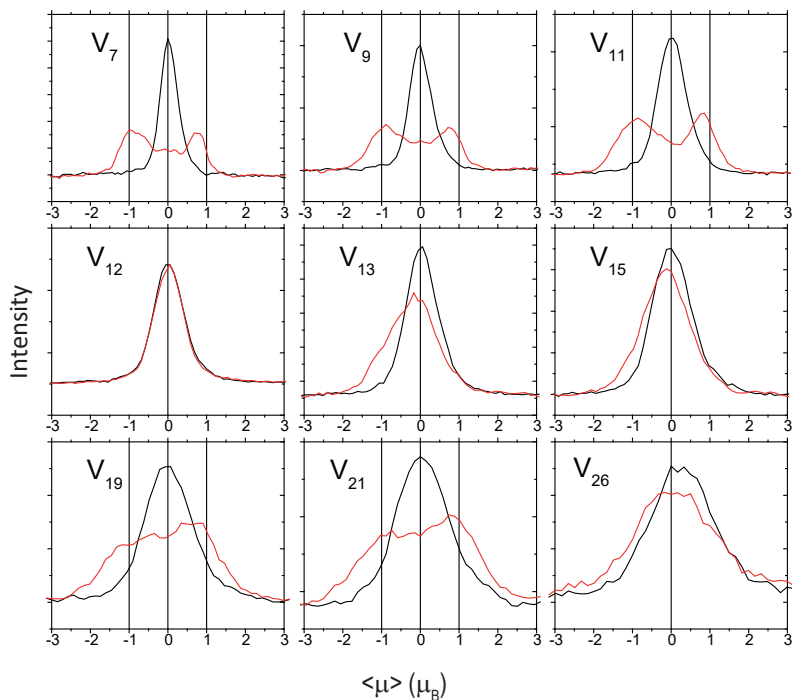
Figure 3.9: Magnetic deflections of V_n clusters at 25 K. Black line for magnetic field off, red line for magnetic field 2.4 T. Pressure was 6 bar.
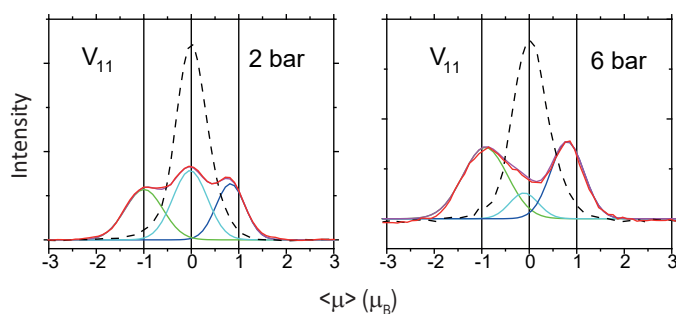
Figure 3.10: Magnetic deflections of V_{11} clusters at 25 K with different carrier gas pressure. Black line for magnetic field off, red line for magnetic field 2.4 T.

cluster lattice [13].

The goal of this section is to compare the results of the magnetic deflection
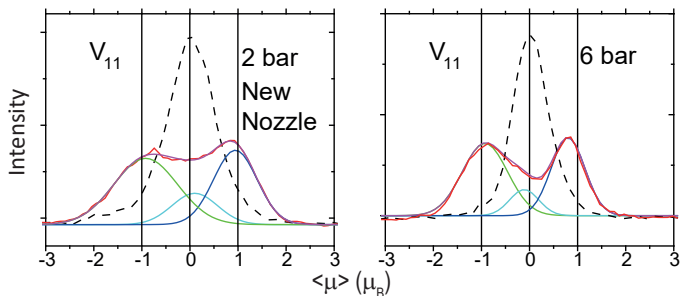
Figure 3.11: Magnetic deflections of V_{11} clusters at 25 K with different carrier gas pressure and nozzle. Black line for magnetic field off, red line for magnetic field 2.4 T.
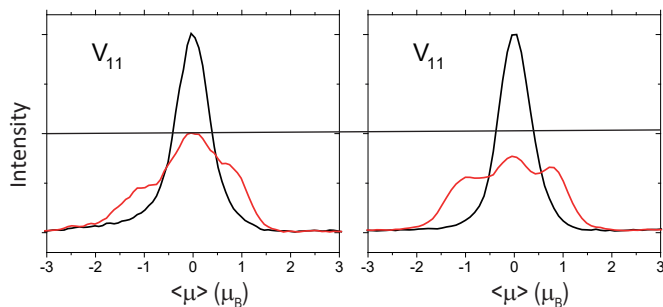
Figure 3.12: Magnetic deflections of V_{11} clusters at 25 K with different extension tube. At the left we have the deflection for a 20 mm extension tube, while at the right we have the deflection for a 25 mm, the one shown in the previous section. Black line for magnetic field off, red line for magnetic field 2.4 T.

experiments with the ones of Ref. [13], in particular, to compare the deflection profiles.

3.3.1 Deflection profiles and magnetic moments of Nb clusters

The results of the magnetic deflection experiment carried out at 25 K is shown in Fig. 3.13. What hits the eye is that the deflection profiles are very different from the ones of Moro et al., [13] even though the magnetic moments obtained are quite similar, as can be seen in Fig. 3.14.

Similar to V, the alternation of magnetic/non-magnetic for clusters containing an odd/even number of atoms is also characteristic for Nb_n clusters. Also here the magnetic moment is caused by a single unpaired electron, which gives a net
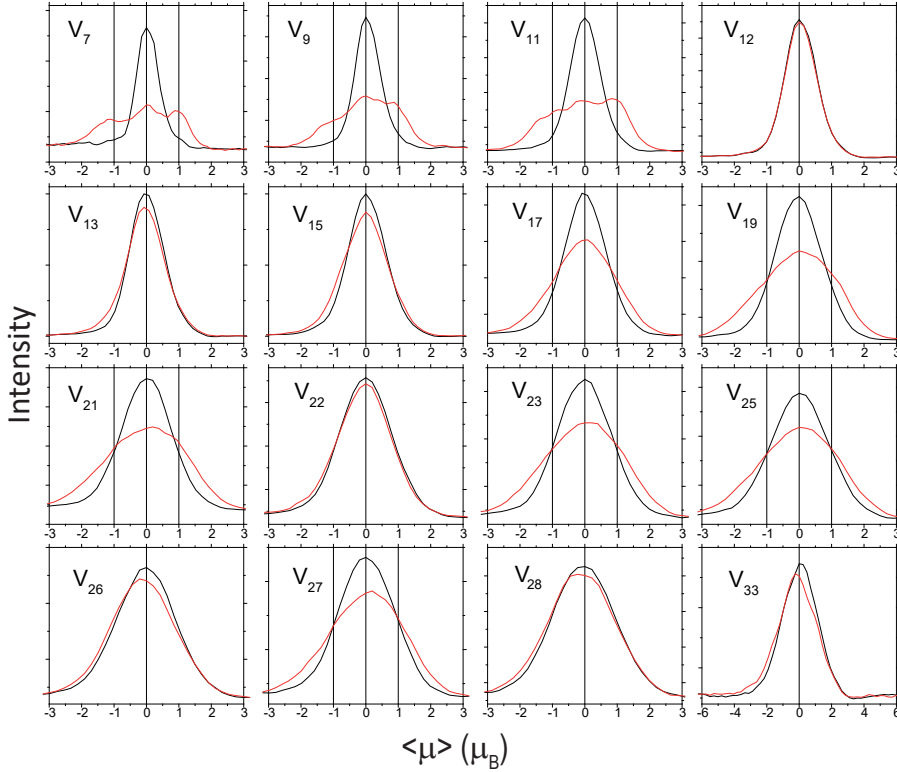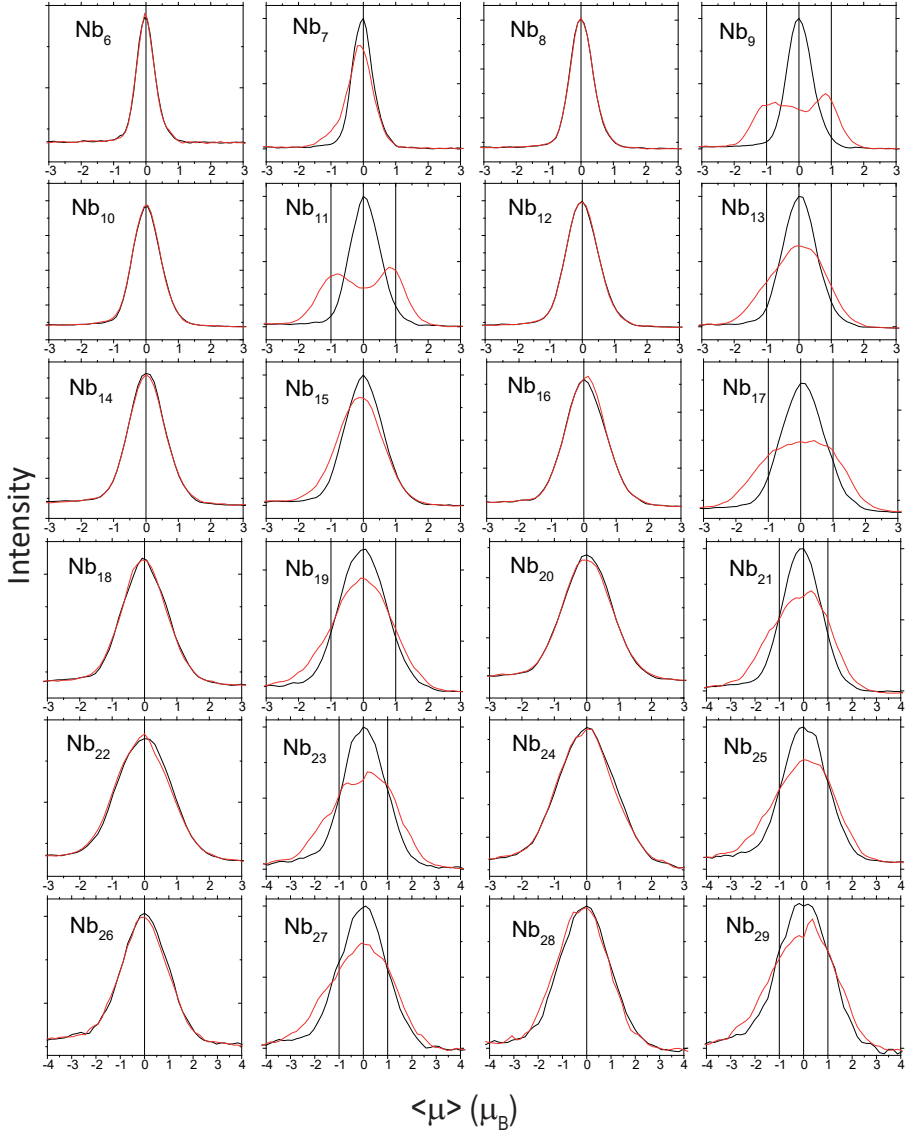
Figure 3.13: Magnetic deflections of Nb$_n$ clusters at 25 K. Black line for magnetic field off, red line for magnetic field 2.4 T. Pressure was 2 bar.

magnetic moment of 1 μ_B. Nb$_7$ and Nb$_{15}$ exhibit superparamagnetic behavior, with net magnetic moments around 3 μ_B. Both V and Nb are superparamagnetic
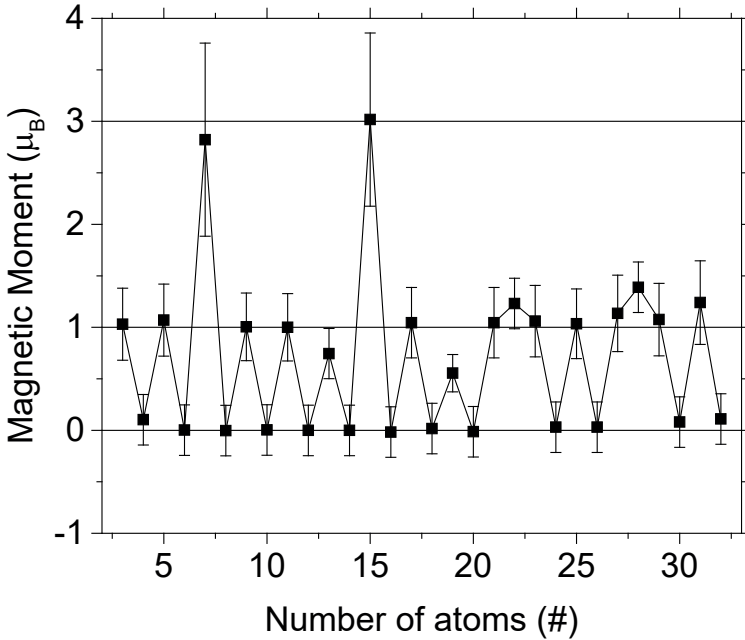
Figure 3.14: Magnetic moments of Nb_n clusters as function of size.

at n=15. Interestingly, Nb_{13} and Nb_{19} have a magnetic moment lower than those of the rest of clusters containing an odd number of atoms, similarly to what happened for V_{17}, 0.6 μ_B.

As was also observed in the previous section, a magnetic field of 2.4 T is too large to study the deflections of the smallest clusters. Though Nb is heavier than V, also here lower magnetic fields need to be used for smaller clusters, as shown in Fig. 3.15.

If we compare with the work of Moro et al. [13], there are small differences in the values of the magnetic moments. Partially this could be due to the difference in the available field and gradient: in our experiment maximum field was B = 2.4 T and the gradient 650 T/m, while in their experiment B = 0.91 T and the gradient 350 T/m. Therefore their fields might have been insufficient to clearly see the deflection of superparamagnetic clusters with small magnetic moments, namely Nb_7 and Nb_{15}. They reported moments even smaller than 1 μ_B [13].

The main difference, however, is in the deflection profiles of the majority of odd-numbered clusters. While for Moro et al. [13] the deflections were characterized by a large central undeflected peak and smaller broad shoulders reaching to ± 1 μ_B, in our deflections the central peak is completely absent or very much
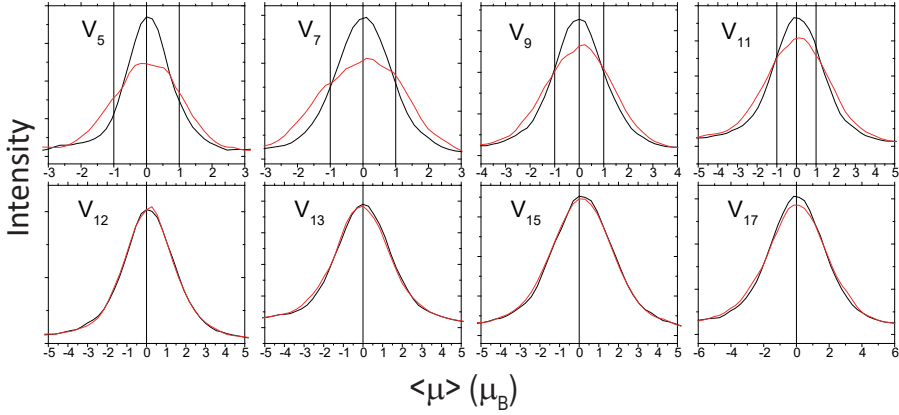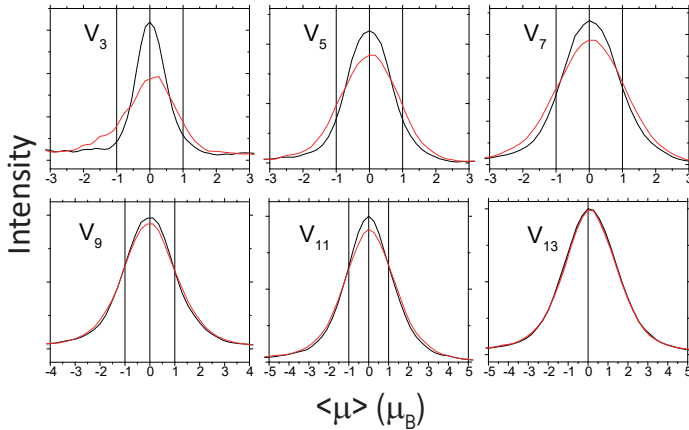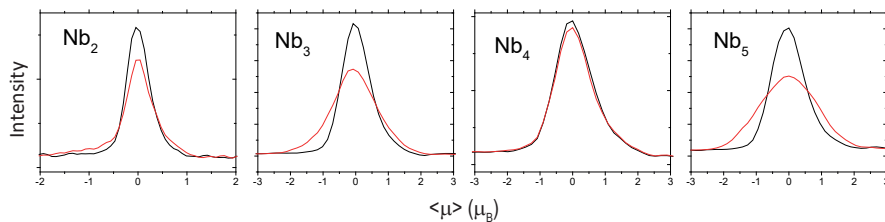
Figure 3.15: Magnetic deflections of Nb$_n$ clusters at 25 K. Black line for magnetic field off, red line for magnetic field 1 T . Pressure was 2 bar.

reduced compared to the ones at ± 1 μ_B. Nb$_9$ and Nb$_{11}$ clearly evidence this. It is also interesting to note that this experiment took place for a He pressure of 2 bar only. Even then the thermalization was sufficient.

3.3.2 Influence of source parameters

It is interesting to follow the temperature dependence for Nb clusters as well. Similarly as it happened for V clusters, a decrease in the deflections is expected upon temperature increase. In Fig. 3.16 deflections at 40 K are shown. Note that only the smaller odd-numbered clusters are shown. Clearly, at a temperature of 40 K the spin relaxation starts taking place.
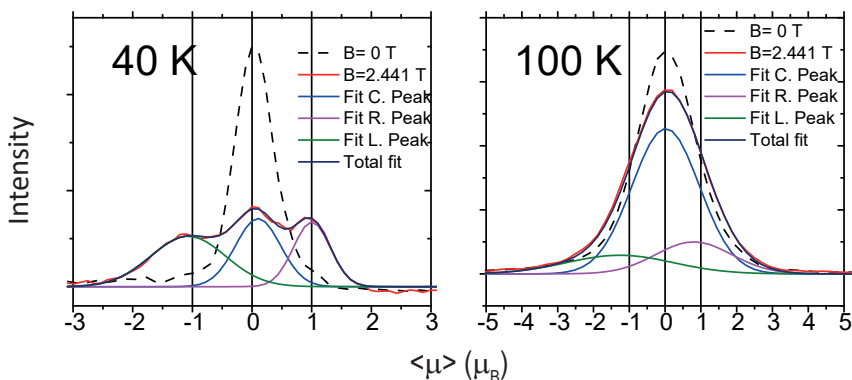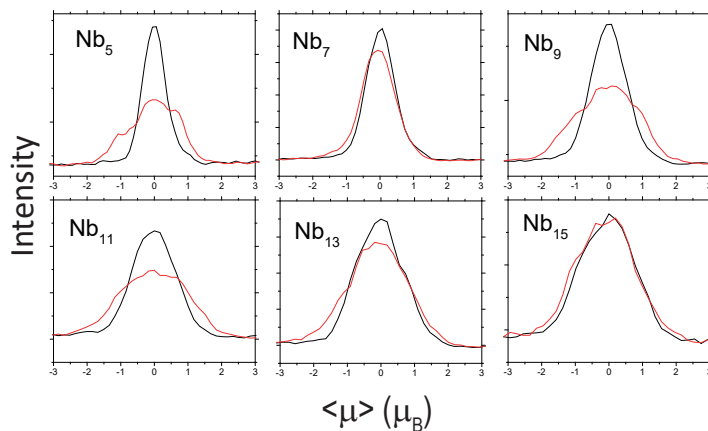

Figure 3.16: Magnetic deflections of Nb$_n$ clusters at 40 K. Black line for magnetic field off, red line for magnetic field 2.4 T. Pressure was 2 bar.

In a similar way as for V clusters, it was verified whether increasing the pressure could decrease the spin-relaxation or not. Unfortunately Nb$_n$ clusters

were never obtained for significantly larger pressure values. Despite of this, a way to decrease the pressure at the formation chamber is to increase its volume, which should cause a similar effect. The results of such increase are shown in Fig. 3.17, where it is clear that the spin-relaxation is increased a lot when compared to Fig. 3.13. The peaks at ± 1 μ_B cannot be distinguished by eye anymore, instead, the deflection shows a broader profile, where the Gaussian fit shows that the ± 1 μ_B are still there, but the ratio of their height to the height of the undeflected peak decreased significantly. This is underlined at Fig. 3.18, where the Gaussian fits for every peak are shown.
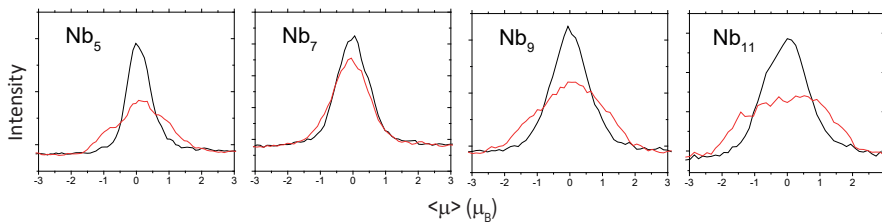
Figure 3.17: Magnetic deflections of Nb_n clusters at 25 K. Black line for magnetic field off, red line for magnetic field 2.4 T. Pressure was 2 bar. Volume of clusters formation chamber was doubled for these deflections.
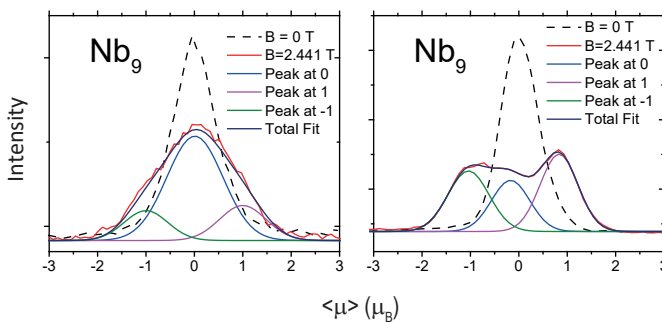
Figure 3.18: Comparison between magnetic deflections of Nb$_9$ at 25 K, for different formation chamber volume. Pressure was 2 bar. Volume of clusters formation chamber was doubled for the left image.

3.4 Tantalum clusters

Tantalum is a 5d metal, which has an electronic configuration $[Xe]4f^{14}5d^36s^2$ and it is significantly heavier than vanadium and niobium, with a mass of 180.95 atomic units, about double than niobium and more than 3 times heavier than vanadium. This makes it more challenging for precise deflection measurements. Magnetism of pure tantalum clusters has not been studied experimentally so far, at least to our knowledge, only in Ref. [13] it was briefly mentioned that their magnetic properties were similar to those of the other elements from the V group. Fa et al. [26] studied these systems theoretically and determined that the magnetic moment for an even number of tantalum atoms gives no net magnetic moment, except for Ta_2, whose magnetic moment was estimated to be 4 μ_B, while an odd number of atoms in the cluster leads to a magnetic moment of 1 μ_B.

3.4.1 Deflection profiles and magnetic moments of Ta clusters

The major difference with the previously discussed V and Nb clusters, is that Ta_n show superparamagnetic behavior for all the odd-numbered clusters. There is also the alternation magnetic/non-magnetic for odd/even number of atoms clusters, but no clusters show double sided deflections, as shown in Fig. 3.19. The velocity in these experiments was 390 m/s, while the He pressure was 2 bar.

The derived evolution of the magnetic moment with size is shown in Fig. 3.20. It can be seen that Ta_3 has a magnetic moment closer to 3 μ_B, being the cluster with the largest magnetic moment among Ta_n clusters. The net magnetic moment slowly decreases with size. Between Ta_3 and Ta_{11} all clusters having an odd number of atoms seem to have a net magnetic moment larger than 2 μ_B, with the exception of Ta_9 whose magnetic moment is slightly smaller. Larger sizes have lower magnetic moments, around 1 μ_B, which most likely is due to the unpaired electron, but oppositely to what happened for the previous materials, here the clusters with such a magnetic moment are all superparamagnetic.

3.4.2 Influence of source parameters

Since Ta clusters are superparamagnetic it is interesting to study the temperature dependence. In Fig. 3.21 deflection profiles obtained at T=40 K are shown. It can be seen that with the exception of Ta_3, due to its smaller mass, all the deflections are clearly decreased. The velocity in this experiment was 560 m/s, which together with the heavy mass of Ta makes deflections really hard to detect.

Fig. 3.22 deflections at T=60 K. The velocity for these deflections was 660 m/s. Only Ta_3 and Ta_5 are deflected enough to be distinguished by eye. Interestingly, Ta_3 for both 40 and 60 K shows a small deflection on the right side. The reason for this cannot be derived from these measurements, however.

Similarly as done in the previous sections, here we reduced the extension tube length from 25 to 20 mm. In Fig. 3.23 the deflections at 25 K with different
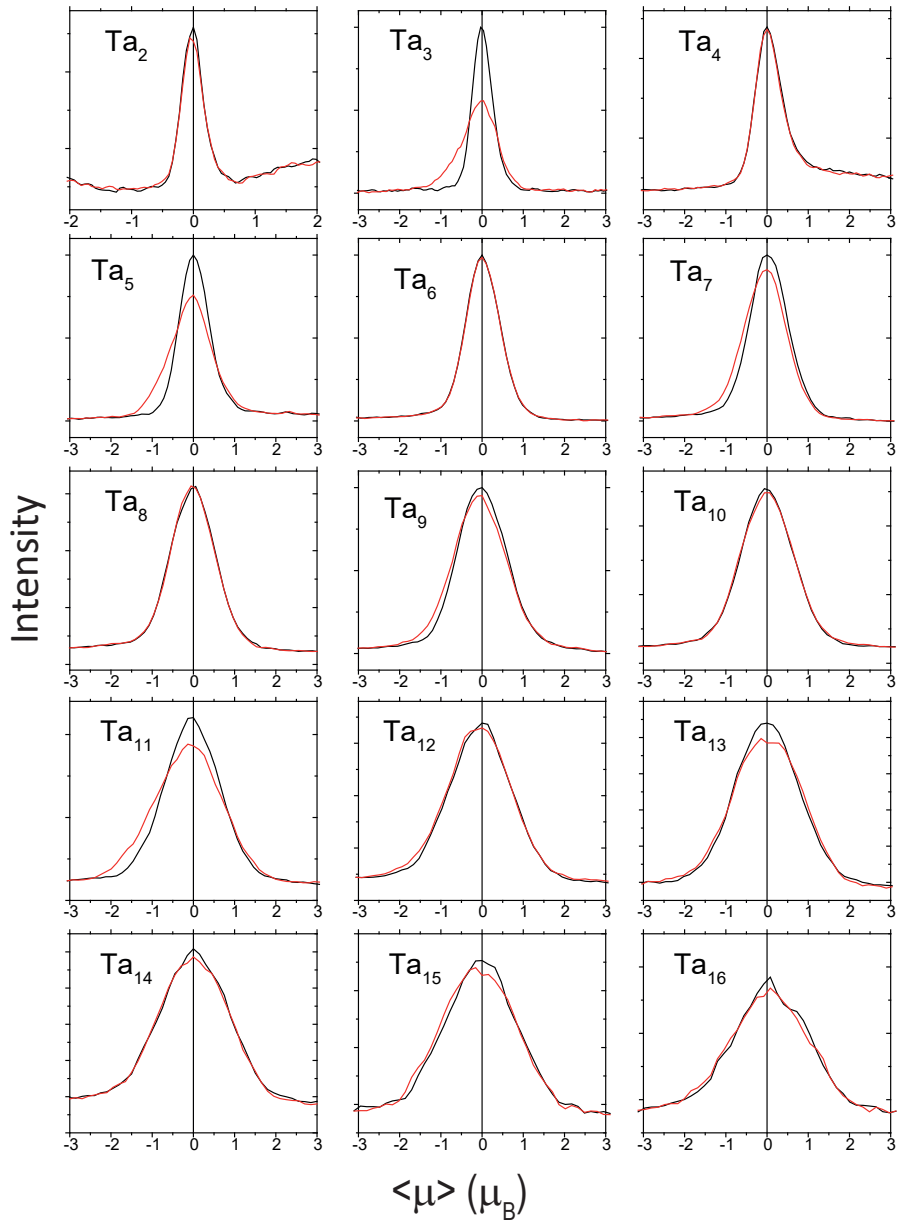
Figure 3.19: Magnetic deflections of Ta$_n$. Measurements performed at 25 K. Black line for magnetic field off, red line for magnetic field 2.4 T. Pressure was 2 bar.
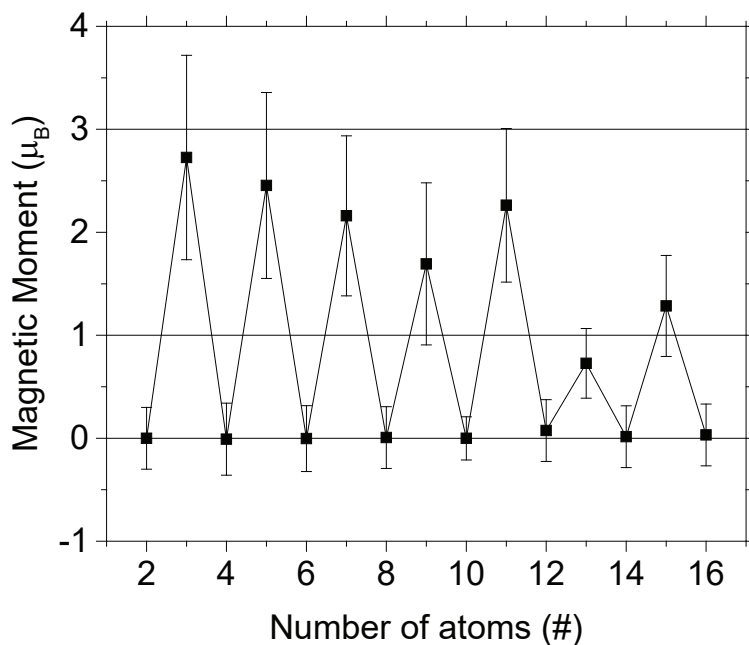
Figure 3.20: Magnetic moments of Ta$_n$ clusters as function of size.
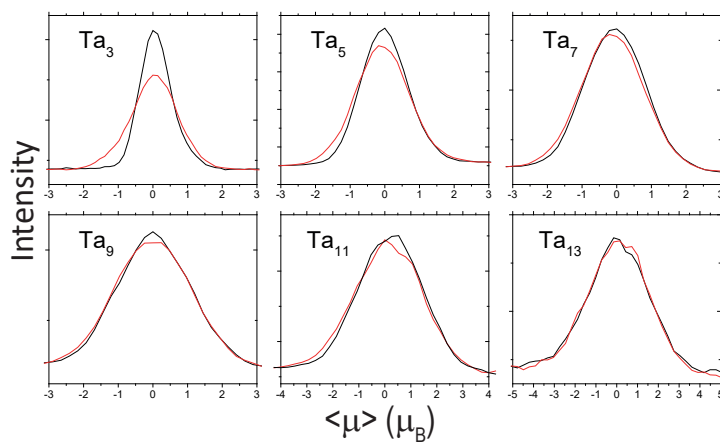
Figure 3.21: Magnetic deflections of Ta$_n$. Measurements performed at 40 K. Black line for magnetic field off, red line for magnetic field 2.4 T. Pressure was 2 bar.
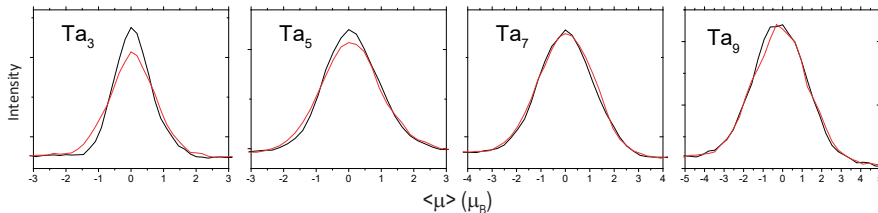
Figure 3.22: Magnetic deflections of Ta$_n$. Measurements performed at 60 K. Black line for magnetic field off, red line for magnetic field 2.4 T. Pressure was 2 bar.
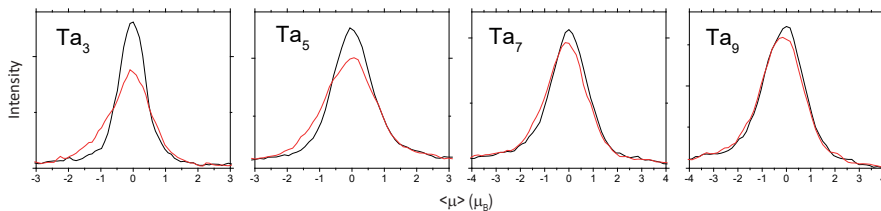
Figure 3.23: Magnetic deflections of Ta$_n$. Measurements performed at 25 K. Black line for magnetic field off, red line for magnetic field 2.4 T. Extension tube used was 20 mm instead of 25 mm.

extension tubes are shown for the smallest odd-numbered clusters. The magnetic moments measured are smaller when the extension tube is shorter as can be seen in Fig. 3.24, where we show the differences between both tubes. It can be seen that for large sizes there is no significant difference while for the smallest sizes the difference is noticeable. The velocity is also different for both cases, as by reducing the extension tube the velocity is increased from 390 m/s to 458 m/s. This indicates, once again, that by increasing the size of the tube, we force the clusters to collide more with the source, achieving a better equilibrium with source and losing excitations. The effect is more noticeable for small clusters than for large ones.

3.5   Discussion

3.5.1   Relaxation from the point of view of avoided crossing model

Double sided deflections like the ones shown in this chapter are not new. Some other works reported similar deflections. The first was Knight et al., [27], who found this undeflected peak for odd-numbered clusters of potassium. Also de
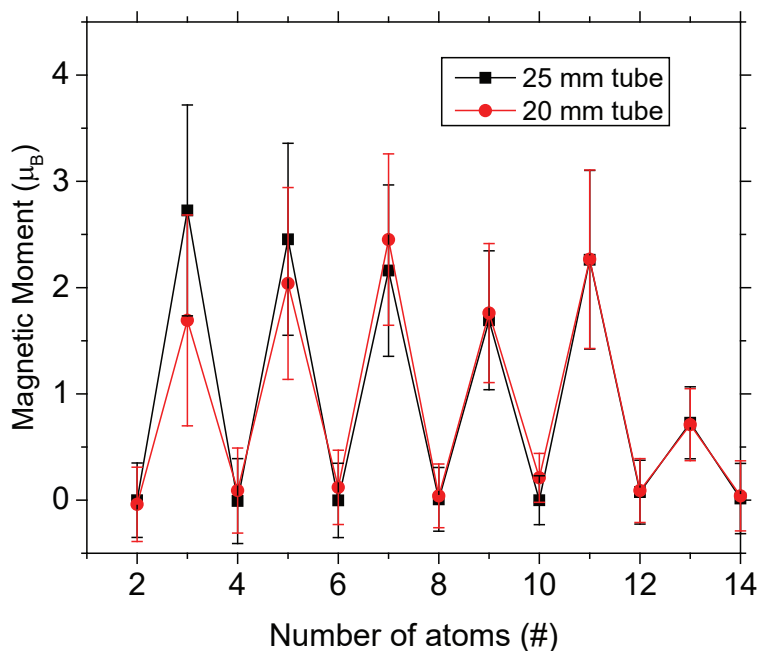
Figure 3.24: Comparison of magnetic moments of Ta_n clusters as function of size for two different extension tubes.

Heer et al., [28] showed this kind of deflections in alkali metals, see Fig. 3.25 a), Li_3, Li_5 and Na_3. There are other examples, like Y_3, shown in Fig. 2.16 above. And more recently Rohrmann et al. [29–31] found similar results for Mn doped Sn clusters.

The origin of the peaks at ± 1 μ_B is clear. But the origin of this undeflected peak at 0 μ_B is not fully understood as it was assumed to be due to spin-relaxation into lattice, but as previously mentioned this should in principle be forbidden by the Kramers degeneracy theorem.

De Heer et al. [28] explained it using the Zeeman diagram of a rotating sodium trimer, shown at Fig. 3.25 b). Two groups of parallel levels originate from each rotational level. Since the magnetic moment equals $\partial E / \partial H$, the rising levels correspond with +1 μ_B and the down going states with -1 μ_B. Zeeman levels with the same m_J values can interact, and therefore in general their crossings will be avoided. In the top-inset a close view of such a non-crossing region is shown. The net effect is that clusters on levels within non-crossing regions have small/zero measured magnetic moments. In between these regions the magnetic moment is again ± 1 μ_B. It was assumed that the relaxation increases with the cluster size because of the increasing density of rotational states.
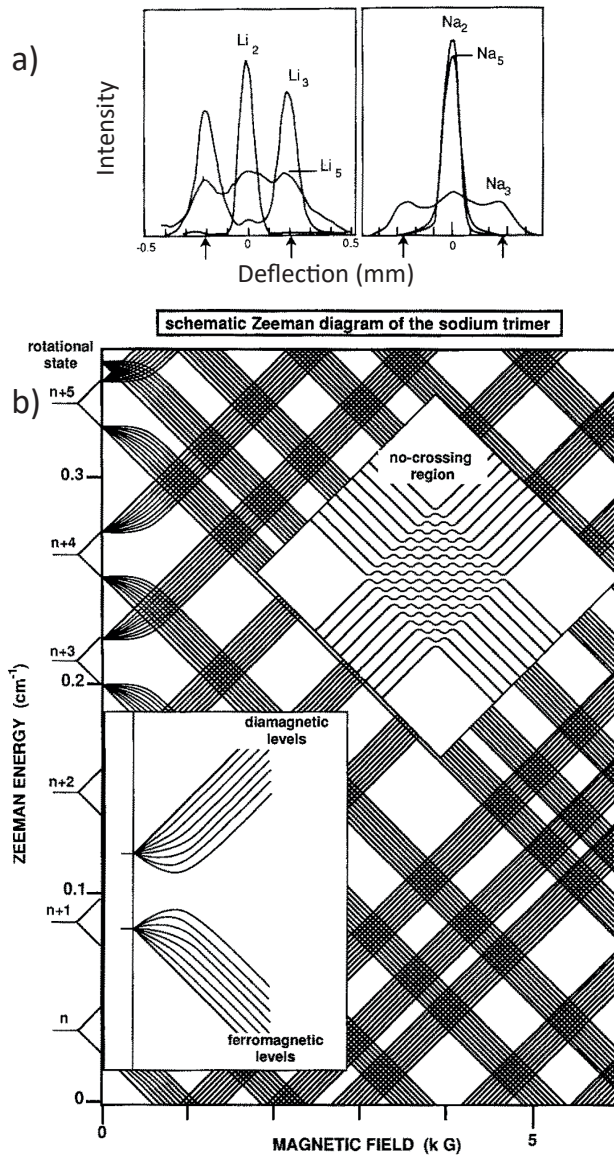
Figure 3.25: a) Magnetic deflections of small alkali clusters [28]. b) Schematic Zeeman diagram for the sodium trimer, showing hyperfine groups of compatible levels from several rotational states, giving rise to no-crossing regions (top inset) [28].

3.5.2 Kramers states and relaxation

While in the Zeeman diagram below one can understand the presence or absence of the splitting based on the avoided crossings, the fact that they are avoided (or not) requires a separate discussion. For magnets with S = 1/2 only intersite magnetic anisotropy is allowed by symmetry, and for a single quantum particle with S = 1/2 the anisotropy is absent; only Zeeman term determines spatial orientation of the spin moment at the equilibrium. However, kinetics of the magnetic moment is important. Generally speaking, one can expect that, due to spin-lattice relaxation, angular momentum will be transferred back and forth to rotational degrees of freedom of the cluster as a whole, and the initial state spin-up $|\uparrow>$ will be transformed into a superposition $\alpha |\uparrow>|0>+\beta |\downarrow>|1>$ where $|0>$ is the ground rotational state of the cluster and $|1>$ is an excited state with z-projection of rotational momentum equal to one (for simplicity, we consider here as an example only the case of zero temperature). If the spin-lattice interaction energy is higher than the rotation energy quantum one could expect $| \alpha |\approx| \beta |$, and the average spin of the cluster will be close to zero; no deflection could be expected in such a situation. However, the time of angular momentum transfer from the spin to the rotational degrees of freedom τ_{S-Lat} should be compared with the flight time t_{fl}; the condition of the deflection reads $\tau_{S-Lat}>t_{fl}$. Different clusters are different by the values of τ_{S-Lat}. We have to discuss therefore physical mechanisms which determine this quantity.

Spin-lattice relaxation processes (for brevity, we will call them below spin-flips) are dramatically different in the systems with integer and half-integer spins. In the latter case the Kramers theorem claims that time-reversal symmetry (which includes spin reversal) guarantees double degeneracy of all energy levels [32]. This means, in particular, that for the systems with total spin S = 1/2, 3/2, ... neglecting the effects of external magnetic field H, no static perturbation can induce the spin-flips ("Van Vleck cancellation" [2, 3]). Dynamical processes such as vibrations can break the symmetry and lead to spin reversal but not in the lowest order: either two-phonon processes or relaxation via excited states should be involved (Raman and Orbach processes, respectively [2, 3, 24]). Both these processes are strongly suppressed at low temperatures T. Their probability vanishes in the limit T → 0 exponentially for the Orbach processes

$$1/\tau_{S-Lat} \propto exp^{(-\Delta/k_B T)}, \tag{3.5}$$

where Δ is the energy of the excited state involved. As for the Raman processes, in the absence of magnetic field [3]

$$1/\tau_{S-Lat} \propto T^9/\Delta^4 v^{10}, \tag{3.6}$$

where v is the sound velocity; in the presence of magnetic field H, the Kramers theorem is violated and additional term $1/\tau_{S-Lat} \propto H^2 T^7$ arises which is typically

much smaller than (3.6).

For non-Kramers systems (integer S) the spin-flip probability can be estimated as

$$1/\tau_{S-Lat} \propto T^7/\Delta^2 v^{10}, \tag{3.7}$$

and is much higher than (3.6) if thermal energy is much smaller than the energy of relevant electron excitations: $k_B T \ll \Delta$. Therefore, if we are looking for the systems with anomalously long-lived total spins, we should focus our attention to the Kramers systems only.

Even within this class of systems, the case S = 1/2 is special, due to the absence of magnetic anisotropy. For S > 1/2, one can build an effective Hamiltonian of magnetic anisotropy for the ground-state multiplet, e.g.

$$\hat{H} = K\left(\hat{S}_z^2 - \frac{1}{3}S(S+1)\right) + E\left(\hat{S}_x^2 - \hat{S}_y^2\right) - \mu_B \hat{S}\hat{g}\mathbf{H}, \tag{3.8}$$

(see, e.g., Ref. [4]). Then, one can consider modulation of the anisotropy parameters K and E by atomic vibrations, etc. However, for the case S = 1/2 the rigid-spin approximation is inapplicable in principle and multi-spin character of the Hamiltonian should be taken into account [33]. In this case, the crucial role is played by Dzialoshinskii-Moriya (DM) interactions [34, 35]. Formally, this is the main relativistic interaction in magnetism since it is of the first-order in spin-orbit coupling constant whereas the magnetic anisotropy is, at least, of the second-order. It vanishes however in high-symmetry systems where each of magnetic couples has inversion center. In magnetic molecules like V_{15} or Mn_{12} this is typically not the case, and DM interactions play a crucial role in their magnetic properties [36–41], including, probably, the magnetic tunneling [38, 39]. Importantly, DM interactions do not conserve the total spin initiating transitions between the states with different multiplicity (in the lowest order, $S \mapsto S \pm 1$). The spin-flip processes in this case involve virtually excited states with S > 1/2, each of elementary step of such transitions involve a small parameter D/J where D and J are characteristic values of DM and exchange interactions, respectively. For magnetic clusters with S = 1/2 DM interaction should be the main factor responsible for the spin flips, similar to the case of V_{15} [33, 39]. For S = 3/2 additional channels of magnetic relaxation arise due to possibility of anisotropy-induced transitions within the ground state multiplet, according to the Hamiltonian 3.8.

Ta is heavier than V and Nb which has two important consequences. First, the spin-orbit coupling and therefore the value of DM interactions should be much higher in Ta clusters than in those of V and Nb. Second, the phonon frequencies are lower, which should essentially increase the probability of the Raman relaxation processes: their probability according to Eq. 3.6, is proportional to $1/v^{10} \propto M^5$ where M is the nuclear mass. It is impossible to say without quite cumbersome calculations which factor is more important but, anyway, they both work in the same direction.

3.6 Conclusions

Our experiments have clearly demonstrated the presence of Kramers blocking of spin-lattice relaxation in clusters of V group elements that are large as V_{21}. This blocking can be lifted by either Raman relaxation via an excited vibrational state, or by Orbach mechanism in clusters with larger magnetic moments. The relaxation is clearly more efficient in clusters with larger nuclear mass such as Ta. These results thus demonstrate that gas-phase clusters represent an ideal model system to study quantum coherent phenomena at practically macroscopic scales.

References

[1] H. A. Kramers, "Théorie générale de la rotation paramagnétique dans les cristaux," Proc. Amsterdam Acad. **33**, 959 (1930).

[2] J. H. Van Vleck, "Paramagnetic Relaxation Times for Titanium and Chrome Alum," Phys. Rev. **57**, 426-447 (1940).

[3] R. Orbach, "Spin-lattice relaxation in rare-earth salts," Proc. Rev. Soc. A. **264**, 458-484 (1961).

[4] S. Gómez-Coca, A. Urtizberea, E. Cremades, P. J. Alonso, A. Camón, E. Ruiz, and F. Luis, "Origin of slow magnetic relaxation in Kramers ions with non-uniaxial anisotropy," Nat. Comm. **5**, 4300 (2014).

[5] K. S. Pedersen, J. Dreiser, H. Weihe, R. Sibille, H. V. Johannesen, M. A. Sørensen, B. E. Nielsen, M. Sigrist, H. Mutka, S. Rols, J. Bendix, and S. Piligkos, "Design of Single-Molecule Magnets: Insufficiency of the Anisotropy Barrier as the Sole Criterion," Inorg. Chem. **54**, 7600-7606 (2015).

[6] W. A. de Heer, "The physics of simple metal clusters: experimental aspects and simple models," Rev. Mod. Phys. **65**, 611-676 (1993).

[7] P.-G. Reinhard, E. Suraud, *Introduction to Cluster Dynamics* (Wiley-VCH, 2003).

[8] J. A. Alonso, "Electronic and Atomic Structure, and Magnetism of Transition-Metal Clusters," Chem. Rev. **100**, 637-677 (2000).

[9] I. M. L. Billas, A. Châtelain and Walt A. de Heer, "Magnetism from the Atom to the Bulk in Iron, Cobalt, and Nickel Clusters," Science. **265**, 1682 (1994).

[10] I. M. L. Billas, J. A. Becker, A. Châtelain, and W. A. de Heer, "Magnetic

moments of iron clusters with 25 to 700 atoms and their dependence on temperature," Phys. Rev. Lett. **71**, 4067 (1993).

[11] X. Xu, S. Yin, R. Moro, and W. A. de Heer, "Magnetic moments and adiabatic magnetization of free cobalt clusters,"Phys. Rev. Lett. **95**, 237209 (2005).

[12] L. Peters, I. Di Marco, O. Grånäs, E. Şaşıoğlu, A. Altun, S. Rossen, C. Friedrich, S. Blügel, M. I. Katsnelson, and A. Kirilyuk and O. Eriksson, "Correlation effects and orbital magnetism of Co clusters," Phys. Rev. B. **93**, 224428 (2016).

[13] R. Moro, S. Yin, X. Xu, and W. A. de Heer, "Spin Uncoupling in Free Nb Clusters: Support for Nascent Superconductivity," Phys. Rev. Lett. **93**, 086803 (2004).

[14] F. Liu, S. N. Khanna, and P. Jena, "Magnetism in small vanadium clusters," Phys. Rev. B. **43**, 8179 (1991).

[15] J. Dorantes-Dávila and H. Dreyssé, "Magnetic behavior of small vanadium clusters," Phys. Rev. B. **47**, 3857 (1993).

[16] K. Lee and J. Callaway, "Electronic structure and magnetism of small V and Cr clusters," Phys. Rev. B. **48**, 15 358 (1993).

[17] X. Wu and A. K. Ray, "A density functional study of small neutral and cationic vanadium clusters V_n and V_n^+ (n=2-9)," J. Chem. Phys. **110**, 2437 (1999).

[18] J. Zhao, X. Chen, Q. Sun, F. Liu, G. Wang, and K. D. Lain, "Tight-binding study of the structural and magnetic properties of vanadium clusters," Phys. B. **215**, 377-382 (1995).

[19] P. Alvarado, J. Dorantes-Dávila, and H. Dreyssé, "Structural effects on the magnetism of small vanadium clusters," Phys. Rev. B. **50**, 1039 (1994).

[20] D. C. Douglass, J.P. Bucher, and L. A. Bloomfield, "Magnetic studies of free nonferromagnetic clusters," Phys. Rev. B. **45**, 6341 (1992).

[21] S. Blundell, *Magnetism in Condensed Matter* (Oxford University Press, Oxford, 2001).

[22] M. B. Knickelbein, "Spin relaxation in isolated molecules and clusters: The interpretation of Stern-Gerlach experiments," J. Chem. Phys. **121**, 5281 (2004).

[23] M. B. Knickelbein, "Magnetic ordering in clusters of the group 3 transition elements: Sc_n, Y_n, and La_n," Phys. Rev. B. **71**, 184442 (2005).

[24] A. Abragam and B. Bleaney, Electron Paramagnetic Resonance of Transition Ions (Oxford Univ. Press, Oxford, 1970).

[25] R. Moro, X. Xu, S. Yin, and W. A. de Heer, "Ferroelectricity in free niobium clusters," Science. **300**, 1265-1269 (2003).

[26] W. Fa, C. Luo, and J. Dong, "Coexistence of ferroelectricity and ferromagnetism in tantalum clusters," J. Chem. Phys. **125**, 114305 (2006).

[27] W. D. Knight, R. Monot, E. R. Dietz and A. R. George, "Stern-Gerlach Deflection of Metallic-Cluster Beams," Phys. Rev. Lett. **40**, 1324-1326 (1978).

[28] W. A. de Heer, P. Milani, and A. Châtelain, "Magnetic properties of free alkali and transition metal clusters," Z. Phys. D. **19**, 241-245 (1991).

[29] U. Rohrmann, and R. Schäfer, "Stern-Gerlach Experiments on Mn@Sn12: Identification of a Paramagnetic Superatom and Vibrationally Induced Spin Orientation," Phys. Rev. Lett. **111**, 133401 (2013).

[30] U. Rohrmann, P. Schwerdtfeger, and R. Schäfer, "Atomic domain magnetic nanoalloys: interplay between molecular structure and temperature dependent magnetic and dielectric properties in manganese doped tin clusters," Phys. Chem. Chem. Phys. **16**, 23952 (2014).

[31] U. Rohrmann, and R. Schäfer, "Stern-Gerlach Experiments on Fe@Sn12: Magnetic Response of a Jahn-Teller Distorted Endohedrally Doped Molecular Cage Cluster," J. Phys. Chem. C **119**, 10958-10961 (2015).

[32] L. D. Landau and E. M. Lifshitz, *Quantum Mechanics* (Pergamon, Oxford, 1977).

[33] B. Barbara, I. Chiorescu, W. Wernsdorfer, H. Bogge, and A. Muller, "The V_{15} Molecule, a Multi-Spin Two-Level System: Adiabatic LZS Transition with or without Dissipation and Kramers Theorem," Prog. Theor. Phys. Suppl. **145**, 357 (2002).

[34] I. Dzyaloshinsky, "A thermodynamic theory of "weak" ferromagnetism of antiferromagnetics," J. Phys. Chem. Solids. **4**, 241 (1958).

[35] T. Moriya, "New Mechanism of Anisotropic Superexchange Interaction," Phys. Rev. Lett. **4**, 228 (1960).

[36] B. Barbara, L. Thomas, F. Lionti, A. Sulpice, and A. Caneschi, J. Magn. "Quantum resonance of the magnetisation in a single-crystal of Mn_{12}-ac," Magn. Mater. **177**, 1324 (1998).

[37] M. I. Katsnelson, V. V. Dobrovitski, and B. N. Harmon, "Many-spin interactions and spin excitations in Mn_{12}," Phys. Rev. B. **59**, 6919 (1999).

[38] H. A. De Raedt, A. H. Hams, V. V. Dobrovitski, M. Al-Saqer, M. I. Katsnelson, and B. N. Harmon, "Many-spin effects and tunneling splittings in Mn_{12} magnetic molecules," J. Magn. Magn. Mater. **246**, 392 (2002).

[39] H. A. De Raedt, S. Miyashita, K. Michielsen, and M. Machida, "Dzyaloshinskii-Moriya interactions and adiabatic magnetization dynamics in molecular magnets," Phys. Rev. B. **70**, 064401 (2004).

[40] M. I. Belinsky, Chem. Phys. **361**, 137 (2009); Chem. Phys. **361**, 152 (2009).

[41] V. V. Mazurenko, Y. O. Kvashnin, F. Jin, H. A. De Raedt, A. I. Lichtenstein, and M. I. Katsnelson, "First-principles modeling of magnetic excitations in Mn_{12}," Phys. Rev. B. **89**, 214422 (2014).

4 Magnetic properties of Co doped Nb and V clusters

In chapter 3 the magnetic deflection of V and Nb clusters was studied, thus demonstrating that these clusters are non-magnetic or barely magnetic. Here, these clusters are doped with a single magnetic impurity, Co, which is widely known as a classic magnetic material. The idea was to investigate whether a single magnetic 3d atom can induce any magnetization in the nominally non-magnetic clusters made of light 3d or 4d elements. Stern-Gerlach deflection experiments were used to obtain the net magnetic moments of the clusters, for both Nb and V clusters doped with Co. Further the vibrational spectra of the most interesting subset of Co doped Nb clusters were measured, and then compared with the results of DFT calculations. This resulted in well-defined geometries of these clusters, that could further serve as input for theory. From them the magnetic moments were also calculated. After this, the Anderson impurity model was used in an attempt to understand the mechanism responsible for quenching of the Co magnetic moment. The possibility of Kondo screening was considered as well. [*]

4.1   Introduction

Electronic correlations constitute the basis of condensed matter physics and are responsible for the enormous wealth of phenomena found in solids, such as (high-T_c) superconductivity [1], charge- and spin-ordering [2] and fluctuations [3], colossal magnetoresistance [4], metal-insulator transition [5], half-metallicity [6], quantum Hall effect [7], heavy fermion behavior [8], etc. Reducing the size, however, leads to an extreme sensitivity of these properties to the atomic arrangement, shape, and the effects of the environment. The understanding and control of these size-driven processes is therefore crucial to maintain the pace of developments in nanoscience.

In this miniaturization trend, the ultimate limit is represented by atomic clusters. Such clusters are particles composed of a countable number of atoms, from the diatomic limit up to some thousands or tens of thousands of atoms [9]. Quantum confinement effects entirely govern the behavior of matter in this size regime. The discretized electronic levels lead to sudden changes of the cluster properties, for example when changing the cluster size on an atom-by-atom basis. In the semiconductor technology there is a long-standing interest in systems with discrete energy spectra, such as quantum wells [10] and quantum dots [11].

Obviously the consideration of doped or alloyed, instead of pure clusters offers an even broader playground for technological applications. However, doped clusters are also very interesting from a fundamental point of view. For example, it is well known that already for a single magnetic impurity in a non-magnetic metallic host interesting phenomena like Friedel oscillations [12] and the Kondo effect [13] can occur. How or would such effects be present in clusters? Furthermore, the case of a single magnetic impurity embedded in a discrete host like a cluster offers a sensitive probe of studying the dependence of the local magnetic moment on the details of the discrete energy spectrum. This could lead to valuable insight in processes reducing the local magnetic moment and/or Kondo screening mechanisms. More precisely, the formation of the atomic magnetic moment is trivially described by the Hund's rules in the case of an isolated atom, but this process is far from trivial in the case of an atom embedded in an interacting host.

Recently, the magnetic moment of a single magnetic impurity in a discrete host was investigated in the framework of the Anderson impurity model [14]. One of the things found, was that the local moment grows with increasing host band gap (HOMO-LUMO gap). Using this relation, the experimentally observed magnetic moments of Cr doped Au clusters were successfully explained [15]. This demonstrates in particular, that the size of the measured local moment follows the trend of the calculated band gap of the host.

In this chapter we present a comprehensive study of the mechanisms governing the formation of magnetic moments in Co doped Nb clusters. From magnetic deflection experiments we make the interesting observation that some clusters are strongly magnetic, while others are completely non-magnetic, in contrast

with the Cr-Au case where all measured clusters were found to be magnetic. There are two possibilities for the absence of magnetism in the Nb_xCo clusters. Either there is no local Co magnetic moment or it is screened by the delocalized electrons of the cluster, i.e. the Kondo effect. From the theoretical perspective, the difficulty in explaining the observed magnetic behavior is in the treatment of the electronic correlations. Since it is not clear from the beginning whether correlations effects are weak, intermediate or strong, it is difficult to decide which theoretical approach is suitable. One could expect correlations to be stronger in small clusters than in their bulk counterparts due to a stronger localization of the wave-functions. On the other hand, for the clusters less screening channels are present, which could lead to an almost constant Coulomb interaction throughout the cluster [16]. This would render correlations effects to be unimportant.

Thus, the importance of correlations effects is not known for Nb_xCo clusters a-priori. To study this, first, we make a comparison of experimental vibrational spectra with those obtained from a density functional theory (DFT) study. This serves two purposes. It provides the ground state geometry of the clusters. Moreover, due to the dependence of the vibrational spectrum on the magnetic moment, the performance of DFT in predicting the magnetic moments can be investigated. Then, in order to obtain a physical understanding of the experimentally observed magnetic behavior, we perform an analysis based on the Anderson impurity model. From this analysis it is observed that the absence of a magnetic moment in the doped clusters is due to an absence of the Co moment and not the Kondo effect. In addition, the magnetic behavior of the Nb_xCo clusters can be understood from an inspection of their electronic structure. Magnetism is favored when the effective hybridization around the chemical potential is small, while the absence of magnetism is signaled by a large effective hybridization around the chemical potential.

Both Co-doped and pure Nb clusters have already been the topic of interest in earlier works. One of the most relevant experimental works on pure Nb clusters is the electric deflection experiment, which showed that cold clusters may attain an anomalous component with very large electric dipole moments [17]. Further, magnetic deflection experiments on pure Nb clusters showed that at very low temperatures the clusters with an odd number of atoms deflect due to a single unpaired spin that is uncoupled from the cluster lattice [18, 19]. Far-infrared absorption spectra of small neutral and cationic Nb clusters combined with DFT calculations have revealed their geometries [20]. Compared to pure Nb clusters, not much is known on Co-doped clusters. Experimentally an anion photoelectron spectroscopy study is performed, which showed that the addition of the Co atom for small Nb clusters induces bulk-like behavior, i.e. closing of the band gap [21]. From the theoretical side a computational study based on DFT addressed the geometric and magnetic properties finding that Nb_7Co has no net magnetic moment, which means that the magnetic moment of 6 μ_B coming from the Co atom is completely destroyed by interactions with the Nb_x host [22]. The experimental confirmation of this is however completely lacking, which is another reason for

conducting a combined experimental and theoretical study.

4.2 Co doped Nb clusters: Magnetic moments.

The magnetic deflection experiments took place in the same fashion as the ones described in the previous chapter. In order to create Co doped Nb clusters a rod consisting in $Nb_{1-y}Co_y$ (y = 5 %) was used. The typical deflection profiles, obtained at a temperature of 25 K using a helium pressure of 2 bar, are shown in Fig. 4.1. It can be seen that some clusters are magnetic while others not. Same as it happens for pure Nb clusters, there are three different behaviors. First, some clusters are not magnetic at all. The smallest cluster among them is Nb_5Co, evidenced by the total absence of deflection. Other clusters that are non-magnetic are Nb_7Co, $Nb_{15}Co$ and the rest of even-numbered clusters for n>15.

Second, there are clusters that deflect towards the direction of the strong magnetic field, thus showing the so-called superparamagnetic behavior. The superparamagnetic clusters are: Nb_3Co, Nb_4Co, Nb_6Co, Nb_9Co, $Nb_{11}Co$, $Nb_{12}Co$ and $Nb_{13}Co$. The third kind of behavior is the atomic-like one, which was also the most common behavior found for odd-numbered pure-Nb clusters in Chapter 3. The smallest cluster showing this behavior is Nb_8Co, but also $Nb_{10}Co$ and all the odd-numbered clusters with $n \geq 14$. This profile is characterized by 3 peaks, 2 peaks at ± 1 μ_B and an additional peak at 0 μ_B. The latter is explained by the fact that these deflections were measured at the carrier gas pressure of 2 bar, when some vibrational modes stay excited and the spin relaxation processes are stronger. This, however, is more of advantage than disadvantage for the purposes of this chapter.

Decreasing the applied field decreases all deflections, as a few selected profiles shown in Fig. 4.2 demonstrate.

It is also interesting to study the temperature dependence. In Fig. 4.3 the deflections for the smallest clusters are shown. The deflections are clearly decreased with respect to the ones shown for T=25 K with the same magnetic field, as could be expected, due to the larger velocity of the clusters, 510 m/s at T=40 k as compared with 410 m/s at T=25 K.

Fig. 4.4 shows the deflections at 70 K, which corresponds to the velocity of 590 m/s. It can be seen that even for the atomic-like clusters, where the spin-lattice coupling is non-existing, the deflections practically vanish.

From Fig. 4.5 it seems that the clusters can be divided into two size regions. For clusters with n≥14 the magnetic to non-magnetic behavior appears to be exactly determined by having an odd or even number of atoms in the cluster. An odd number of atoms in the cluster corresponds to the situation of at least one unpaired electron and thus at least a moment of 1 μ_B. For an even number of atoms, all the electrons can be paired. Note that the magnetic behavior of
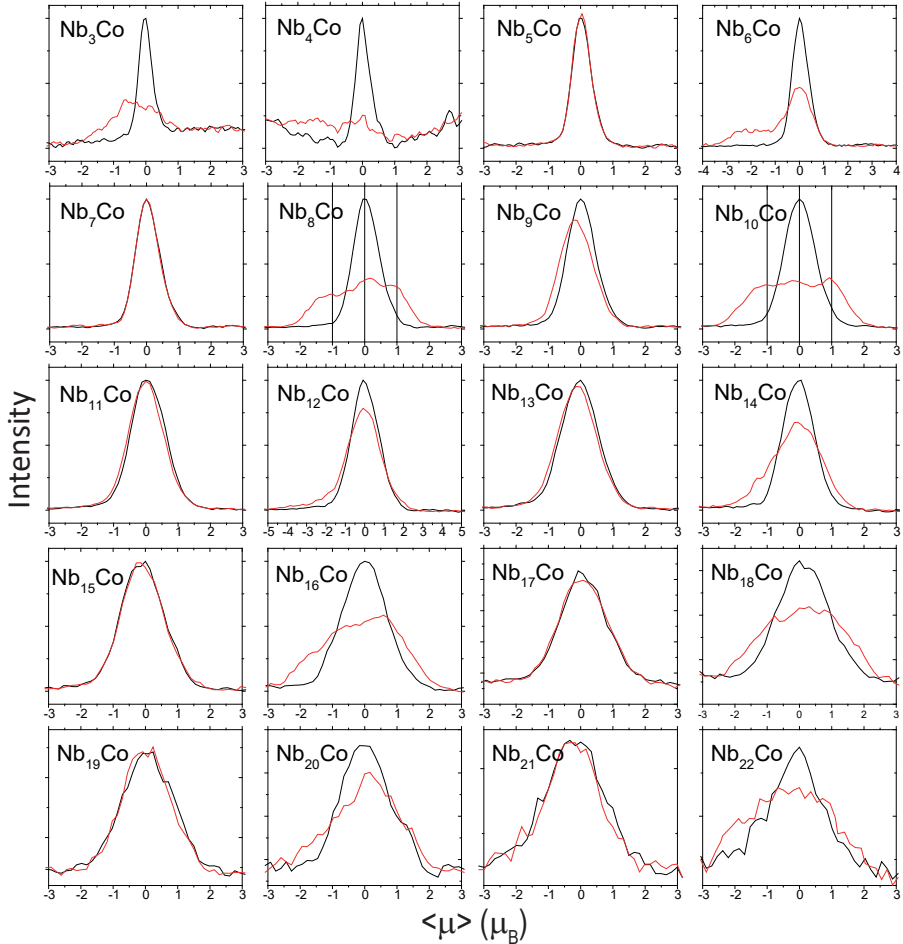
Figure 4.1: Magnetic deflections of Co doped Nb clusters measured at a temperature of 25 K and at a carrier gas pressure of 2 bar. Black line is for zero magnetic field, red line for 2.4 T.

pure Nb clusters was indeed explained in this way, see Ref. [18] and previous Chapter. Then, there is the regime of clusters with $n \leq 14$, where the magnetic behavior clearly cannot be explained due the presence or absence of a single unpaired electron. In this region strong fluctuations in the magnetic moment can be observed by just adding or removing a single Nb atom. For example, Nb_4Co is strongly magnetic, while Nb_5Co is completely non-magnetic. Then, again adding just one Nb atom leads to Nb_6Co which is again strongly magnetic. On the other hand Nb_7Co is again non-magnetic.
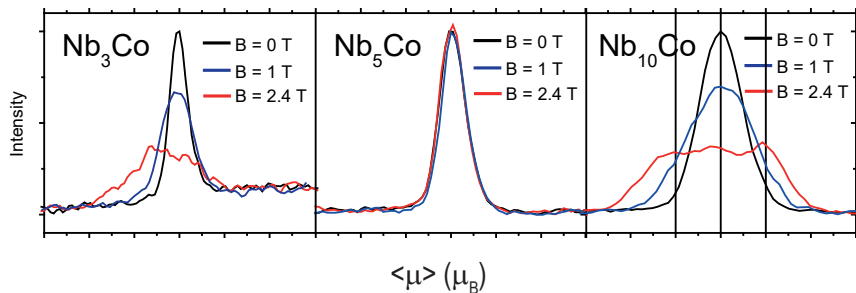
Figure 4.2: Deflections for Nb_3Co, Nb_5Co and $Nb_{10}Co$ at a temperature of 25 K, using different magnetic fields.
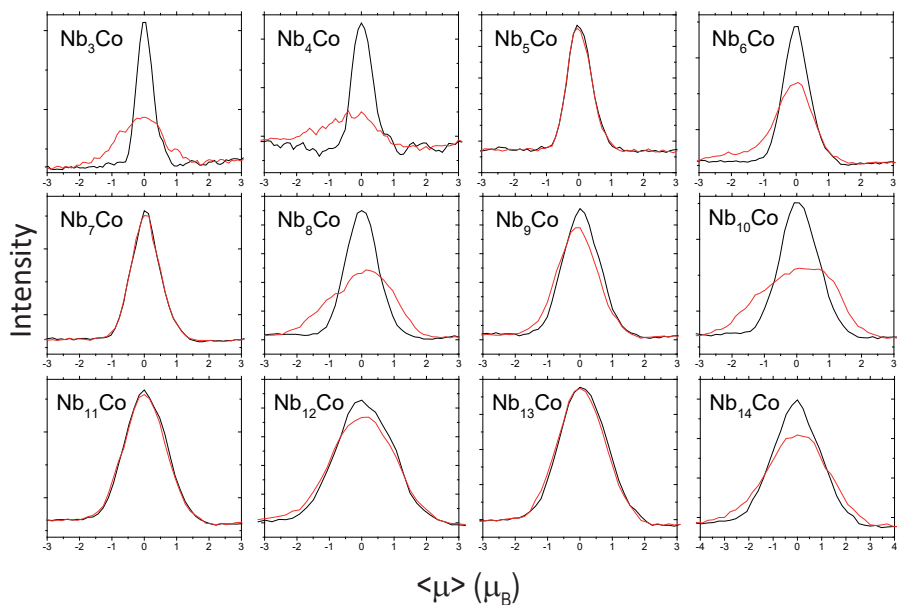
Figure 4.3: Magnetic deflections of Co doped Nb clusters at a temperature of 40 K and at the gas carrier pressure of 2 bar. Black line is for zero magnetic field, red line for 2.4 T.
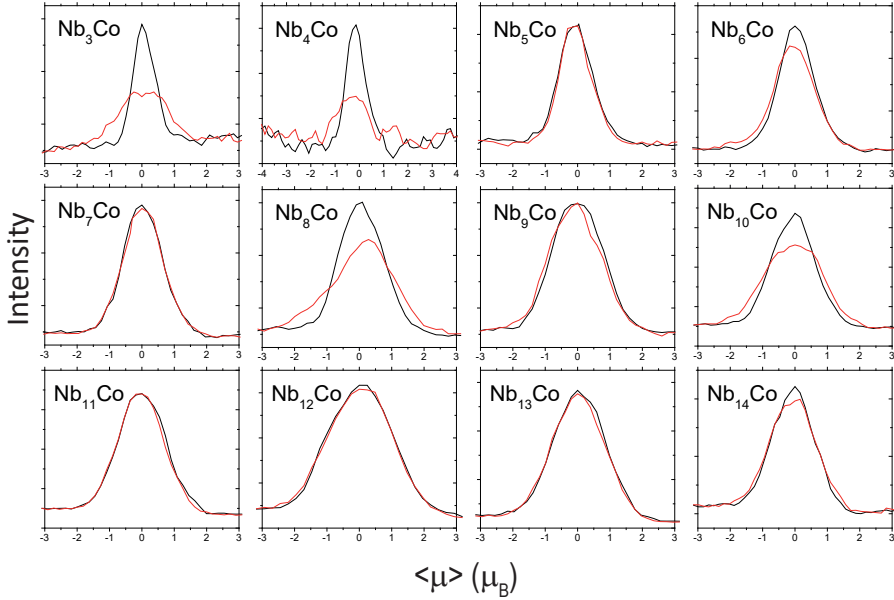
Figure 4.4: Magnetic deflections of Co doped Nb clusters at a temperature of 70 K and at the gas carrier pressure of 2 bar. Black line is for zero magnetic field, red line for 2.4 T.

It can also be observed that there is no cluster with a magnetic moment larger than that of an isolated Co atom. An isolated Co atom has 7 $3d$ electrons leading to a total moment of 6 μ_B, where both the spin and orbital moment contribute 3 μ_B. This indicates that either the Co atom is not very effective in inducing magnetic moments in the Nb_x host or a large part of the Co moment is absent due to interactions with the Nb_x host. Based on an inspection of previous works the latter explanation seems to be the most plausible. For example, in Ref. [22] it is shown by means of a DFT study on Nb_xCo clusters that roughly 20-50 % of the total magnetic moment can come from the Nb host. It should be mentioned that in this study only the spin magnetic moment was considered. However, from for example Ref. [23] and [24] it is well established for pure Co clusters that the orbital contribution can be substantial, up to 1 μ_B per Co atom. A similar observation is made for Co clusters deposited on Pt(111) [25]. Although being substantial, it is still largely quenched with respect to the 3 μ_B of the isolated atom. Besides the orbital moment of the Co atom, also its spin moment is known to be reduced in Nb_xCo [22] and pure Co clusters [23, 24, 26, 27]. For the Nb_xCo clusters it is found to be about 1-2 μ_B. Based on these observations we expect that the spin moment of the Nb_xCo clusters can be attributed to both the Nb_x host and Co atom. On the
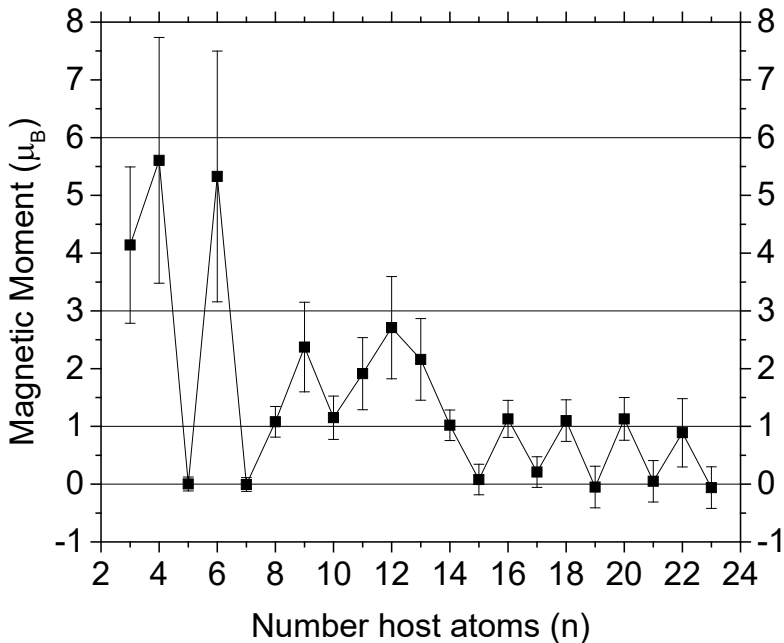
Figure 4.5: Magnetic moments of Co doped Nb clusters as function of size.

other hand the orbital moment is expected to come from the Co atom and to be substantially quenched from its atomic value.

4.3 Vibrational spectra: geometric and magnetic structure

The vibrational spectra were obtained with the help of Valeriy Chernyy, while the DFT calculation were performed by Remko Logemann. In this section a comparison between the experimental vibrational spectra with those obtained from a DFT study is performed. This serves two purposes. First, due to the dependence of the vibrational spectrum on the magnetic moment, the performance of DFT in predicting the magnetic moments can be investigated. Second, it provides the ground state geometry of the clusters. These ground state geometries are required as an input in Section 4.4 below, to obtain a physical understanding of the observed magnetic behavior from Section 4.2.

4.3.1 Experimental details

In order to record the vibrational spectra we coupled our cluster setup to the Free Electron Laser For Intra Cavity Experiments (FELICE) [28]. Below a brief description of the experimental setup is given and for more details the reader is referred to Ref. [29, 30] and Chapter 2. The clusters are produced in an ablation-type cluster source in a growth channel filled by a helium carrier gas prior to ablation of a $Nb_{1-y}Co_y$ (y = 5 %) rod by a Nd:YAG laser (532 nm). The temperature of the extension tube, which is attached to the cluster source for better cluster thermalization, is 77 K. After expansion in the source chamber, the mixture of clusters and carrier gas is skimmed. This results in the formation of a molecular beam that is shaped by a slit with a width of 0.45 mm. The interaction between the IR light and the molecular beam takes place in the center of the extraction region of the REToF mass spectrometer with a 35° angle between the two beams. The IR pulse energies inside the FELICE cavity range between 0.2 and 0.6 J over the IR scans. The IR pulse consists of a 9 μs long train of micro-pulses with 1 ns time delay between them. The clusters are ionized by a frequency doubled dye laser with a photon energy of 5.4 eV entering the extraction region at a ~90° angle with respect to the cluster beam.

The frequency of the ionizing UV laser is chosen just below the ionization potential, and in the absence of the IR laser, only a small ion yield is observed for each mass. When the IR laser is resonant, the number of neutrals that can be ionized is increased, leading to a frequency dependent gain upon ionization; all species formed are accelerated into the RETOF flight tube by extraction plates with static voltages. The experiment operates at twice the FELICE frequency which allows to record a signal with ($I_{IR+UV}(\omega)$) and without (I_{UV}) IR radiation in a shot-to-shot manner. The experimental IR curves are presented in terms of gain spectra ($G(\omega)$) calculated as

$$G(\omega) = \frac{I_{IR+UV}(\omega) - I_{UV}}{I_{UV}}, \tag{4.1}$$

at an IR frequency ω, and are for the IR pulse energy corrected.

4.3.2 Computational details

For the calculation of the vibrational spectra we employed the DFT implementation of the Vienna ab initio simulation package (VASP) [31]. The projector augmented wave (PAW) method [32, 33] in combination with the Perdew, Burke, and Ernzerhof (PBE) functional is used [34]. For all cluster sizes we searched for the lowest-energy geometries by using a genetic algorithm (GA) [35] in combination with DFT. The details of the used method can be found in Ref. [36]. In addition, we also considered conformations previously reported in the literature (Nb_3Co, Nb_4Co, Nb_5Co, Nb_6Co, Nb_7Co)[22] and re-optimized the mentioned structures. For some clusters the GA results were equal to those already found in literature,

while for other clusters additional geometries lower in energy were obtained (see Sections 4.3.3-4.3.3 for details). Further, for the PAWs an energy cutoff of 4293 eV is used. All forces were minimized below 10^{-3} eV/Å. In order to eliminate inter-cluster interactions, the clusters were placed in a cubic periodic box with 16 Å dimensions. For the calculations, a single k point (Γ) is used.

4.3.3 Results: Geometric and magnetic structure

In the following, we will present experimental and calculated spectra for the two or three lowest energy isomers. The calculated geometries of the clusters are presented by a stick model, i.e. the clusters are presented by connected sticks. Here green corresponds to Nb and gold to Co. Further, to facilitate the comparison of the experimental and calculated results, the experimental spectra are shown with black squares accompanied by a three-point adjacent average (blue line). The gray dashed line indicates the IR power corrected experimental spectrum. The calculated harmonic vibrational frequencies (vertical sticks) are convoluted with a 15 cm^{-1} FWHM Gaussian line shape function. All frequencies for the structures presented in this work are unscaled and the energies contain the zero-point vibrational energies (ZPVE). Finally, the insets of the figures below show the energy as a function of magnetization for the presented geometries with respect to that of the ground state.

Nb$_3$Co

For Nb$_3$Co a trigonal pyramid is found with three different magnetic states. Here the Nb-Nb and Nb-Co distances differ slightly between the magnetic configurations. In Fig. 4.6 (b)-(d) the corresponding geometries are shown. The magnetic $M = 2\,\mu_B$ (3,1)A geometry is lowest in energy, with (3,1)B and (3,1)C 0.14 eV and 0.25 eV higher respectively. Note that geometry (3,1)A has been reported previously also as the ground state in Ref. [22]. The symmetry point group depends on the magnetization, with C_{3v} for (3,1)A and C_s for (3,1)B and (3,1)C. This difference in symmetry results in significant differences in the vibrational spectra.

Fig. 4.6 shows that the vibrational spectrum of (3,1)A with modes at 224, 228 and 356 cm^{-1} provides the best match to the experimental modes at 212 and 328 cm^{-1} and also explains the doublet structure of the band at 212 cm^{-1}. The vibrational spectra of (3,1)B and (3,1)C contain vibrational modes in the range 125-220 cm^{-1} where no clear experimental modes are observed. Therefore, geometry (3,1)A in the $M = 2\,\mu_B$ state is assigned as the ground state of Nb$_3$Co.

Nb$_4$Co

In the experimental spectrum of Nb$_4$Co presented in Fig. 4.7 (a), at least four modes can be distinguished, at 150, 230, 255 and 325 cm^{-1}. The three geometries lowest in energy are shown in Fig. 4.7(b)-(c). Geometry (4,1)A with $M = 3\,\mu_B$ is
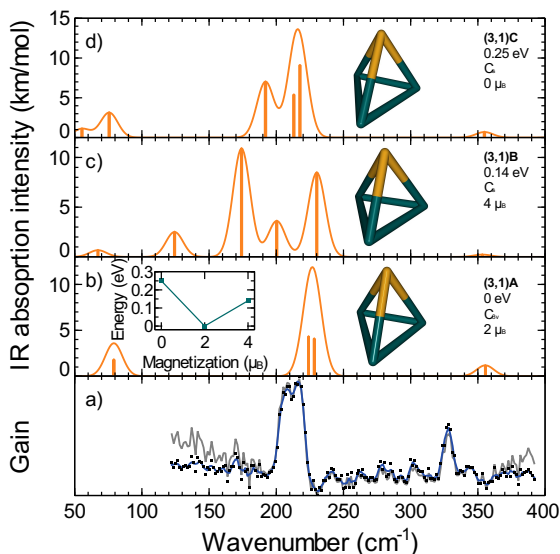
Figure 4.6: Experimental (panel (a), squares) and calculated ((b)-(d)) IR spectra of Nb_3Co. The blue line is a three-point adjacent average of the experimental data. The gray dashed line indicates the IR power corrected spectrum. The calculated discrete vibrational frequencies (orange vertical lines) are convoluted with a $15 \, cm^{-1}$ FWHM Gaussian line shape function (orange). For the geometries green and gold are used for Nb and Co respectively. The inset graph shows the energy as function of the magnetization for the different magnetic states.

the lowest in energy and has C_{3v} point group symmetry. Geometry (4,1)A consists of a trigonal bi-pyramid, where Nb and Co are the axial atoms. In contrast, in geometry (4,1)B the Co atom is part of the equatorial triangle. For geometry (4,1)B the $M = 1 \, \mu_B$ state is the lowest in energy and is 0.18 eV higher compared to the lowest of (4,1)A. Note that both (4,1)A and (4,1)B are previously reported in Ref. [22], where (4,1)A with $M = 3 \, \mu_B$ was also found to be the lowest in energy. The vibrational spectrum of (4,1)A with $M = 3 \, \mu_B$ consists of two large modes at 145 and 238 cm^{-1} and smaller modes at 173, 278 and 342 cm^{-1}, and matches to the experimental spectrum. The vibrational spectrum of (4,1)A with $M = 3 \, \mu_B$ is the only spectrum with two major modes around 150 and 230 cm^{-1}. Therefore, we tentatively assign geometry (4,1)A with $M = 3 \, \mu_B$ to be the ground state of Nb_4Co.

Nb_5Co

In Fig. 4.8 (b)-(d) the three geometries found to be lowest in energy for Nb_5Co are presented. Geometry (5,1)A consists of a dimer-capped rhombus with C_s point
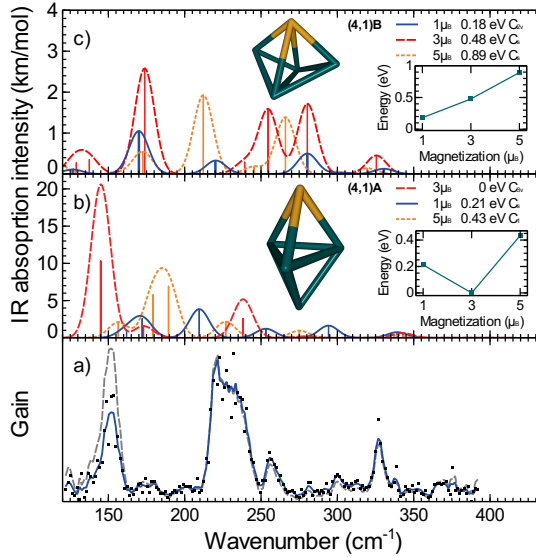
Figure 4.7: Experimental (panel (a)) and calculated ((b)-(c)) vibrational spectra of Nb$_4$Co. The insets show the energy as function of magnetization for each geometry.

group symmetry for all considered magnetic states and has been previously reported in Ref. [22] to be the lowest in energy for the $M = 4$ μ_B state. We also find geometry (5,1)A in the $M = 4$ μ_B state to be the lowest in energy, although the $M = 2$ μ_B state is only 0.03 eV higher. Geometries (5,1)B and (5,1)C both consist of a distorted Nb$_5$ bi-pyramid with one of the faces of the bi-pyramid capped by the Co atom. Geometries (5,1)B and (5,1)C differ in the distance of the Co atom to the bi-pyramid. Whereas for the (5,1)B geometry the $M = 2$ μ_B state is the lowest in energy, the (5,1)C geometry has a non-magnetic ground state which is 0.37 eV higher in energy compared to (5,1)A. The experimental spectrum of Nb$_5$Co in Fig. 4.8 (a) shows three major bands at 170, 205 and 250 cm^{-1}, where the internal structure of the band at 205 cm^{-1} indicates at least a second mode at 220 cm^{-1}. A smaller vibrational mode is present at 275 cm^{-1}. If the calculated spectra of Fig. 4.8 (b)-(d) are compared to that of Fig. 4.8 (a), both (5,1)A $M = 4$ μ_B and (5,1)C $M = 0$ μ_B can only partially explain the experimental spectrum. Whereas (5,1) $M = 4$ μ_B resembles the experimental spectrum below 230 cm^{-1}, the structure around 250 cm^{-1} is not present in the calculated spectrum. Due to the similar vibrational spectrum and the low difference in energy between (5,1)A $M = 2$ μ_B and $M = 4$ μ_B, the former cannot be excluded based on IR vibrational spectroscopy. The vibrational spectrum of (5,1)C $M = 0$ μ_B agrees for the modes above 250 cm^{-1}, but deviates significantly in the relative IR absorption intensities
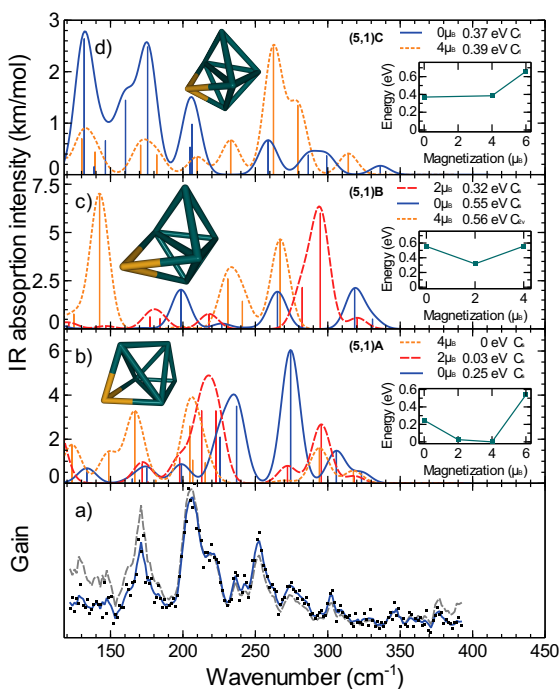
Figure 4.8: Experimental (panel (a)) and calculated ((b)-(d)) vibrational spectra of Nb_5Co.

between modes compared to the experimentally observed gain. Therefore, the IR gain spectrum of Nb_5Co might by due to the geometry (5,1)A with $M = 2$ μ_B or $M = 4$ μ_B, or geometry(5,1)C $M = 0$ μ_B. However, due to the finite temperature at which the experiment is performed, the vibrational spectrum might also be due to a combination of different geometries and magnetic states. On the other hand, the magnetic deflection experiments (see Section 4.2) were performed at a lower temperature than the vibrational experiments and strictly found Nb_5Co to be non-magnetic. Therefore, the (5,1)C geometry corresponding to the $M = 0$ μ_B state is ascribed to be the ground state.

Nb_6Co

The two geometries that were found to be the lowest in energy for Nb_6Co are shown in Fig. 4.9 (b)-(c). Here geometry (6,1)A consists of a distorted pentagon with both sides capped with a single Nb atom. Geometry (6,1)A in the $M = 3$ μ_B state is obtained as the lowest in energy. All magnetic states of the (6,1)A geometry have a C_1 point group symmetry. Geometry (6,1)B consists of two stacked Nb_3 triangles, where the top triangle is capped with a Co atom. For this geometry

81
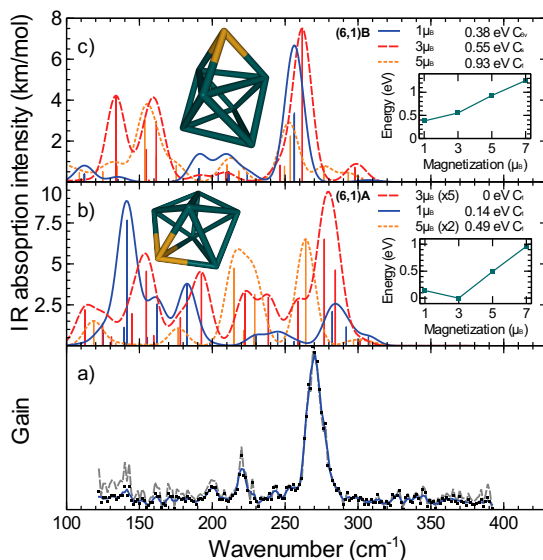
Figure 4.9: Experimental (panel (a)) and calculated ((b)-(c)) vibrational spectra of Nb_6Co. The IR absorption intensity of (6,1)A $M = 3$ μ_B and $M = 5$ μ_B are enhanced by a factor of 5 and 2 respectively to increase visibility.

the $M = 1$ μ_B state is the lowest in energy and has a C_{3v} point group symmetry. The experimental IR spectrum of Nb_6Co is shown in Fig. 4.9(a) and contains a dominant mode at 270 cm^{-1} and two smaller modes at 200 and 220 cm^{-1}. The vibrational spectrum of (6,1)B $M = 1$ μ_B provides the best match to the experimental spectrum with a single dominant mode at 256 cm^{-1} and several smaller modes constituting two bands at 190 and 210 cm^{-1}. In the vibrational spectrum of (6,1)A the bands at 220 and 264 cm^{-1} have similar IR absorption intensities, which is in disagreement with the experimentally observed relative difference between these bands. All other geometries have significant vibrational modes below 190 cm^{-1} where experimentally no modes are observed. Therefore, the (6,1)B geometry with the $M = 1$ μ_B state is assigned to the ground state of Nb_6Co.

Nb_7Co

The experimental spectrum of Nb_7Co in Fig. 4.10a has arguably the poorest signal-to-noise ratio of all spectra shown here. The spectrum shows one clear band centered around 260 cm^{-1}, and some less pronounced structure at lower frequencies. The three geometries lowest in energy are shown in Fig. 4.10b-d. All geometries found have either one symmetry plane or no symmetry at all. Geometry (7,1)A consists of a distorted pentagonal Nb bipyramid, with one of
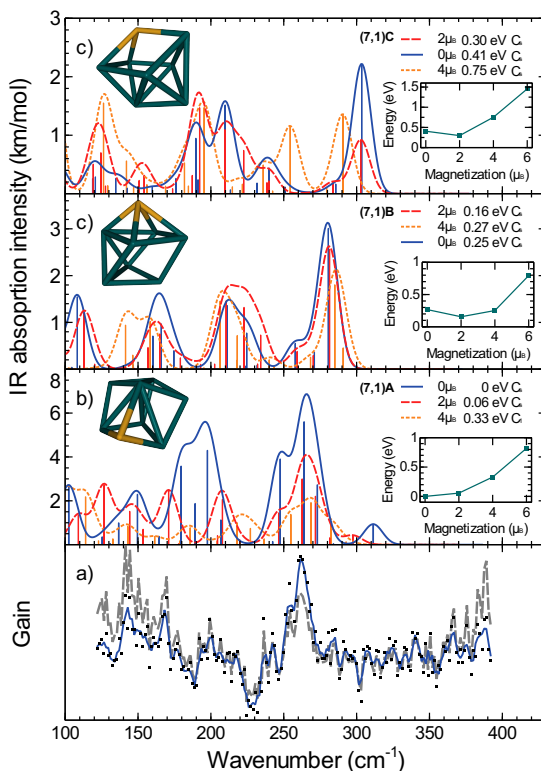
Figure 4.10: Experimental (panel (a)) and calculated ((b)-(d)) vibrational spectra of Nb_7Co.

the faces capped by a Co atom. The lowest energy spin state of geometry (7,1)A has a magnetic moment of $M = 0$ μ_B, although the triplet structure is only 0.06 eV higher in energy. Structure (7,1)A was also previously reported as the lowest in energy [22]. A second structure (7,1)B is formed by a Nb_4Co square pyramid with a Co apex; three more Nb atoms form a triangle parallel to the pyramid base. Structure (7,1)C is essentially the same structure as (7,1)B now with a full Nb pyramid, and the Co part of the triangle. In contrast to structure (7,1)A, the magnetic ground states of geometries (7,1)B and (7,1)C are magnetic, both with $M = 2$ μ_B. Due to the low symmetry of all structures, their vibrational spectra contain many vibrational modes. Structure (7,1)C's spectra all extend to higher frequency than those for either (7,1)A and (7,1)B.

The single experimental band at 260 cm^{-1} can be both explained by (7,1)A $M = 0$ μ_B, and (7,1)B. Both spectra do not match the observed structure in the lower frequency region particularly well. That being so, we cannot assign the spectrum to one particular structure or magnetic state. As will be discussed
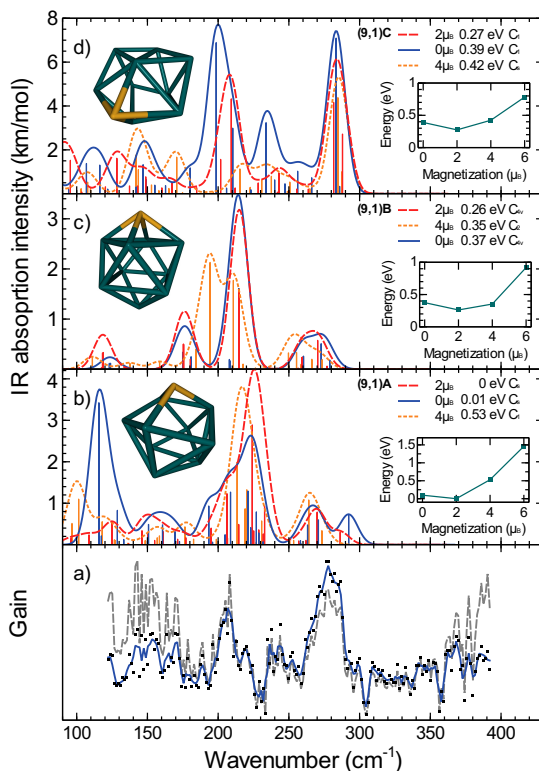
Figure 4.11: Experimental (panel (a)) and calculated ((b)-(d)) vibrational spectra of Nb_9Co.

later, this lack of definite assignment will not change the conclusions regarding the nature of the magnetic structure observed in the Stern-Gerlach deflection experiments.

Nb_9Co

Fig. 4.11 (a) shows the IR gain spectrum of Nb_9Co. Although this figure is not very well resolved, at least bands at 205, 240 and 280 cm^{-1} can be identified. In Fig. 4.11 (b)-(d) the three Nb_9Co geometries that were found to be the lowest in energy are presented. Here geometry (9,1)A consists of a Nb_4 rhombus stacked with a Nb_5 pentagon capped by a Co atom. Note that geometry (9,1)A is distorted such that only a mirror plane symmetry remains. The geometry indicated by (9,1)B consists of two stacked Nb_4 squares, where the two open faces are capped by a Nb and Co atom. The (9,1)C geometry is best described (yet poorly) by a distorted hexagon with a Nb in the center and a Co atom occupying a corner, and capped

by a Nb_3 triangle. Here for the geometry (9,1)C in the states $M = 2$ and $M = 0$ μ_B there is no symmetry, while in the $M = 4$ μ_B state there is only a mirror plane. For geometry (9,1)C the $M = 2$ μ_B state is found to be the lowest in energy, while the $M = 0$ μ_B state is 0.12 eV higher in energy. If the calculated vibrational spectra of Fig. 4.11 (b)-(d) are compared to the experimental spectrum, geometry (9,1)C with $M = 2$ and $M = 0$ provide the best match with dominant bands around 205 and 285 cm^{-1} and an intermediate mode in-between. Therefore, the ground state of the Nb_9Co cluster is described by the (9,1)C geometry.

4.3.4 Comparison with magnetic deflection results

It is interesting to compare the magnetic moments obtained from the magnetic deflection experiments described in Section 4.2 with those obtained above from an inspection of the vibrational spectra. In Table 4.1 the second column contains the total magnetic moments of the Nb_xCo clusters obtained from the best match of the calculated DFT vibrational spectra compared to experiment. For some clusters multiple magnetic moments are given, because of not clear match with experiment. The third column corresponds to the magnetic moments observed in the magnetic deflection experiments (see Fig. 4.5).

For all clusters except for Nb_5Co, it appears that the magnetic moments derived from the magnetic deflection experiments are substantially larger. Part of this difference is due to not taking into account the orbital contribution to the magnetic moment within the DFT calculations [23]. Based on the orbital moment observed in pure Co clusters and Co clusters deposited on Pt(111) a value up to 1 μ_B is roughly expected. This together with the observation made in Ref. [22] that the Nb host contributes about 20-50 % to the total magnet moment of the Nb_xCo clusters, means that the spin contribution is also underestimated within DFT.

Unfortunately, for Nb_5Co and Nb_9Co we cannot be conclusive about the magnetic moment obtained from an inspection of the vibrational spectra. For Nb_5Co the zero magnetic moment would be in agreement with the magnetic deflection experiment, but this state is 0.37 eV higher in energy than the calculated ground state. Note that for Nb_6Co and Nb_7Co the best match of the calculated spectrum with experiment was also for a state higher in energy than the ground state, respectively 0.38 and 0.16 eV. On the other hand for Nb_3Co and Nb_4Co the spectrum calculated for the ground state provided the best match with experiment. For Nb_9Co the state with a magnetic moment of 2 μ_B would be the closest to the result of the magnetic deflection experiment. Here the state with a moment of 2 μ_B is 0.27 eV higher in energy than the ground state.

Table 4.1: Here the second column corresponds to the total magnetic moments of the Nb_xCo clusters obtained from the best match of the calculated DFT vibrational spectra with respect to experiment. The third column contains the magnetic moments obtained from the magnetic deflection experiments presented in Section 4.2.

Cluster	M_{vib} (μ_B)	M_{exp} (μ_B)
Nb_3Co	2	4.1
Nb_4Co	3	5.6
Nb_5Co	0,2,4	0.0
Nb_6Co	1	5.3
Nb_7Co	0	0.0
Nb_9Co	0,2	2.4

4.4 Theoretical investigation based on the Anderson impurity model

The results discussed in this Chapter were performed in a close collaboration and with the help of Lars Peters, who did the computations.

In this section the physical origin is explained of the magnetic behavior obtained from the magnetic deflection experiments presented in Section 4.2. For example, it will be understood why some clusters are strongly magnetic, while others are non-magnetic. For this purpose an analysis based on the Anderson impurity model is performed, where the ground state geometries obtained in Section 4.3 are used as an input.

4.4.1 Theoretical background

There are two possible explanations for the doped Nb_xCo clusters to be non-magnetic. First, they can be non-magnetic, because interactions of the Co atom with the Nb_x host destroy the local moment at the Co site. More precisely, there is a competition between Jahn-Teller distortion working against the formation of a magnetic moment and the exchange interaction between Nb and Co preferring the existence of a magnetic moment. Another possibility is that the local moment at the Co site is screened by the delocalized electrons in the cluster, i.e. the Kondo effect. For both mechanisms it is crucial to understand physically when a local moment is formed on the Co site. In case of a magnetic (transition-metal) impurity resolved in a metallic non-magnetic host this is well established within the celebrated Anderson impurity model [13, 37, 38],

$$H = \sum_{k,\sigma} \epsilon_{k\sigma} c_{k\sigma}^{\dagger} c_{k\sigma}$$
$$+ \sum_{\sigma} E_{d\sigma} d_{\sigma}^{\dagger} d_{\sigma} + U n_{d\uparrow} n_{d\downarrow} \qquad (4.2)$$
$$+ \sum_{k,\sigma} V \left(d_{\sigma}^{\dagger} c_{k\sigma} + c_{k\sigma}^{\dagger} d_{\sigma} \right).$$

Here $E_{d\sigma}$ is the single-particle impurity energy level and U is the onsite Coulomb repulsion between the impurity states. Further, the dispersion of the non-interacting electronic bath is given by $\epsilon_{k\sigma}$. The coupling between the impurity and bath states is described by V. Within this model the formation of a local moment depends on a delicate interplay between the onsite Coulomb interaction, the coupling strength between the impurity and bath states, the position of the bare impurity level (or equivalently the filling) and the positions of the bath energy levels (the dispersion). Within the static mean-field approximation the criterion for a local moment to exist is $U/\Gamma > \pi$. Here $2\Gamma = \pi V^2 \rho(E_F)$ is the effective hybridization, i.e. broadening of the impurity E_d level, where $\rho(E_F)$ is the density of impurity states at the Fermi level. From this criterion it is clear that a large onsite Coulomb interaction and small coupling between the impurity and bath are favorable for a local moment to exist.

It is well known that Kondo physics occurs for the model described by Eq. 4.3 at half-filling and in the limit where the hybridization can be treated perturbatively. More precisely, it can be shown that in this regime the virtual spin-flip scatterings of the bath electrons against the local impurity moment are the dominant processes occurring in the system. At low enough temperatures, below the Kondo temperature, they start to screen the local moment. For half-filling and by treating the hybridization perturbatively, the Kondo temperature T_K can be estimated via

$$T_L = U \left(\frac{\Gamma}{2U} \right)^{1/2} \exp \left[\frac{-\pi |E_d||E_d + U|}{2U\Gamma} \right], \qquad (4.3)$$

where the Kondo temperature is equal to $T_K = 0.041 T_L$ [13]. The Kondo effect for very small systems, in particular ones with discrete energy spectrum, has been been the subject of study already for several decades. Theoretically, the Kondo effect was predicted to be found e.g. in quantum dots [39–41]. A few years later experiments confirmed these predictions [42, 43].

Although less studied within the Anderson impurity model, the situation of a magnetic impurity in a semi-conductor or equivalently a bulk host with a band gap has also been addressed [14, 44]. It has been demonstrated that a local magnetic moment on the impurity is stabilized by the introduction of a band gap. In other words, a local moment can be formed even when the criterion above is not satisfied. Furthermore, the magnitude of the local moment increases with increasing band gap.

In Ref. [14] the investigation of the Anderson impurity model for an impurity in a gapped host is extended to the situation of a finite sized host. Interestingly, it was found that on average the local moment grows with increasing band gap (HOMO-LUMO gap). Here on average should be understood as the local moment averaged over a number of random configurations of the discrete host energy levels for a fixed band gap. Further, it has been shown that in the regimes where $V \ll E_g$ or $V \gg E_g$, the magnitude of the local moment merely depends on the size of the band gap (E_g) and not on the exact positions of the discrete energy levels of the host. Namely, for $V \ll E_g$ the effect of the hybridization is small no matter what the exact arrangement of the host energy levels is, while for $V \gg E_g$ the impurity level hybridizes with all host levels anyway. However, for the regime in between, $V \sim E_g$, the local moment strongly depends on the exact positions of the host energy levels. In Ref. [28] these findings were successfully used to interpret the experimentally observed magnetic moments of Au_xCr clusters. For example, the trend of the Au_x host band gap was found to exactly follow that of the magnetic moment of the Au_xCr clusters.

4.4.2 Computational details

Here we thus performed for the Nb_xCo clusters an analysis based on the Anderson impurity model in the same spirit as in Ref. [28]. For this purpose the density functional theory (DFT) [45, 46] is employed within the full-potential linear muffin-tin orbital method [47]. The local density approximation (LDA) exchange-correlation functional is used in the formulation of Perdew and Wang [48]. For the Nb atoms the main valence basis functions were 4d, 5s and 5p states, while 4s and 4p states were treated as pseudo-core in a second energy set [47]. In case of Co, the 3s and 3p states were treated as pseudo-core, and the 3d, 4s and 4p states as the main valence states. In all calculations the valence states were treated scalar relativistically (without spin-orbit coupling). Since the employed DFT code works in k-space, a supercell approach was used. A large unit cell of at least 14-Å dimensions was used in order to prevent the interaction between clusters of different unit cells. In these calculations the Γ point was the only k-point considered. The geometry of the clusters is obtained from the comparison of the experimental and DFT vibrational spectra performed in Section 4.3. More precisely, the ground state geometries (3,1)A M=3, (4,1)A M=3, (5,1)C M=0, (6,1)B M=1, (7,1)B M=0 and (9,1)B M=2 are taken. Note that for Nb_9Co the structure with C_{4v} symmetry is chosen. Namely for a magnetic cluster the Jahn-Teller distortion should be counteracted by the exchange interaction between Nb and Co.

The effective onsite Coulomb repulsion U between the 3d electrons of the Co impurity is obtained from DFT calculations in conjunction with the random phase approximation (RPA) within the full-potential linearized augmented plane wave (FLAPW) method [49]. All these calculations are performed with the GGA functional as formulated by Perdew, Burke and Ernzerhof [34]. Here a large unit cell of at least 12-Å dimensions is used and also only the Γ point is considered.

Further, the plane wave cutoff is 4.0 Bohr^{-1}. The actual RPA calculations are performed with the SPEX code, which uses the DFT calculations as an input [50]. The SPEX code uses the Wannier90 library to construct the maximally localized Wannier functions [51, 52]. For this construction five 3d states and one 4s state are used for the Co atom.

4.4.3 Results: Anderson impurity model

Table 4.2 presents for each Nb$_x$Co cluster its characteristic parameters related to the Anderson impurity model. The center of gravity of the Co 3d projected density of states E_d and its weighted standard deviation Γ are shown. Also are shown, the band gap (HOMO-LUMO gap) E_g of the bare Nb$_x$ host for the geometry it has in the full Nb$_x$Co cluster and the effective onsite Coulomb interaction U between the Co 3d electrons. Although Eq. 4.3 is strictly speaking only valid for an impurity in a non-magnetic metallic host at half-filling in the limit of small hybridization, we employed it to obtain a rough estimate of the Kondo temperature T_K for the Nb$_x$Co clusters. For convenience also the experimentally observed magnetic moment (see Fig. 4.5) is presented in the last column. As can be observed, the impurity energy level E_d and its broadening 2Γ are more or less constant as a function of cluster size. On the other hand, the band gap of the bare Nb$_x$ host strongly fluctuates as function of cluster size, while the effective onsite Coulomb repulsion slowly decreases as function of cluster size.

Table 4.2: The Co impurity energy level E_d, broadening of the impurity level 2Γ, energy gap E_g (HOMO-LUMO gap) of the bare Nb$_x$ host and the effective onsite Coulomb interaction U between the Co impurity 3d electrons within RPA for different Nb$_x$Co clusters. The sixth column contains a rough estimate of the Kondo temperature T_K obtained from Eq. 4.3. For convenience also the experimentally observed total magnetic moment in μ_B is presented in the last column.

Cluster	E_d (eV)	Γ (eV)	E_g (eV)	U (eV)	T_K (K)	M (μ_B)
T_K (K)	M (μ_B)					
Nb$_3$Co	-0.88	0.34	0.03	5.5	151	4.1
Nb$_4$Co	-0.97	0.35	1.04	5.0	133	5.6
Nb$_5$Co	-1.28	0.35	0.11	4.6	68	0.0
Nb$_6$Co	-1.16	0.34	0.002	4.3	81	5.3
Nb$_7$Co	-0.99	0.26	0.36	4.1	37	0.0
Nb$_9$Co	-1.42	0.33	0.02	3.8	55	2.4

As naively expected from Refs. [14, 28], the magnitude of the local Co moment should follow the trend of the band gap of the isolated host as a function of cluster size. In other words a small band gap is expected for the clusters with zero magnetic moment, while a larger band gap is expected for the magnetic

clusters. It is clear that this expectation is not verified by the results in Table 4.2. For example, magnetic Nb_3Co and Nb_6Co have a very small band gap compared with the non-magnetic Nb_5Co and Nb_7Co clusters.

It is also interesting to have an inspection of the criterion for the existence of a local moment formulated in the Anderson impurity model. In case of an impurity with degenerate orbitals the criterion stated above is slightly modified into $(U+4J)/\Gamma > \pi$, where J is the Hund exchange coupling between the impurity electrons. Even when the contribution of J is neglected, it is clear from Table 4.2 that the criterion is satisfied for all clusters. It was already known from Ref. [28] that a magnetic impurity moment can occur even when the criterion above is not satisfied. However, it appears that the other way around is also possible, i.e. there is no magnetic moment even when the criterion is satisfied.

Only considering the band gap of the bare host did not provide an explanation for some Nb_xCo clusters being magnetic and others non-magnetic. On the other hand for Au_xCr it perfectly predicted the magnetic moment as a function of cluster size. The reason is that the Au_x host is inert, i.e. there is only a weak coupling between the Cr impurity states and Au_x host states. Therefore, Au_x clusters can be considered to be in the regime $V \ll E_g$, where the size of the local moment solely depends on the band gap of the host and not on the exact positions of its energy levels. This is also apparent from the observation that for the Au_xCr clusters the local moment of the Cr impurity is barely reduced by the interactions with the Au_x host. Contrary for the Nb_xCo clusters the magnetic moment strongly fluctuates as a function of cluster size, which hints in the direction that we are in the regime $V \sim E_g$. Unfortunately, this cannot be directly verified from the parameters presented in Table 4.2. Namely, Γ corresponds to the effective hybridization in which both V and the density of states of the host are involved. However, indirectly one could argue that the Nb_xCo clusters are in the $V \sim E_g$ regime. Indeed, from Ref. [14] it is know that for $V \gg E_g$ the impurity moment is almost completely absent, while for $V \ll E_g$ the moment should follow the size of the band gap. Since neither of the two is in agreement with the results of Table 4.2, it is expected that the Nb_xCo clusters are in the $V \sim E_g$ regime.

In the $V \sim E_g$ regime the exact positions of the host energy levels are known to be important. It would be helpful to be a bit more specific and to have a feeling for which host energy levels are important. For example, intuitively one would expect only host states within a range of about V around the Fermi level (chemical potential) to be important.

In order to verify this expectation we investigated the Anderson impurity model for an impurity with a single orbital coupled to 6 spin degenerate bath states. The impurity energy level and onsite Coulomb repulsion were chosen such that the single and double occupied isolated impurity states are symmetric around the chemical potential, e.g. $E_d = -1$ and $U = 3$. Further, a total occupation (impurity plus bath) of 7 electrons was considered. The Anderson impurity model was solved exactly via exact diagonalization. Note that in Ref. [14] a tight binding approximation was employed.

In Table 4.3 the influence of different arrangements of 3 occupied and 3 unoccupied (occupied and unoccupied refers to the bare bath situation) spin degenerate host states on the impurity magnetic moment is presented. For all calculations $V = 0.1$ is taken. The columns 2 to 7 correspond to the positions of the spin degenerate occupied and unoccupied host states, column 8 contains the band gap and the last column the magnetic moment on the impurity. From this table it is clear that indeed only host states within a range of V are important in terms of the magnitude of the impurity magnetic moment. For example, a comparison of the first 5 calculations shows this. Also a comparison of the calculations 3, 8, 9 and 10 clearly indicates this. Another (trivial) observation can be made from calculations 4, 6 and 7. For these calculations the band gap is the same and the only difference is in the positions of the HOMO and LUMO levels with respect to the chemical potential. It appears that these exact positions are unimportant as long as the band gap is fixed. Finally, from calculations 3, 8, 9 and 10 it can also be concluded that not only the band gap itself, but also the number of states (density of states) involved is important.

Table 4.3: The impurity magnetic moment (last column) for different arrangements of the occupied (columns 2 to 4) and unoccupied (columns 5 to 7) spin degenerate host states. The column with E_g contains the band gap (HOMO-LUMO gap).

	E_{occ1}	E_{occ2}	E_{occ3}	E_{unocc1}	E_{unocc2}	E_{unocc3}	E_g	M_{imp}
1	-0.5	-0.5	-0.5	0.5	0.5	0.5	1.0	0.98
2	-0.3	-0.3	-0.3	0.3	0.3	0.3	0.6	0.97
3	-0.1	-0.1	-0.1	0.1	0.1	0.1	0.2	0.78
4	-0.05	-0.05	-0.05	0.05	0.05	0.05	0.1	0.22
5	0	0	0	0	0	0	0	0
6	-0.1	-0.1	-0.1	0	0	0	0.1	0.21
7	0	0	0	0.1	0.1	0.1	0.1	0.23
8	-0.5	-0.1	-0.1	0.1	0.1	0.5	0.2	0.89
9	-0.3	-0.1	-0.1	0.1	0.1	0.3	0.2	0.88
10	-0.2	-0.1	-0.1	0.1	0.1	0.2	0.2	0.86

Since the coupling strength V, the band gap and host density of states are important for the impurity magnetic moment, it would be natural to study the hybridization function corresponding to the Co 3d electrons. Namely, the imaginary part of the hybridization function is proportional to the coupling strength V squared and the host density of states. Furthermore, in the regime $V \sim E_g$ the influence of the coupling of the impurity with the host cannot be considered as a (small) perturbation like in Au_xCr. This coupling is already taken into account explicitly within the hybridization function.

For details on how the hybridization function projected on the Co 3d states

is obtained, the reader is referred to Ref. [53]. In short, the Nb_xCo cluster is first calculated self-consistently within DFT. Then, from the obtained Kohn-Sham eigenstates and energies, the corresponding Green's function is constructed. Next, this Green's function is projected on the 3d states. This projected Green's function $G_{mm'}(E)$ and the hybridization function of the Co 3d states $\Delta_{mm'}(E)$ are related by

$$G_{mm'}(E) = \left[E - \epsilon_{mm'} + \mu - \Delta_{mm'}(\omega) \right],$$

$$\text{with } \Delta_{mm'}(E) = \sum_k \frac{V_{km}^* V_{km'}}{E - \epsilon_k + \mu}. \tag{4.4}$$

Here, E is the energy, V_{km} represent the coupling strength of the impurity state m with bath (host) state k, $\epsilon_{mm'}$ is obtained from the local projection of the DFT Kohn-Sham Hamiltonian and ϵ_k corresponds to the energies of the bath states. From the expression of the hybridization function in terms of the coupling strengths and bath energy levels, it is clear that different choices of them can lead to the same hybridization function and thus Anderson impurity problem. Therefore, unless the V_{km} matrix elements are computed directly, it is hard to explicitly determine whether Nb_xCo corresponds to the $V \sim E_g$ regime. However, this determination is not necessary to understand the physical origin of the presence or absence of magnetism in the Nb_xCo clusters. From the discussions above we know that the HOMO-LUMO gap, the density of states at the HOMO and LUMO levels, the coupling V between the impurity and host states, and the onsite Coulomb repulsion U are important for the impurity magnetic moment. The first three are captured by the (imaginary part of the) hybridization function. Therefore, in Fig. 4.12 the imaginary part of the total (trace of $\Delta_{mm'}(E)$) hybridization function for the Co 3d states is shown for the different Nb_xCo clusters. From this figure an estimate can be made of the coupling strength V. Assuming that the peak of Nb_3Co at -0.25 eV is due to the coupling with only one bath state, would require a V of about 0.37 eV. Therefore, the hybridization function is only plotted roughly in this range around the chemical potential (zero energy).

From the discussions above we know that the HOMO-LUMO gap, the density of states at the HOMO and LUMO levels, the coupling V between the impurity and host states, and the onsite Coulomb repulsion U are important for the impurity magnetic moment. The first three are captured by the (imaginary part of the) hybridization function. Therefore, in Fig. 4.12 the imaginary part of the total (trace of $\Delta_{mm'}(E)$) hybridization function for the Co 3d states is shown for the different Nb_xCo clusters. From this figure an estimate can be made of the coupling strength V. Assuming that the peak of Nb_3Co at -0.25 eV is due to the coupling with only one bath state, would require a V of about 0.37 eV. Therefore, the hybridization function is only plotted roughly in this range around the chemical potential (zero energy).

From the model calculations presented in Table 4.3 it is expected that a small HOMO-LUMO gap and large hybridization around the HOMO and LUMO levels
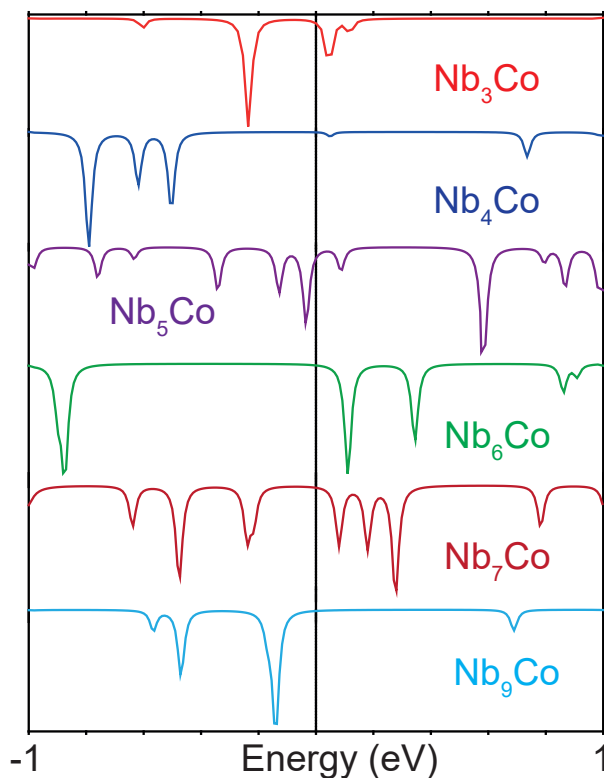
Figure 4.12: The imaginary part of the hybridization function for the Co 3d electrons for the different Nb_xCo clusters.

is unfavourable for a magnetic moment. A discussion solely based on the hybridization functions of Fig. 4.12 is complicated by the fact that the onsite Coulomb repulsion is not constant over the range of clusters investigated. However, for two clusters differing only by one Nb atom in size the difference in the onsite Coulomb interaction is small. Therefore, in the following the hybridization functions will be compared cluster for cluster. From Fig. 4.12 it appears that Nb_3Co has a much stronger hybridization around the chemical potential (zero energy) than Nb_4Co. More precisely for Nb_3Co there is a peak at about -0.25 eV and 0.1 eV, while Nb_4Co has a peak at about -0.5 eV and a very tiny one at 0.05 eV. Since the gap between the peaks is larger and the total height of the peaks is smaller for Nb_4Co, a larger magnetic moment is expected for Nb_4Co compared to Nb_3Co. This is confirmed by the magnetic deflection experiment (see last column of Table 4.2 and Fig. 4.5).

By going from magnetic Nb_4Co to non-magnetic Nb_5Co, it is clear that there

is a huge increase of hybridization around the chemical potential. Therefore, in addition with a smaller onsite Coulomb interaction it is indeed expected that Nb_5Co has a much smaller tendency to be magnetic than Nb_4Co (and Nb_3Co). Then, by going from non-magnetic Nb_5Co to magnetic Nb_6Co, there is a considerable decrease of hybridization around the chemical potential. More precisely, there is a large increase from about 0.15 eV to 1.0 eV in the separation between the first peak below and above the chemical potential. Thus, in accordance with experiment Nb_6Co is expected to have a larger tendency to be magnetic than Nb_5Co. Next, magnetic Nb_6Co and non-magnetic Nb_7Co will be compared. As expected the hybridization around the chemical potential is larger for Nb_7Co than for Nb_6Co. Interestingly, Nb_7Co has a similar hybridization around the chemical potential as Nb_3Co. However, Nb_3Co has an onsite Coulomb interaction which is 1.4 eV larger than for Nb_7Co. Finally, we compare the non-magnetic Nb_7Co with magnetic Nb_9Co. Although Nb_9Co has a quite large peak at about -0.15 eV, the difference between the first peak below and above the chemical potential is much larger. Therefore, the effective hybridization around the chemical potential is as expected smaller for Nb_9Co than for Nb_7Co. To conclude, for Nb_3Co to Nb_7Co and Nb_9Co the effective hybridization around the chemical potential is in agreement with the experimentally observed magnetic behavior.

Above we performed an analysis based on the Anderson impurity model in order to explain the experimentally observed magnetic behavior. From an inspection of the hybridization function and the onsite Coulomb repulsion a trend in agreement with experiment could be predicted. However, based on these observations it cannot be explained whether the local Co moment is truly absent or Kondo screened. Therefore, we made an estimate of the Kondo temperature for the clusters from Eq. 4.3, which are presented in the sixth column of Table 4.2 above. In case the absence of magnetic moment is due to a complete Kondo screening, higher Kondo temperatures are expected for the non-magnetic clusters than for the magnetic ones. From Table 4.2 it can be observed that the results are not in accordance with this expectation. For example, the highest Kondo temperatures are observed for magnetic Nb_3Co and Nb_4Co. Further, non-magnetic Nb_5Co and Nb_7Co have a smaller Kondo temperature than magnetic Nb_6Co.

In addition we searched for signatures of the Kondo effect in the Nb_xCo clusters from the experimental side. For this purpose the temperature dependence of the magnetic deflection experiments was investigated. In case of the Kondo effect it is expected that by approaching the Kondo temperature from below the screening of the local Co moment reduces. An inspection of Table 4.2 shows that Nb_5Co has a Kondo temperature of 68 K and Nb_7Co of 37 K. However, even for temperatures up to 70 K both clusters still appeared to be strictly non-magnetic. These results indeed indicate that the Kondo effect is not responsible for the absence of magnetism in Nb_5Co and Nb_7Co.

4.4.4 Nb$_n$Co clusters summary

We have thus performed magnetic deflection experiments on Co doped Nb clusters from which we made the interesting observation that some clusters are strongly magnetic, while others are non-magnetic. Further, it appeared that the magnetic behavior of the clusters could be divided into two regimes. For Nb$_x$Co clusters with x≥14, the magnetic to non-magnetic behavior is exactly determined by having an odd or even number of atoms in the cluster, i.e. having an unpaired electron or not. Note that this behavior was also observed for pure Nb clusters. Then, in the region x<14 strong fluctuations in the magnetic moment as function of cluster size are observed.

There are in principle two possible explanations for some clusters being non-magnetic. Either the local moment at the Co site is absent or it is screened by the delocalized electrons of the cluster, i.e. the Kondo effect. In order to reveal the physical origin, we conducted a combined theoretical and experimental investigation.

First, we made a comparison of the experimental vibrational spectra with those obtained from a DFT study. This served two purposes. It provides the ground state geometry of the clusters. Further, due to the dependence of the vibrational spectrum on the magnetic moment, the performance of DFT in predicting the magnetic moments can be investigated. We found that not for all clusters it could be determined which calculated vibrational spectrum has the best agreement with experiment. However, for those it could, two interesting observations could be made. The best match with experiment not always corresponds to the geometry and magnetic state found to be the lowest in energy, ground state, in DFT. Further, we found that the DFT magnetic moments were considerably smaller than those obtained from the magnetic deflection experiments. This is due to a neglect of the orbital moments in our DFT calculations and underestimation of the spin moments within DFT.

Second, using the obtained ground state structures as an input, we performed an analyses based on the Anderson impurity model. It appears that the non-magnetic clusters are due the absence of the local Co moment and not due to the Kondo effect. In addition, the magnetic behavior of the Nb$_x$Co clusters can be understood from an inspection of their electronic structure. Here magnetism is favored when the effective hybridization around the chemical potential is small, while the absence of magnetism is signalled by a large effective hybridization around the chemical potential.

Thus, DFT cannot provide a quantitative description of the magnetic moments in agreement with the deflection experiments. However, DFT can be employed to obtain a qualitative understanding of the experimentally observed magnetic moments by using its results as an input for an analyses based on the Anderson impurity model. In order to also obtain theoretically a quantitative agreement with experiment we argue that a proper consideration of correlation effects is required. For example, for DFT in combination with the dynamical mean-field

theory it has recently been demonstrated to give orbital and spin magnetic moments in good agreement with experiment for pure Co clusters [23].

4.5 Co doped V clusters: Magnetic moments.

As it was shown in chapter 3 above, the magnetic properties of pure V and Nb clusters are similar. It is therefore interesting to investigate how the magnetic properties of the Co doped V clusters evolve compared to the Nb host case. In order to create Co doped V clusters a rod consisting in $V_{1-y}Co_y$ (y = 5 %) was used. The deflections took place at the same conditions as for Co doped Nb clusters. The results are shown in Fig. 4.13. Again we can find three different types of behavior. These are, first, superparamagnetic clusters, such as V_3Co, V_7Co, $V_{11}Co$, $V_{21}Co$ and $V_{25}Co$. Second, several clusters show double-sided deflection profiles, such as V_4Co and the majority of odd-numbered clusters. And last, also completely non-magnetic clusters, where V_5Co is the smallest one.

In Fig. 4.14 the evolution of the magnetic moment as a function of size is shown. It can be seen that similarly as it happens for Nb as a host material, the magnetic moment of Co atom is decreased. This effect is even stronger than it is for Nb, as V as host does not allow any single cluster to achieve 6 μ_B, the maximum is 3 μ_B. There are also less clusters which behave superparamagnetically. It is interesting to note than for all the odd-numbered clusters, regardless of their sizes, the magnetic behavior is due only to a single unpaired spin, no superparamagnetic behavior could be found for any size at all. In contrast, pure V_{13}, V_{15} and V_{33} clusters show larger magnetic moments and a single-sided deflection. Thus, when exchanging one V atom for a Co one, the large atomic magnetic moment of Co is lost. In contrast, even-numbered cluster sizes that showed larger moments in case of pure V, retain their superparamagnetic behavior when exchanging one V atom for a Co atom. Namely, $V_{21}Co$, $V_{25}Co$ and $V_{27}Co$ keep the magnetic moment measured for V_{22}, V_{26} and V_{28} in the previous chapter.

All measurements for both Co doped Nb and V were performed at 2 bar, which may give raise to somewhat incomplete thermalization and thus the peak at 0 μ_B in the case of single uncoupled spin behavior. Interestingly, this effect is stronger for clusters doped with Co, as compared to the pure ones, for both Nb and V cases.

4.5.1 V_nCo clusters summary

Similar to Nb, V clusters also destroy the magnetic moment of Co atom. This effect is even stronger here than it was in the case of Nb as host. We did not carry out any theoretical calculation that proves the origin for this, but it may be understood in the same manner as for the Nb host, as these are similar systems.
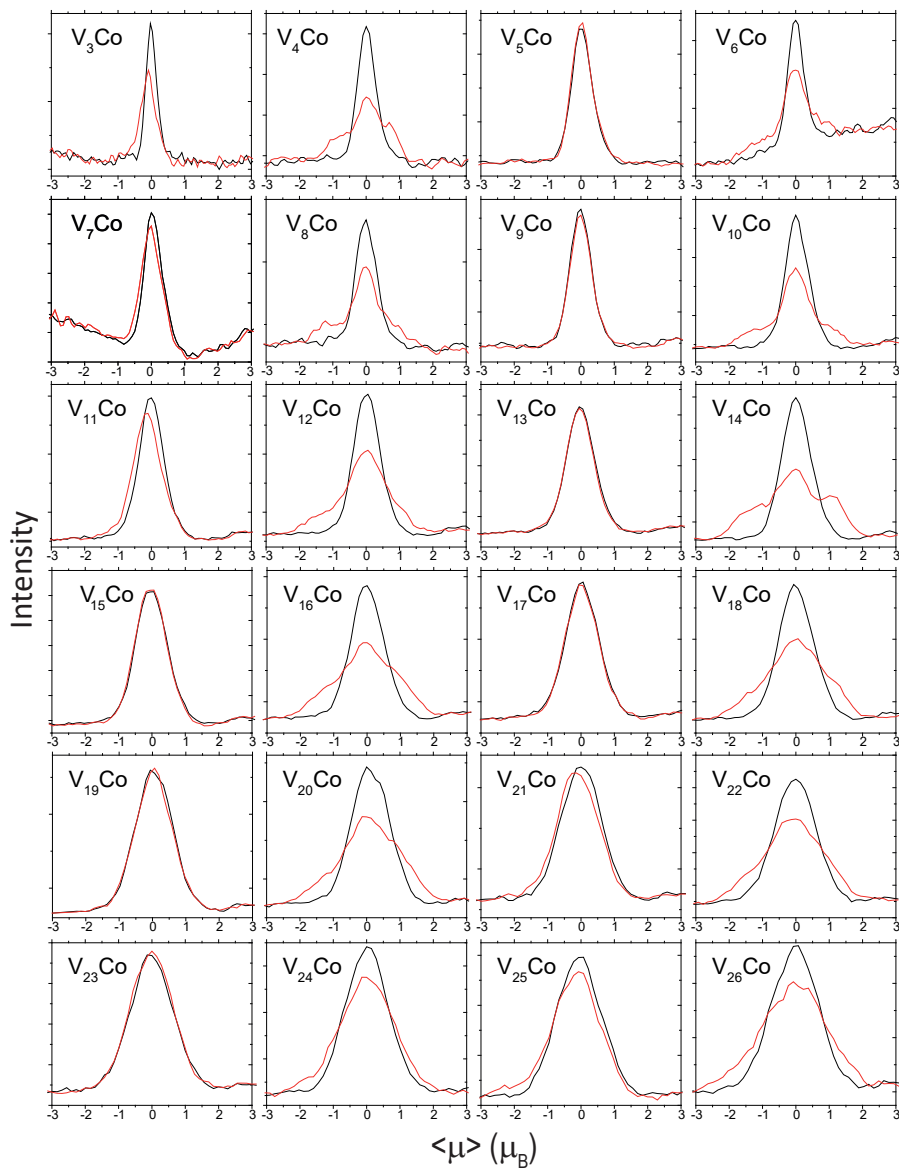
Figure 4.13: Magnetic deflections of Co doped V clusters. The deflections were measured at a temperature of 25 K and at a gas carrier pressure of 2 bar. Black line corresponds to zero magnetic field, red line to the field of 2.4 T.
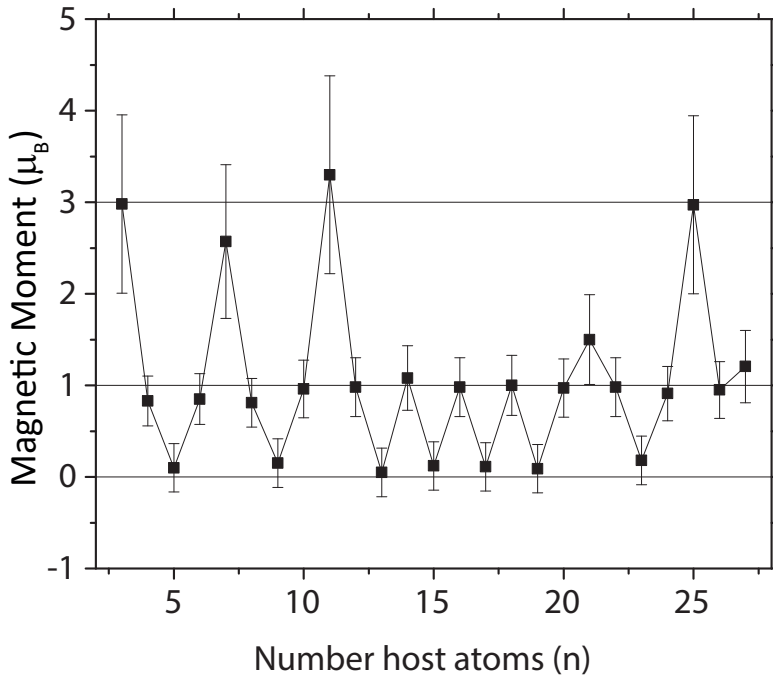
Figure 4.14: Magnetic moments of Co doped V clusters.

4.6 Conclusions

After thus proving that Co cannot induce net magnetic moment on Nb or V as host and that its magnetic moment is strongly decreased, we can conclude that the magnetic moments of a 3d impurity should generally decrease when doping other 3d/4d non-magnetic metals. This is explained by a strong hybridization of the impurity electrons with those of the host. The next step is therefore to verify the behavior of an impurity of a different kind, for example the one with 4f electrons. Such impurity would have much more localized electrons responsible for its magnetic moment, and thus may retain its properties better or even induce magnetic moments on these hosts. Such study will be presented in the next chapter.

References

[1] E. Dagotto, "Correlated electrons in high-temperature superconductors Elbio," Rev. Mod. Phys. **66**, 763-840 (1994).

[2] J. M. Tranquada, B. J. Sternlieb, J. D. Axe, Y. Nakamura, and S. Uchida, "Evidence for stripe correlations of spins and holes in copper oxide superconductors," Nature. **375**, 561-563 (1995).

[3] K. Yamada, C. H. Lee, K. Kurahashi, J. Wada, S. Wakimoto, S. Ueki, H. Kimura, Y. Endoh, S. Hosoya, G. Shirane, R. J. Birgenau, M. Greven, M. A. Kastner, and Y. J. Kim, "Doping dependence of the spatially modulated dynamical spin correlations and the superconducting-transition temperature in $La_{2-x}Sr_xCuO_4$," Phys. Rev. B. **57**, 6165-6172 (1998).

[4] J. Fontcuberta, B. Martínez, A. Seffar, S. Piñol, J. L. García-Muñoz, and X. Obradors, "Colossal Magnetoresistance of Ferromagnetic Manganites: Structural Tuning and Mechanisms," Phys. Rev. Lett. **76**, 1122-1125 (1996).

[5] A. Zylbersztejn and N. F. Mott, "Metal-insulator transition in vanadium dioxide," Phys. Rev. B. **11**, 4383-4395 (1975).

[6] M. I. Katsnelson, V. Yu. Irkhin, L. Chioncel, A. I. Lichtenstein, and R. A. de Groot, "Half-metallic ferromagnets: From band structure to many-body effects,"Rev. Mod. Phys. **80**, 315-378 (2008).

[7] R. Willett, J. P. Eisenstein, H. L. Störmer, D. C. Tsui, A. C. Gossard, and J. H. English, "Observation of an Even-Denominator Quantum Number in the Fractional Quantum Hall Effect," Phys. Rev. Lett. **59**, 1776-1779 (1987).

[8] R. G. R. Stewart, "Heavy-fermion systems," Rev. Mod. Phys. **56**, 755-787 (1984).

[9] A. W. Castleman and S. N. Khanna, "Clusters, Superatoms, and Building Blocks of New Materials," J. Phys. Chem. **113**, 2664 (2009).

[10] M. König, S. Wiedmann, C. Brüne, A. Roth, H. Buhmann, L. W. Molenkamp, X.-L. Qi, and S.-C. Zhang, "Quantum Spin Hall Insulator State in HgTe Quantum Wells," Science. **318**, 766-770 (2007).

[11] X. Michalet, F. F. Pinaud, L. A. Bentolila, J. M. Tsay, S. Doose, J. J. Li, G. Sundaresan, A. M. Wu, S. S. Gambhir, and S. Weiss, "Quantum Dots for Live Cells, in Vivo Imaging, and Diagnostics," Science. **307**, 538-544 (2005).

[12] J. Friedel, "The distribution of electrons round impurities in monovalent metals," Phil. Mag. **43**, 153 (1952).

[13] A. C. Hewson, *The Kondo Problem to Heavy Fermions*, edited by D. Edwards and D. Melville (Cambridge University Press, Cambridge, 1993).

[14] K. Hirsch, J. T. Lau, and B. v. Issendorff, "Extension of the Anderson impurity model for finite systems: Band gap control of magnetic moments," arXiv. **1407.2018**, (2014).

[15] K. Hirsch, V. Zamudio-Bayer, A. Langenberg, M. Niemeyer, B. Langbehn, T. Möller, A. Terasaki, B. v. Issendorff, and J. T. Lau, "Magnetic Moments of Chromium-Doped Gold Clusters: The Anderson Impurity Model in Finite Systems," Phys. Rev. Lett. **114**, 087202 (2015).

[16] L. Peters, E. Şaşıoğlu, S. Rossen, C. Friedrich, S. Blügel, and M. I. Katsnelson, "Nonconventional screening of the Coulomb interaction in Fe_xO_y clusters: An ab initio study," Phys. Rev. B. **95**, 155119 (2017).

[17] R. Moro, X. Xu, S. Yin, and W. A. de Heer, "Ferroelectricity in Free Niobium Clusters," Science. **300**, 1265-1269 (2003).

[18] R. Moro, S. Yin, X. Xu, and W. A. de Heer, "Spin Uncoupling in Free Nb Clusters: Support for Nascent Superconductivity," Phys. Rev. Lett. **93**, 086803 (2004).

[19] A. Diaz-Bachs, M. I. Katsnelson, and A. Kirilyuk, "Kramers degeneracy and relaxation in vanadium, niobium and tantalum clusters," New J. Phys. **20**, 043042 (2018).

[20] A. Fielicke, C. Ratsch, G. von Helden, and G. Meijer, "The far-infrared spectra of neutral and cationic niobium clusters: $Nb_5^{0/+}$ to $Nb_9^{0/+}$," J. Chem. Phys. **127**, 234306 (2007).

[21] A. Pramann, K. Koyasu, A. Nakajima, and K. Kaya, "Band gap shiftings in Co-doped Nb_n (n = 3-15) clusters: Influence of Co 3d electrons on the electronic structure," Int. J. Mass Spectrom. **229**, 77-82 (2003).

[22] H. Li, X. Kuang, L. Ding, P. Shao, L. Han, and T. Lu, "Evolution of geometrical structures, stabilities and electronic properties of neutral and anionic $Nbn_{n-1}Co$ (n = 2-9) clusters: Comparison with pure niobium clusters," Int. Comput. Mater. Sci. **95**, 600-609 (2014).

[23] L. Peters, I. Di Marco, O. Grånäs, E. Şaşıoğlu, A. Altun, S. Rossen, C. Friedrich, S. Blügel, M. I. Katsnelson, and A. Kirilyuk and O. Eriksson, "Correlation effects and orbital magnetism of Co clusters," Phys. Rev. B. **93**, 224428 (2016).

[24] A. Langenberg, K. Hirsch, A. Lawicki, V. Zamudio-Bayer, M. Niemeyer, P. Chmiela, B. Langbehn, A. Terasaki, b. v. Issendorff, and J. T. Lau, "Spin and orbital magnetic moments of size-selected iron, cobalt, and nickel clusters and their link to the bulk phase diagrams," Phys. Rev. B **90**, 184420 (2014).

[25] J. Minár, S. Bornemann, O. Šipr, S. Polesya, and H. Ebert, "Magnetic properties of Co clusters deposited on Pt(111)," Appl. Phys. A **82**, 139 (2006).

[26] I. M. L. Billas, A Châtelain, and W. A. de Heer, "Magnetism of Fe, Co and Ni clusters in molecular beams," J. Magn. Mat. **168**, 64 (1997).

[27] Q. Ma, Z. Xie, J. Wang, Y. Liu, and Y. Li, "Structures, stabilities and magnetic properties of small Co clusters," Phys. Lett. A **358**, 289 (2006).

[28] J. M. Bakker, V. J. F. Lapoutre, B. Redlich, J. Oomens, B. G. Sartakov, A. Fielicke, G. von Helden, G. Meijer, and A. F. G. van der Meer, "Intensity-resolved IR multiple photon ionization and fragmentation of C_{60}," J. Chem. Phys. **132**, 074305 (2010).

[29] M. Haertelt, V. J. F. Lapoutre, J. M. Bakker, B. Redlich, D. J. Harding, A. Fielicke, and G. Meijer, "Structure Determination of Anionic Metal Clusters via Infrared Resonance Enhanced Multiple Photon Electron Detachment Spectroscopy," J. Phys. Chem. Lett. **2**, 1720 (2011).

[30] J. Jalink, J. M. Bakker, Th. Rasing, and A. Kirilyuk, "Channeling Vibrational Energy To Probe the Electronic Density of States in Metal Clusters," J. Phys. Chem. Lett. **6**, 750-754 (2015).

[31] G. Kresse and F. Furthmüller, "Efficient iterative schemes for ab initio total-energy calculations using a plane-wave basis set," Phys. Rev. B. **54**, 11169-11186 (1996).

[32] P. E. Blöchl, "Projector augmented-wave method," Phys. Rev. B. **50**, 17953-17979 (1994).

[33] G. Kresse and D. Joubert, "From ultrasoft pseudopotentials to the projector augmented-wave method," Phys. Rev. B. **59**, 1758 (1999).

[34] J. P. Perdew, K. Burke, and M. Ernzerhof, "Generalized Gradient Approximation Made Simple," Phys. Rev. Lett. **77**, 3865-3868 (1996).

[35] R. L. Johnston, "Evolving better nanoparticles: Genetic algorithms for optimising cluster geometries," Dalt. Trans. **2003**, 4193-4207 (2003).

[36] R. Logemann, G. A. de Wijs, M. I. Katsnelson, and A. Kirilyuk, "Geometric, electronic, and magnetic structure of $Fe_xO_y^+$ clusters," Phys. Rev. B. **92**, 144427 (2015).

[37] P. W. Anderson, "Localized magnetic states in metals," Phys. Rev. **124**, 41 (1961).

[38] A. M. Tsvelick and P. B. Wiegmann, "Exact results in the theory of magnetic alloys," Adv. Phys. **32**, 453 (1983).

[39] T. K. Ng and P. A. Lee, "On-Site Coulomb Repulsion and Resonant Tunneling," Phys. Rev. Lett. **61**, 1768-1771 (1988).

[40] Y. Meir, N. S. Wingreen, and P. A. Lee, "Low-temperature transport through a quantum dot: The Anderson model out of equilibrium," Phys. Rev. Lett. **70**, 2601-2604 (1993).

[41] N. S. Wingreen and Y. Meir, "Anderson model out of equilibrium: Noncrossing-approximation approach to transport through a quantum dot," Phys. Rev. B. **49**, 11040-11052 (1994).

[42] S. M. Cronenwett, T. H. Oosterkamp, and L. P. Kouwenhoven, "A tunable Kondo effect in quantum dots," Science. **280**, 540-544 (1998).

[43] D. Goldhaber-Gordon, H. Shtrikman, D. Abusch-Magder, D. Mahalu, U. Meirav, and M. A. Kastner, "Kondo effect in a single-electron transistor," Nature. **391**, 156-158 (1998).

[44] F. D. M. Haldane and P. W. Anderson, "Simple model of multiple charge states of transition-metal impurities in semiconductors," Phys. Rev. B. **13**, 2553 (1976).

[45] P. Hohenberg and W. Kohn, "Inhomogeneous Electron Gas," Phys. Rev. **136**, B 864-B 871 (1964).

[46] W. Kohn and L. J. Sham, "Self-Consistent Equations Including Exchange and Correlation Effects," Phys. Rev. **140**, A 1133-A 1138 (1965).

[47] J. M. Wills, M. Alouani, P. Andersson, A. Delin, O. Eriksson, and O. Grechnyev, Springer-Verlag, Berlin (2010).

[48] J. P. Perdew and Y. Wang, "Accurate and simple analytic representation of the electron-gas correlation energy," Phys. Rev. B. **45**, 13244 (1992).

[49] www.lapw.de.

[50] C. Friedrich, S. Blügel, and A. Schindlmayr, "Efficient implementation of the GW approximation within the all-electron FLAPW method," Phys. Rev. B. **81**, 125102 (2010).

[51] A. A. Mostofi, J. R. Yates, Y. -S. Lee, I. Souza, D. Vanderbilt, and N. Marzari, "wannier90: A tool for obtaining maximally-localised Wannier functions," Comput. Phys. Commun. **178**, 685-699 (2008).

[52] F. Freimuth, Y. Mokrousov, D. Wortmann, S. Heinze, and S. Blügel, "Maximally localized Wannier functions within the FLAPW formalism," Phys. Rev. B. **78**, 035120 (2008).

[53] O. Grånäs, I. Di Marco, P. Thunström, L. Nordström, O. Eriksson, T. Björkman, and J.M. Wills, "Charge self-consistent dynamical mean-field theory based on the full-potential linear muffin-tin orbital method: Methodology and applications," Comp. Mat. Sci. **55**, 295-302 (2012).

5 Magnetic properties of Tb doped Nb and V clusters

In the previous chapter 4 we studied the magnetic properties of Co doped V and Nb. It appeared clear that the effect of Co impurity is not to induce magnetic moments in the hosts; on the contrary, the magnetic moment of Co itself is often quenched. In this chapter Tb doped V and Nb clusters are studied. Tb is chosen as representative among rare earth metals, because of its large magnetic moment, 10 μ_B in the atomic case, which becomes 9 μ_B in compounds. Again the clusters will be studied by means of the Stern-Gerlach setup described in chapter 2. The results of the magnetic deflection experiments in this case show a drastically different behavior from that of Co. All of the clusters were magnetic, with the measured magnetic moments larger than Tb magnetic moment by itself. This proves that Tb can induce sizable spin polarization in the host, with the total measured magnetic moments going up to 22 μ_B.

5.1   Introduction

Rare earth metals are known for their magnetic properties. The 4f electrons of rare earth metals, because of the small radius of the 4f shell, keep their atomic-like spin- and orbital moments also in the bulk phase. As representative of rare earth metals we selected Tb that also shows strong magnetic properties in clusters [1, 2]. Here we study the effects of Tb doping on the magnetic properties of V and Nb hosts. Atomic terbium has the magnetic moment of 10 μ_B, but in the bulk Tb is trivalent and thus looses one of its 4f electrons. The magnetic moment then becomes 9 μ_B, not counting a small contribution from outer electronic shells [3].

In the bulk, Tb is found to have a Néel temperature of 237 K being antiferromagnetically ordered for temperatures between 218 and 237 K, but becomes ferromagnetic below 218 K [4]. For single crystals it was found to have a saturation magnetic moment of 9.34 μ_B/atom [5].

Because of this large moment, Tb attracted a lot of attention. For example, molecular magnets containing Tb are less perturbed by the environment, making them more stable [6]. Interestingly, the magnetic properties of isolated $TbPc_2$ molecules supported on a Cu(100) show that the saturation orbital and spin magnetic moment values reach 3 and 6 μ_B [7]. The same single molecule coupled to single-walled carbon nanotube contacted with non-magnetic electrodes, results in magneto-resistance ratios up to 300% at temperatures less than 1 K, demonstrating the functionality of a supramolecular spin valve without magnetic leads [8]. Tb can give rise to very large single-ion magnetic anisotropies for 4f ions, and thus increases the stability against thermal fluctuations by an order of magnitude [9].

The goal of this chapter will be to study whether Tb can keep its magnetic moment similarly to what happens to the previously mentioned single molecule magnets when interacting with V and Nb hosts. And if so, whether it is also capable to induce spin polarization in both hosts.

5.2   Magnetic deflections of Tb-doped V clusters

The magnetic deflection experiments were carried out similarly as was done in the previous chapters. In order to create Tb-doped V clusters a rod consisting of $V_{1-y}Tb_y$ (y=5%) was used. The deflections at a temperature of 25 K using a helium pressure of 6 bar are shown in Fig. 5.1. The magnetic field used was only 0.25 T as a larger field resulted in a strong loss of signal, immediately indicating large magnetic moments. The velocity of the clusters for this measurement was 475 m/s.

All clusters shown in Fig. 5.1 deflect towards the direction of the strongest magnetic field. The effect is more pronounced for the smallest clusters. It is interesting to note that, at least among the smaller sizes, there is no single cluster which does not deflect. Thus, in contrast to what happens for Co as magnetic impurity, for Tb atom V as host does not destroy its magnetic moment. Moreover,

Figure 5.1: Magnetic deflections of V_nTb clusters at 25 K. Black line for no magnetic field, red line for 0.25 T. The He pressure was 6 bar.

Tb also induces some polarization on the host, as the obtained magnetic moments are always larger than 9 μ_B, as can be seen in Fig. 5.2. For instance, for the smallest cluster studied, V_3Tb, the measured magnetic moment is about 16 μ_B, and the maximum spin magnetic moment available for V_3 is 9 μ_B, as V_3 has 9 3d electrons available which may contribute to the magnetic moment, so at least a part of it must come from the host. In general, the measured magnetic moments lie between 9 and 25 μ_B within the error bars.

We have also measured the behavior of these clusters with larger magnetic fields, in order to see better the deflections for clusters with large masses. On the
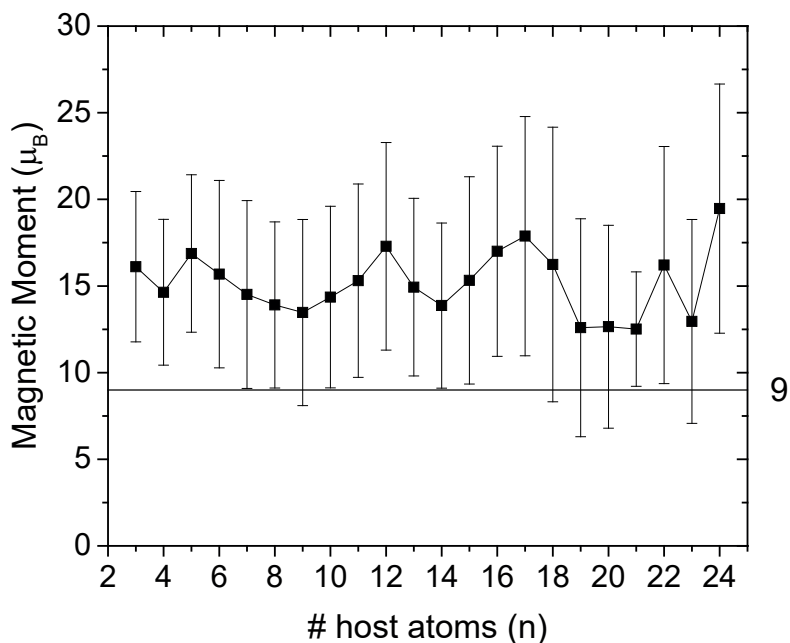
Figure 5.2: Magnetic moments of V_nTb clusters as function of size.

other hand, due to the relatively large magnetic gradient, using a large magnetic field creates a loss in signal for the smallest clusters. As Fig. 5.3 shows, deflections are larger than those for Fig. 5.1.

Additionally to the loss in signal for large magnetic fields, there is another issue, which makes this measurement difficult, which is the mass. Tb mass is 158.93 atomic units of mass, while V mass is 50.94 atomic units of mass. Thus Tb mass is 3 times the mass of V, plus 6.11 a.u. For this reason the distance between the peaks of pure V clusters and the Tb doped ones is small. This issue is of importance for the largest clusters, as the peaks of such clusters are broader. Because of this, when the deflections for the doped clusters are large, they overlap with neighbor peak corresponding to a pure V cluster, making the analysis impossible. Also for this reason, it is important to choose the right magnetic field. It can be seen in Fig. 5.4 how the deflections of neighbor peaks overlap for a magnetic field of 1 T.

Figure 5.3: Magnetic deflections of V$_n$Tb clusters at 25 K. Black line for no magnetic field, red line for 0.5 T. The He pressure was 6 bar.
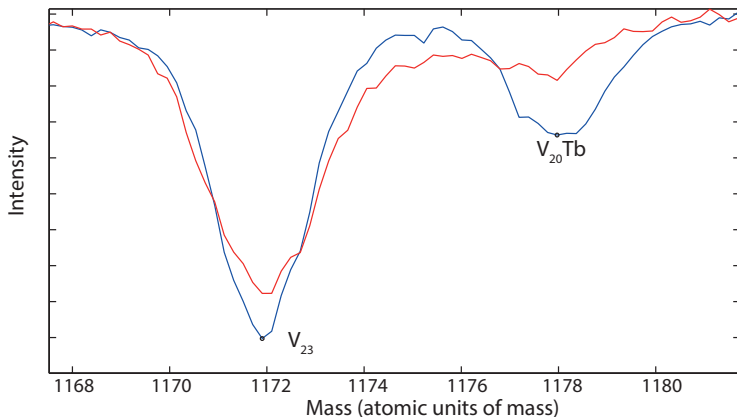
Figure 5.4: Magnetic deflections of V_{23} and V_{20}Tb clusters. Blue line for no magnetic field, red line for 1 T. The He pressure was 6 bar.

5.2.1 Temperature dependence

By checking the deflections at 40 K with a magnetic field of 0.5 T, shown in Fig. 5.5 it can be seen that the deflections are decreased, compared to those shown in Fig. 5.3. Interestingly, most of the deflection profiles for the smallest clusters are double sided, but not symmetric, possibly indicating locked magnetic moments. The effect is particularly strong for V_3Tb. The same behavior is observed for V_4Tb, V_5Tb and V_6Tb. Some larger clusters also show it, but the effect tends to vanish. This behavior indicates strong magnetic anisotropy.

The velocity of the measurement at 40 K was 586 m/s, while for the measurement at 25 K it was 475 m/s. In Fig. 5.6 the data are shown at 60 K. The magnetic field used was 0.75 T, while the He pressure was again 6 bar. The velocity was 691 m/s, which is almost 50% larger than it was for the measurements at 25 K. This is clearly noticeable in the deflections.

The behavior of V_nTb is thus clearly different from the one of V_nCo. The temperature dependence is similar, but as the magnetic moments are much larger, their deflections can be seen even for large sizes at relatively large temperatures compared to V_nCo. No single V_nTb cluster exhibits atomic-like behavior in the deflection profiles.

5.3 Tb doped Nb clusters

In this section we will study the effect of Tb-doping in Nb clusters. In order to create Tb doped Nb clusters a rod consisting in $Nb_{1-y}Tb_y$ (y=5%) was used. The magnetic deflections showed at Fig. 5.7 are the results obtained for a temperature
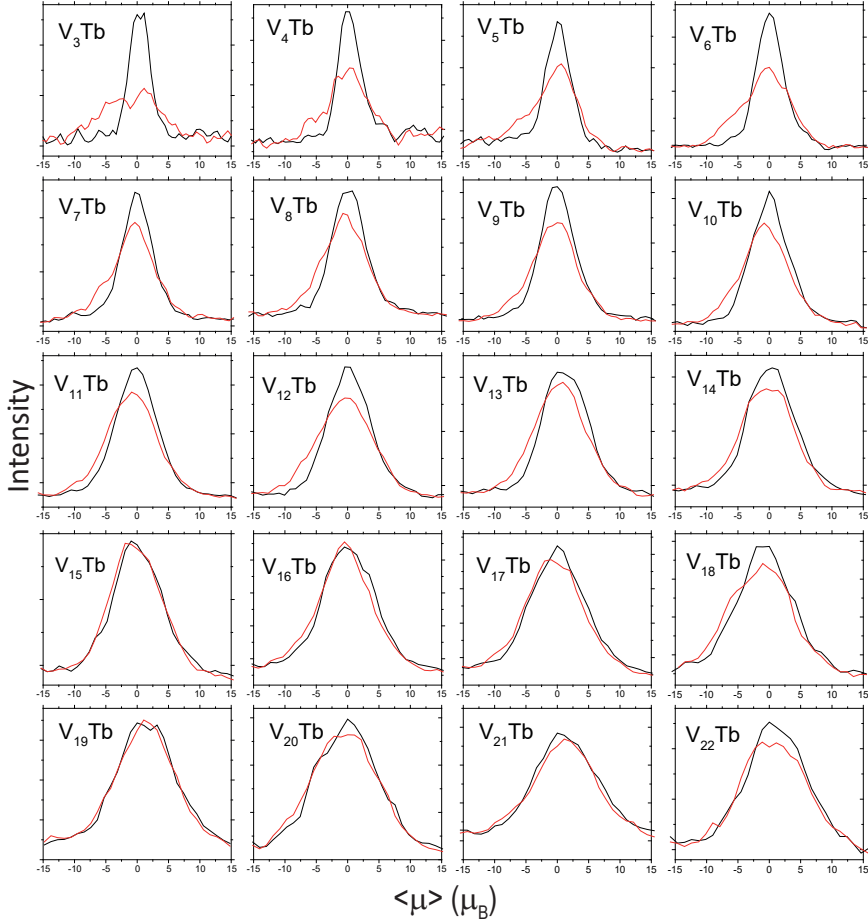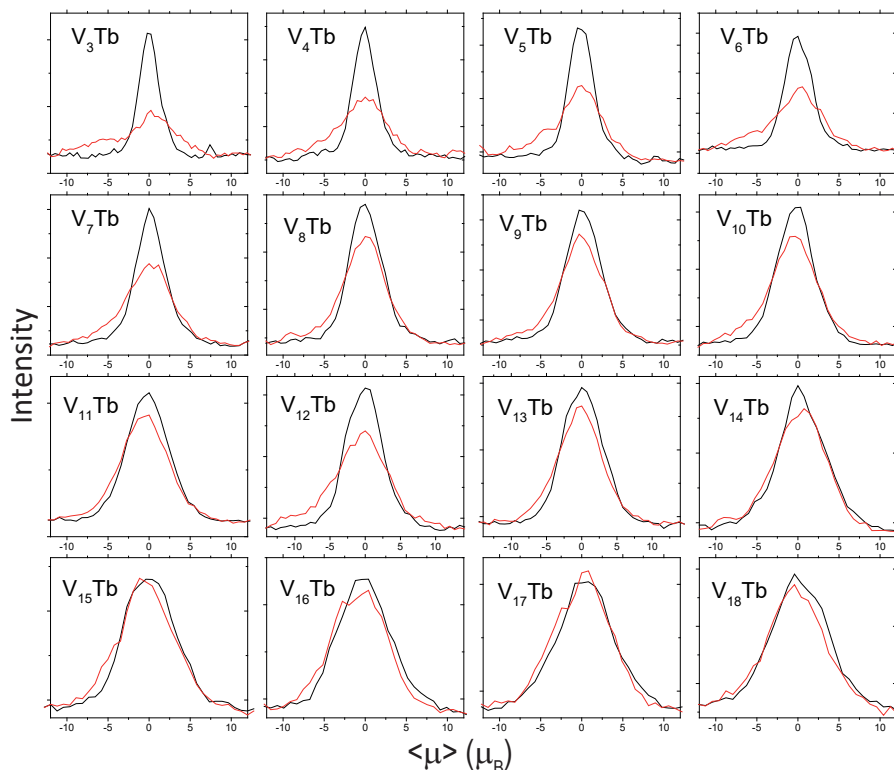
Figure 5.5: Magnetic deflections of V_nTb clusters at 40 K. Black line for no magnetic field, red line for 0.5 T. The He pressure was 6 bar.

of 25 K and the magnetic field of 0.5 T. The clusters traveled at 531 m/s.

Similarly as for the previous section, Tb can induce magnetization in Nb_n host. All the clusters deflected towards the direction of the strongest magnetic field. The smallest clusters, Nb_2Tb, Nb_3Tb, Nb_4Tb and Nb_5Tb, show asymmetric double-sided deflections, indicating magnetic moments locked to the lattice. This effect vanishes for the heavier clusters, which behave as superparamagnetic particles.

In Fig. 5.8 the evolution of the magnetic moment as a function of size for Nb_nTb is presented. It can be seen that the magnetic moment for every cluster is larger than the magnetic moment of the atomic Tb. Again this does not tell much about the nature of the magnetic moments, but since it is larger than for the atomic Tb, it is clear that Tb induces some net magnetic moment on the host. The magnetic moments vary with size, but changes are not significant. On average the magnetic moments measured for Nb_nTb are slightly larger than those of V_nTb, but the overall behavior is very similar. The temperature dependence is also very
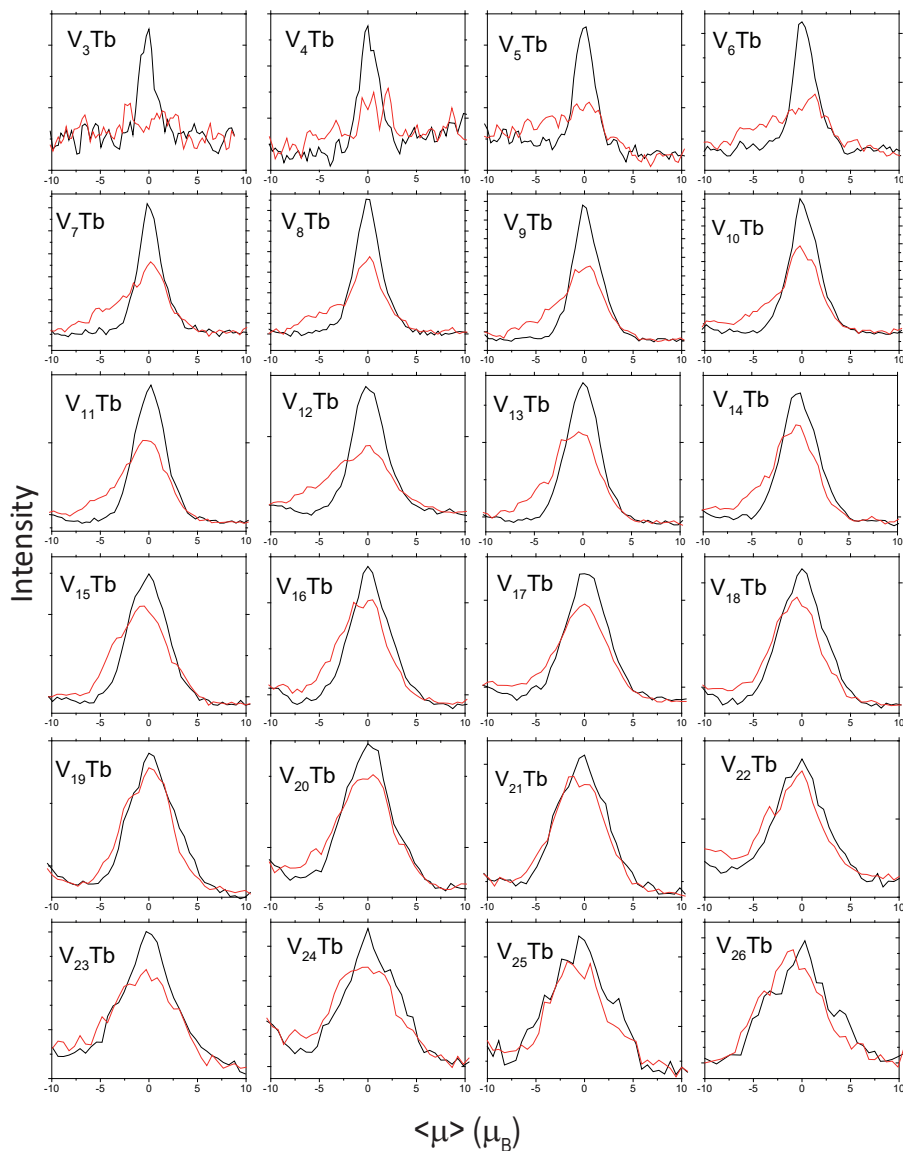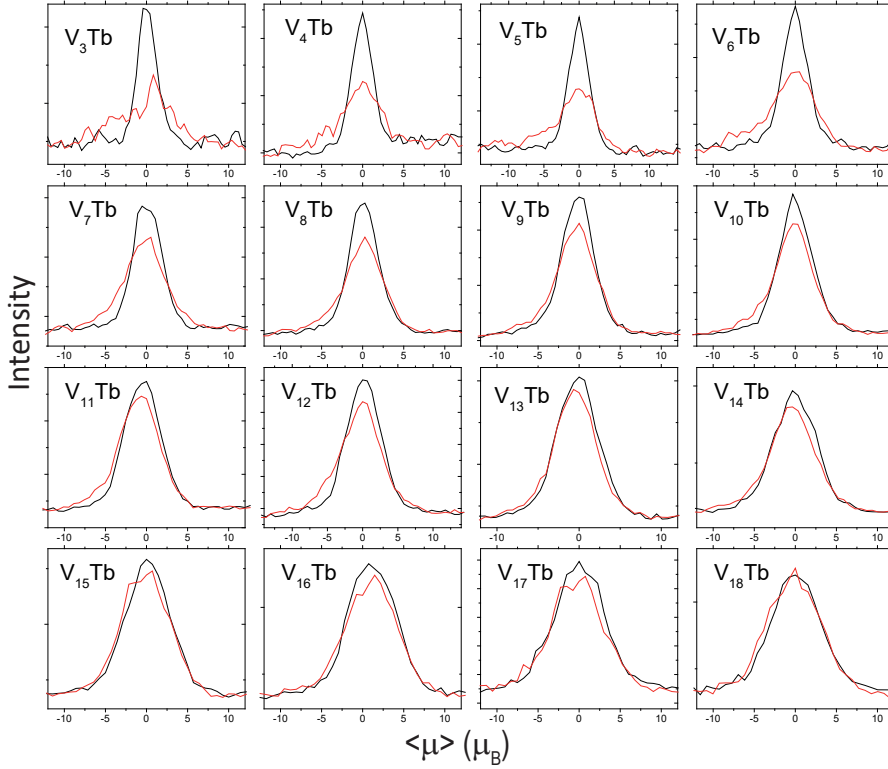
Figure 5.6: Magnetic deflections of V_nTb clusters at 60 K. Black line for no magnetic field, red line for 0.75 T. The He pressure was 6 bar.

similar to the one shown in the previous section for V_nTb.

5.4 Conclusions and outlook

In the previous chapter, we have shown that Co is not very efficient in inducing magnetic moments in V and Nb hosts. In the contrary, Tb is able to induce magnetic moments on both Nb and V clusters. Our measurements demonstrate that the magnetic moments are larger than the magnetic moment of Tb alone, which guarantees part of the total magnetic moment coming from the electrons of the hosts.

For further insight, geometrical structures of these clusters are necessary, that could further serve as a basis for computational theory. Therefore, ideally, experimental vibrational spectra of the clusters, combined with DFT calculations
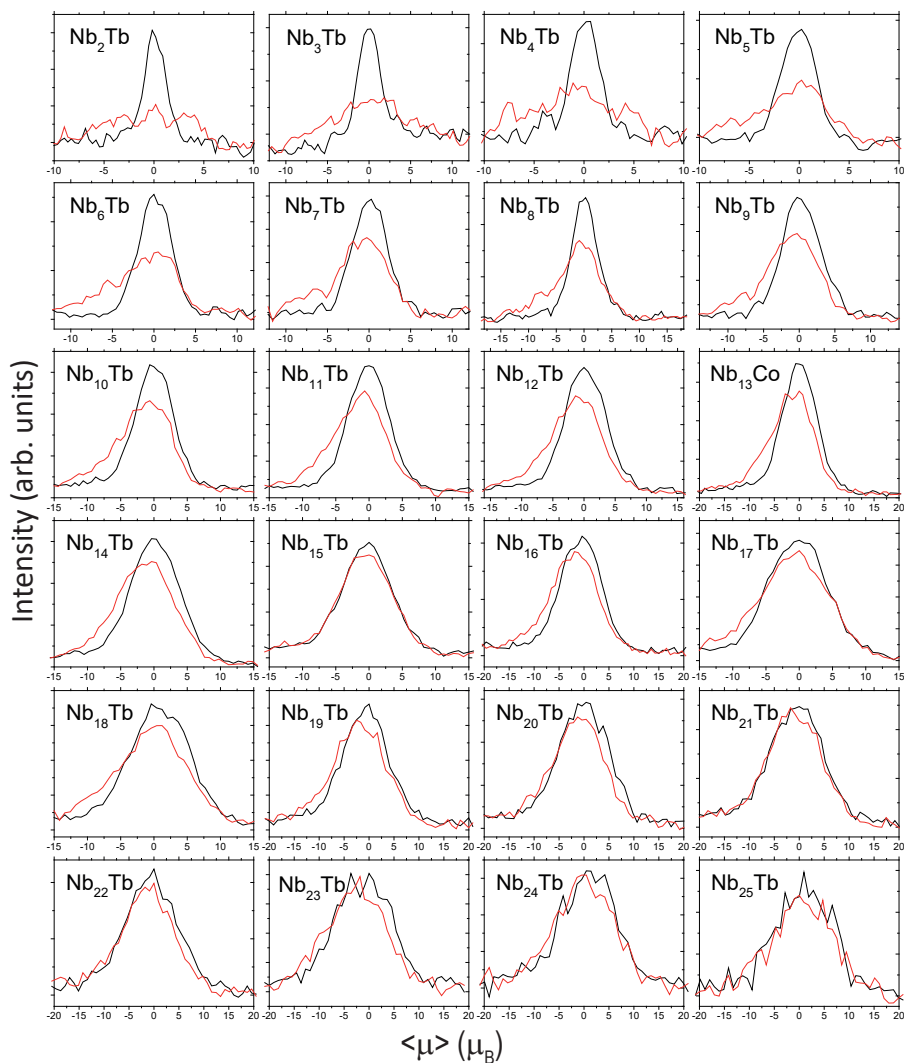
Figure 5.7: Magnetic deflections of Nb$_n$Tb clusters at 25 K. Black line for no magnetic field, red line for 0.5 T. The He pressure was 2 bar.
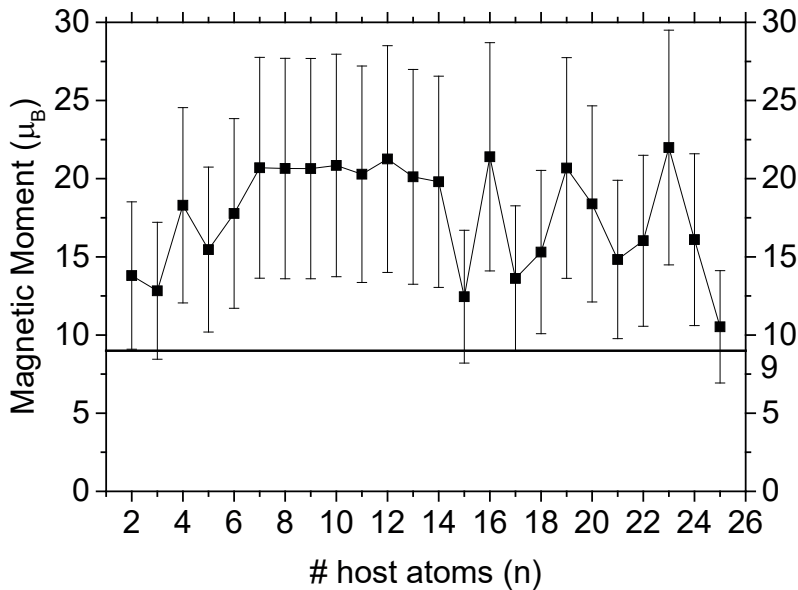
Figure 5.8: Magnetic moments of Nb$_n$Tb clusters as function of size.

in a similar fashion as described in Chap. 4 would be necessary. This is something for future research.

References

[1] C. N. van Dijk, Th. Rasing, A. Kirilyuk, J. Bowlan, A. Liang, and W. A. de Heer, "The effect of oxygen doping on the magnetism of Tb and Pr clusters," J. Appl. Phys. **107**, 09B526 (2010).

[2] J. Bowlan, C. N. van Dijk, A. Kirilyuk, A. Liang, S. Yin, Th. Rasing, and W. A. de Heer, "Size dependent magnetic moments and electric polarizabilities of free Tb, Ho and Tm clusters," J. Appl. Phys. **107**, 09B509 (2010).

[3] J. Jensen and A. R. Mackintosh, Rare Earth Magnetism (Clarendon Press, Oxford, 1991).

[4] W. C. Thoburn, S. Legvold, and F. H. Spedding, "Magnetic Properties of Terbium Metal," Phys. Rev. **112**, 56 (1958).

[5] D. E. Hegland, S. Legvold, and F. H. Spedding, "Magnetization and Electrical Resistivity of Terbium Single Crystals," Phys. Rev. **131**, 158 (1963).

[6] L. Vitali, S. Fabris, A. M. Conte, S. Brink, M. Ruben, S. Baroni and K. Kern, "Electronic Structure of Surface-supported Bis(phthalocyaninato) terbium(III) Single Molecular Magnets," Nano Lett. **8, 10**, 3364-3368 (2008).

[7] S. Stepanow, J. Honolka, P. Gambardella, L. Vitali, N. Abdurakhmanova, T.-C. Tseng, S. Rauschenbach, S. L. Tait, V. Sessi, S. Klyatskaya, Mario Ruben, and K. Kern, "Spin and Orbital Magnetic Moment Anisotropies of Monodispersed Bis(Phthalocyaninato)Terbium on a Copper Surface," J. Am. Chem. Soc. **132**, 11900-11901 (2010).

[8] M. Urdampilleta, S. Klyatskaya, J-P. Cleuziou, M. Ruben, and W. Wernsdorfer, "Supramolecular spin valves," Nat. Mat. **10**, 502-506 (2011).

[9] C. R. Ganivet, B. Ballesteros, G. de la Torre, J. M. Clemente-Juan, E. Coronado, and T. Torres, "Influence of Peripheral Substitution on the Magnetic Behavior of Single-Ion Magnets Based on Homo- and Heteroleptic Tb^{III} Bis(phthalocyaninate)," Chem. Eur. J. **19**, 1457-1465 (2013).

6   Oxygen doped samarium clusters

In this chapter the magnetic properties of samarium clusters doped with a single oxygen atom are studied. The measurements were done in the Stern-Gerlach setup described in chapter 2, as in all previous chapters. Samarium clusters have never been studied experimentally before. From theoretical point of view, however, a transition from fully non-magnetic to weakly magnetic is predicted to occur due to a valence change occuring at a size of 8 atoms[1]. These interesting predictions thus needed an experimental confirmation. Unfortunately, it was observed that with our current setup pure Sm clusters could not be synthesized due to the strong oxidation tendency of Sm. Instead, single-oxygen doped Sm_nO clusters happened to be the only species detected. Therefore, in this Chapter, we analyze the magnetic moments of the detected Sm_nO species. Since the oxygen contributes to the binding, the valence transition for Sm_nO clusters should occur for a smaller cluster size than for pure Sm clusters. Indeed from our experiments the valence transition is shown to occur for $n = 4$ Sm atoms instead of 8. Furthermore, the observed magnetic moment as function of cluster size for Sm_nO clusters is also interesting. For $n > 4$ there is a strong dependence of the magnetic moment on the cluster size. A large total magnetic moment is observed for Sm_6O, Sm_7O, $Sm_{13}O$ and $Sm_{14}O$ compared to the smaller moment for Sm_8O to $Sm_{12}O$ and $Sm_{15}O$ to $Sm_{18}O$.[*]

6.1   Introduction

The rare earth elements despite of their name are not hard to find, but usually they tend to occur together in nature, and difficult to separate from each other. The study of the magnetic properties of rare earth materials started in the 1930s, when the ferromagnetic properties of Gd were discovered. Nowadays it is one of the most important fields in physics of solid state magnetism. In general, the magnetic properties of rare earth metals can be understood according to the fact that the magnetic 4f electrons in metal have practically the same angular momentum quantum numbers as for the free ion. The magnetic exchange interaction is therefore of the Ruderman-Kittel-Kasuya-Yosida (RKKY) mechanism [2–4] transported by the electrons of conductivity. These interactions have been addressed by many researchers, both in experiments and theory. Phenomena such as intermediate valence [5, 6], valence fluctuations depending on chemical surrounding [7] or geometry [8, 9], or heavy-fermion behavior [10, 11] have been discussed.

Since the 4f electrons of rare earth metals are able to keep their properties also in metal phase, it could be expected that in the cluster regime they exhibit high net magnetic moments. As a confirmation, in terbium and oxygen-doped terbium clusters [12] large magnetic moments were observed, which strongly fluctuate with size, as can be seen in Fig. 6.1. Holmium clusters [13] showed similar behavior while in thulium clusters, much smaller magnetic moments were observed probably because of noncollinear magnetic structures [14].
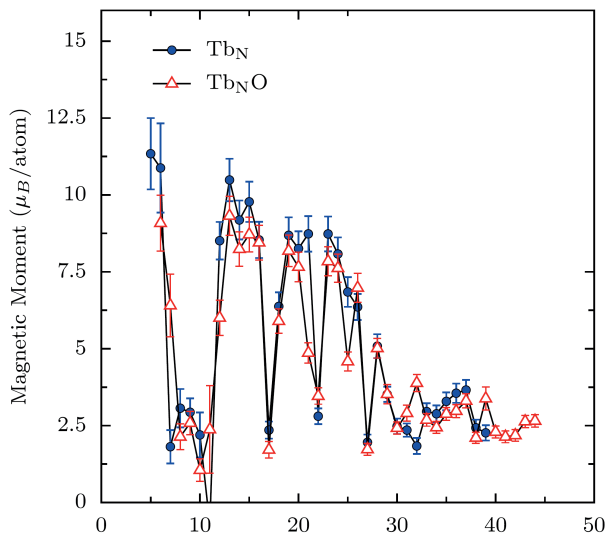
Figure 6.1: Magnetic moments of terbium and oxygen doped terbium clusters [12].

Atomic samarium possesses no net magnetic moment in the ground state. Its electronic structure is $[Xe]4f^6 6s^2$, which according to Hund's rules implies both spin and orbital moments of $S = L = 3$, with total angular momentum $J = 0$. In the bulk, samarium is typically trivalent, Sm^{3+}, and paramagnetic at room temperature, with effective magnetic moments below 2 μ_B, the third lowest among the lanthanides, including their oxides. Samarium becomes antiferromagnetic at 14.8 K [15]. According to Hund's rules an angular moment of $J = 5/2$ is expected for trivalent Sm^{3+}, which together with the consideration of the Landé g-factor corresponds to 0.845 μ_B [16, 17].

Because of Sm not being magnetic in the atomic form, and magnetic in the bulk, it is the cluster regime that is interesting to study. Indeed, it was predicted by using a combination of density functional theory and experimental information, i.e. the Born-Haber cycle, that there is a change of valence in the cluster regime [1]. More precisely, Sm clusters are predicted to be pure divalent up to 8 atoms and trivalent for larger cluster sizes. Note, that this change in valence is accompanied by a transition from non-magnetic to magnetic.

A valence transition from divalent to trivalent occurs for a rare-earth atom, when the energy cost of promoting a 4f electron to the [spd] band is smaller than the increase in binding energy due to this extra band electron. Typically, this gain in binding energy increases with the number of atoms to bind with. Thus the addition of oxygen to a Sm cluster allows for more bonds to be formed and an increase in binding energy. This is confirmed by the fact that oxygen is observed in our experiments to stick to the samarium clusters.

In this work we experimentally address the magnetic properties of $Sm_n O$ clusters. The measurements were done in the Stern-Gerlach-type magnetic deflection setup. Pure Sm clusters could not be produced with our current setup. The reason is twofold. First, the strong tendency of Sm clusters to oxidize and second the unability to suffieciently remove the oxygen from the setup. In addition, the cluster formation by itself could be triggered by the oxygen atom. However, $Sm_n O$ clusters showed interesting magnetic behavior and indirectly provide useful information on pure Sm clusters. Since the oxygen contributes to the binding, the valence transition for $Sm_n O$ clusters should occur for a smaller number of Sm atoms than in pure Sm clusters. Indeed from our experiments the valence transition is shown to occur for $n = 4$ Sm atoms instead of 8.

Furthermore, the observed magnetic moment as function of cluster size for $Sm_n O$ clusters is also interesting. For $n > 4$ there is a strong dependency of the magnetic moment on the cluster size. A large total magnetic moment is observed for $Sm_6 O$, $Sm_7 O$, $Sm_{13} O$ and $Sm_{14} O$ compared to the smaller moment for $Sm_8 O$ to $Sm_{12} O$ and $Sm_{15} O$ to $Sm_{18} O$.

6.2   Magnetic deflection of Sm_nO clusters

It must be said that the magnetic deflection study of Sm clusters is intriguing for all the mentioned reasons but also challenging. The main reason why it is challenging is because Sm has 7 stable isotopes. Note that the detection method is a position sensitive mass spectrometer, and a material possessing 7 isotopes will lead to extremely broad peaks, where combinations of all these isotopes will be present, an issue that will be increased with size.
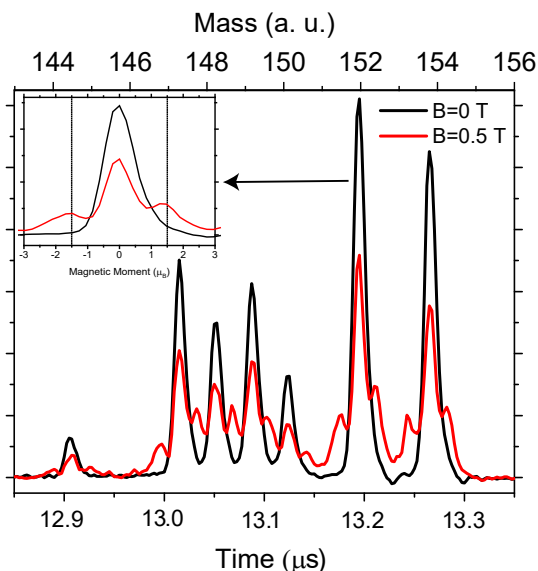
Figure 6.2: Samarium atomic stable isotopes deflected when crossed the magnetic field. Since their J=0 this was not expected. The spectra was obtained at 25 K. Bottom axis is shown in time units (μs), while top axis is calibrated in atomic units of mass. The inset shows the 6th isotope calibrated in magnetic moment units (μ_B), evidencing the splitting in three peaks, according to J=1.

The first issue that we found when tried to measure samarium clusters was that despite of being supposed to be non-magnetic, atomic Sm clearly reacts to the magnetic field, as shown in Fig. 6.2. All of the individual isotope peaks showed splitting in three parts. Note that except for the lightest isotope (the one at the left) and the two heaviest isotopes (the ones at the right), the deflected peaks overlap with the ones of the neighbor isotopes, as their mass is very close. By using the Al calibration we can check the value of the magnetic moment corresponding to the Sm atoms with $J = 1$, see inset in Fig. 6.2. This corresponds to the first excited state of Sm, as shown in the Table 6.1 below [18], where the lowest excited states of Sm are shown. The table shows that a magnetic moment of 1.5 μ_B, μ_J=Jg$_J\mu_B$,

corresponds to an excited state at 292.58 cm^{-1}, 36.3 meV.

Table 6.1: List of the lowest excited states for Sm atoms[18].

Configuration	Term	J	Level (cm^{-1})	g
$4f^6 6s^2$	^7F	0	0.00	
$4f^6 6s^2$	^7F	1	292.58	1.49839
$4f^6 6s^2$	^7F	2	811.92	1.49779
$4f^6 6s^2$	^7F	3	1489.55	1.49707
$4f^6 6s^2$	^7F	4	2273.09	1.49625
$4f^6 6s^2$	^7F	5	3125.46	1.49532
$4f^6 6s^2$	^7F	6	4020.66	1.49417

......

By knowing the energy of the excited state, the temperature of the atoms can estimated, as from the height of the peaks the ratio between excited atoms versus the atoms in the ground state can be found. Then the Boltzmann distribution gives the relative population of energy states (usually the ratio of excited states to ground state) for a given temperature.

$$\frac{N_f}{N_i} = exp\left(-\frac{\Delta E}{k_B T}\right) \tag{6.1}$$

where N_f is the intensity of the deflected peaks (the sum of both), N_i is the intensity of the undeflected peak, ΔE is the difference in energy between the excited state and the ground state, k_B=1.381x10^{-23} J/K is the Boltzmann constant and T is the temperature in Kelvins.

The temperature obtained for samarium atoms showed at Fig. 6.2 is quite high, ~1130 K. For all other experiments the temperature showed similar values, regardless of all changes in pressure or nozzle. This means that after the atoms are melted and eventually vaporized they do not cool down enough. This was not observed for the other atomic species studied in this thesis, Al and Y.

Next, while the goal of these measurements was to study the magnetic deflections of pure samarium clusters, these were actually never observed in the mass-spectra. Instead, oxygen doped samarium clusters were obtained. There are several possible explanations that may lead to that. The most obvious is that rare earth metals in general have a huge tendency to get oxidized. Thus, it appears probable that by firing the rod with a powerful laser beam, oxidation reaction may take place.

Knowing the tendency of rare earth metals to get oxidized, the Sm rod is always stored inside vacuum, at pressure values around 1x10^{-5} mbar. Nevertheless this did not help to get rid of the oxygen in the clusters. We have also tried to

clean the tube where the carrier gas is flowing, by having it connected to a pump the previous 10-12 hours prior to the measurements, in order to avoid oxygen to be attached to the walls; it also did not help, not even when the tube was heated to help oxygen atoms to detach from the walls of the tube. The rod was polished before the measurements, just to get rid of the first layers of the rod, where the oxygen is more likely to be attached, which also did not help.

Therefore, the conclusion was that for some reason Sm clusters cannot nucleate without the oxygen atom. Interestingly, no Sm clusters were obtained with more than one oxygen as doping, which also points in the direction of the nucleation issue. It is interesting to note that the dimer SmO was never obtained, at least its intensity was never high enough to be detected in the spectra. It may also happen that as the Sm atoms are excited it is harder for them to nucleate without the assistance of oxygen.

From the theoretical work of Ref. [1] it is predicted that for pure Sm_n clusters a valence transition occurs at $n = 8$. This change in valence is accompanied by a non-magnetic to magnetic transition, which can be observed experimentally with a magnetic deflection setup. Similarly, a valence and thus non-magnetic to magnetic transition is expected for Sm_nO clusters. However, due to the contribution to the binding of the oxygen this transition should occur for smaller cluster sizes, i.e. smaller n. Further, it should be noted that above the valence transition only magnetic moments of $1\ \mu_B$ per atom are expected. Also, the valence transition might be accompanied by a regime of mixed valence, so magnetic moments can be even smaller than $1\ \mu_B$ per atom. In addition, possible non-collinearity and/or ferrimagnetic ordering of the magnetic moments has the same effect.

The atomic mass of Sm ranges from 143.91 a.u. of mass to 153.92 a.u. of mass, depending on the isotope. In Fig. 6.3 the mass distribution for $Sm_{13}O$ is represented, both the measured one and the simulation.

It can be seen that the correlation between simulation and measurement is good and that the peak is really broad, having a half width at half maximum around 20 a.u. of mass. This gives an idea about the difficulty of such a measurement, as the resolution is much worse than the expected deflections. This figure also evidences the noise involved in these measurements.

In Fig. 6.3, also the deflected profile of $Sm_{13}O$ is shown. It can be observed that despite being noisy and broad, both peaks are quite symmetric, allowing a Gaussian fit to be applied. The difference between both peaks gives a good estimation of the deflection. As we can expect that the magnetic properties of all different combinations of isotopes are equivalent, the deflection of the whole peak should be equivalent to the deflection of every single peak inside the distribution.

In Fig. 6.4 the deflection profiles of some other clusters are shown as well. One can distinguish two rather different types of behavior, clusters which are deflecting and clusters which are not. The evolution of the magnetic moment as function of size is summarized in Fig. 6.5.

From Fig. 6.5 the valence transition visible as a transition from non-magnetic to magnetic Sm_nO clusters occurs at $n = 4$, which is indeed smaller than $n = 8$ for
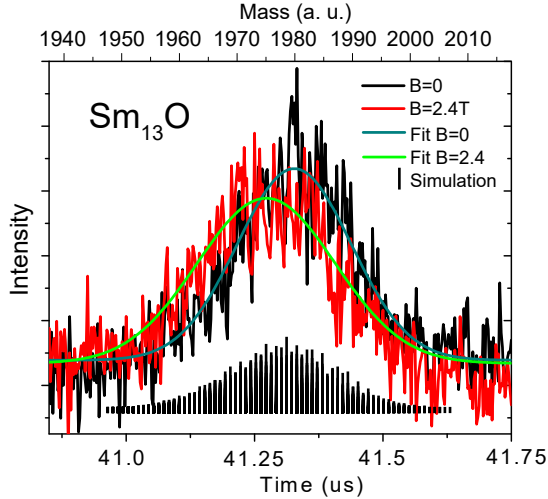
Figure 6.3: $Sm_{13}O$ deflection. Raw data and Gaussian fits for both curves. Temperature is 25 K. The simulation of the peak, obtained using [19], shows good agreement with the experimental data. The bottom axis is in time units while the top axis is calibrated in atomic units of mass. Note that the calibration is applied to the undeflected peak.

pure Sm clusters. This could be the result of the oxygen which contributes to the binding. Further, the magnetic clusters show an interesting behavior as function of cluster size. A large total magnetic moment is observed for Sm_6O, Sm_7O, $Sm_{13}O$ and $Sm_{14}O$ compared to the much smaller moment for Sm_8O to $Sm_{12}O$ and $Sm_{15}O$ to $Sm_{18}O$. In case of a mixed valence regime around $n = 4$ it would be expected that Sm_6O and Sm_7O would have smaller moments than Sm_8O and larger, which is clearly not observed. On the other hand the small moment of Sm_5O might be explained by the presence of mixed valence. Further, the difference between the relatively large total magnetic moments around $10 \, \mu_B$ and small moments around $4 \, \mu_B$ could be due to non-collinearity and/or ferrimagnetic ordering of the local moments. However, at this point we can only speculate on the physical origin of the observed magnetic behavior for $n > 4$ and further studies are required to shed light on this.

6.3 Conclusions

The main goal of these measurements was to confirm experimentally the divalent-trivalent transition in Sm clusters, at the size close to Sm_8. This behavior could not be confirmed, as pure Sm_n clusters were never obtained. There are several
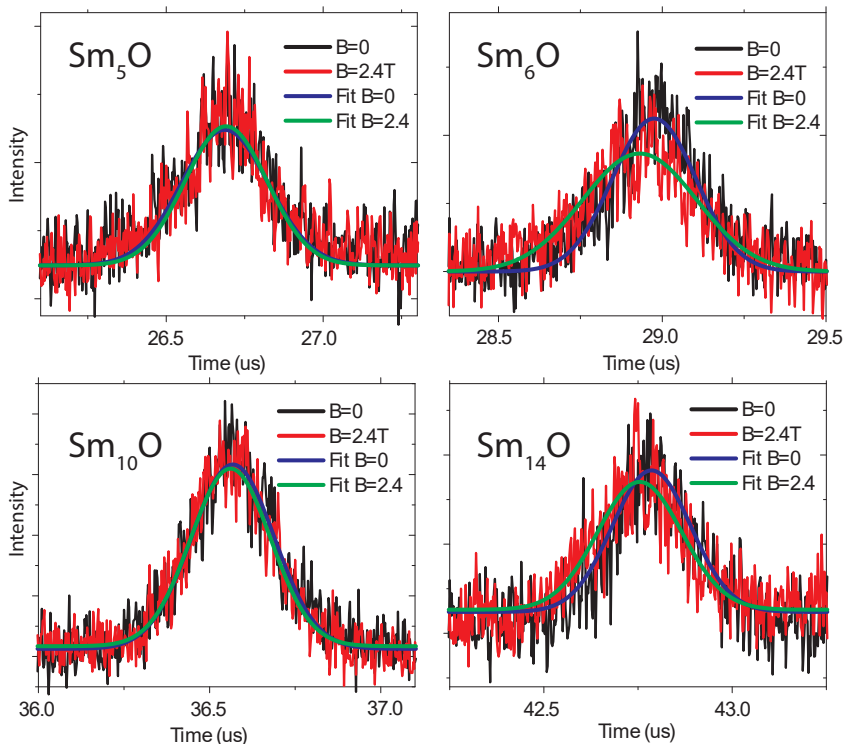
Figure 6.4: Spectra for Sm_5O, Sm_6O, $Sm_{10}O$ and $Sm_{14}O$ deflections. Raw data and Gaussian fit for both curves are shown. Temperature is 25 K.

reasons to explain why the detection of pure Sm_n failed. First, it is the tendency for rare earth elements in general and samarium in particular to get oxidized. Second, most probably an oxygen atom may assist the nucleation and in such way can help to stabilize the cluster.

Once Sm_nO were obtained, we studied them with magnetic deflection experiments. The results show that the magnetic moments depend strongly on the cluster size. Thus, the smallest clusters in the spectra Sm_4O and Sm_5O have no net magnetic moment within the error bar; Sm_6O and Sm_7O have net magnetic moments closer to 2 μ_B per atom. The next clusters have very small to none magnetic moments again. Then, $Sm_{13}O$ and $Sm_{14}O$ have magnetic moments larger than 10 μ_B, which might be about 1 μ_B per atom. The rest of the clusters have lower magnetic moments, most of them no net magnetic moment within the error bar. This behavior could be explained by the migration of Sm atoms from divalent, when there is no net magnetic moment, to trivalent when there is net magnetic moment. The origin of this still needs to be explained.
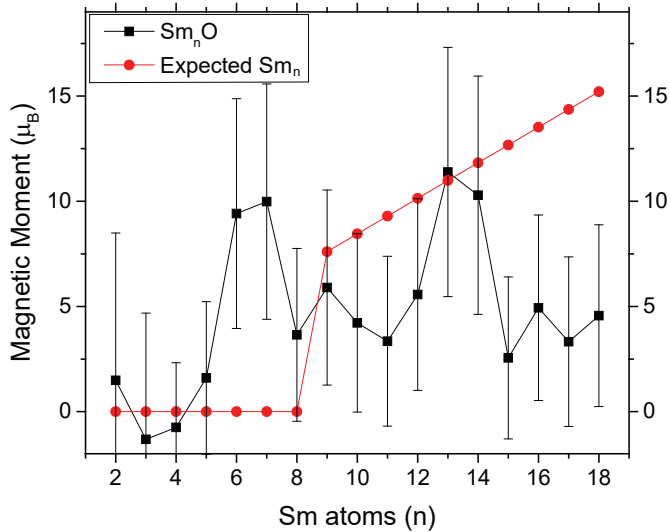
Figure 6.5: Sm$_n$O clusters magnetic moments as function of size.

References

[1] L. Peters, I. Di Marco, M. S. Litsarev, A. Delin, M. I. Katsnelson, A. Kirilyuk, B. Johansson, B. Sanyal, and O. Eriksson, "Valence and spectral properties of rare-earth clusters," Phys. Rev. B. **92**, 035143 (2015).

[2] M. A. Ruderman and C. Kittel, "Indirect exchange coupling of nuclear magnetic moments by conduction electrons," Phys. Rev. **96**, 99-102 (1954).

[3] T. Kasuya, "A Theory of Metallic Ferro- and Antiferromagnetism on Zener's Model," Prog. Theor. Phys. **16**, 45-57 (1956).

[4] K. Yosida, "Magnetic Proyerties of Cu-Mn Alloys," Phys. Rev. **106**, 893-898 (1957).

[5] G. K. Wertheim and M. Campagna, "Is samarium metal in an intermediate valence state?," Chem. Phys. Lett. **47**, 182-184 (1977).

[6] H. Bilz, G. Guntherodt, W. Kleppmann, and W. Kress, "Phonon Anomalies and Electron-Lattice Coupling in Intermediate-Valence $Sm_{0-25}Y0 - 75S$,"

Phys. Rev. Lett. **43**, 1998-2001 (1979).

[7] D. Gignoux, F. Givord, R. Lemaire, and F. Tasset, "Intermediate valence state of Ce in CeNi," J. Less-Comm. Metals. **94**, 165-172 (1983).

[8] A. T. Holmes, D. Jaccard, and K. Miyake, "Signatures of valence fluctuations in CeCu$_2$Si$_2$ under high pressure," Phys. Rev. B. **69**, 024508 (2004).

[9] M. Campagna, E. Bucher, G. K. Wertheim, D. N. E. Buchanan, and L. D. Longinotti, "Spontaneous Interconfiguration Fluctuations in the Tm Monochalcosenides," Phys. Rev. Lett. **32**, 885 (1974).

[10] G. R. Stewart, "Heavy-fermion systems," Rev. Mod. Phys. **56**, 755-787 (1984).

[11] E. D. Bauer, N. A. Frederick, P. -C. Ho, V. S. Zapf, and M. B. Maple, "Superconductivity and heavy fermion behavior in PrOs$_4$Sb$_{12}$," Phys. Rev. B. **65**, 100506 (2002).

[12] C. N. van Dijk, Th. Rasing, A. Kirilyuk, J. Bowlan, A. Liang, and W. A. de Heer, "The effect of oxygen doping on the magnetism of Tb and Pr clusters," J. Appl. Phys. **107**, 09B526 (2010).

[13] J. Bowlan, C. N. van Dijk, A. Kirilyuk, A. Liang, S. Yin, Th. Rasing, and W. A. de Heer, "Size dependent magnetic moments and electric polarizabilities of free Tb, Ho, and Tm clusters," J. Appl. Phys.**107**, 09B509 (2010).

[14] C. van Dijk, J. Bowlan, W. A. de Heer, Th. Rasing, and A. Kirilyuk, "Unusual Temperature Dependence of Magnetization and Possible Magnetic Non-collinearity in Tm and Pr Clusters," J. Phys. Chem. C **119**, 11153-11159 (2015).

[15] P. G. Huray, S. E. Nave, and R. G. Haire, "Magnetism of the heavy 5f elements," J. Less-Comm. Metals. **93**, 293-300 (1983).

[16] A. M. Stewart, "Paramagnetic Susceptibilities of Metallic Samarium Compounds," Phys. Rev. B **6**, 1985-1998 (1972).

[17] A. M. Stewart, "Gyromagnetic Ratios of Metallic Samarium Compounds," Phys. Rev. B **8**, 2214-2221 (1973).

[18] W. C. Martin, R. Zalubas, and L. Hagan, *Atomic Energy Levels - The Rare-Earth Elements* (NSRDS-NBS 60, 1978).

[19] http://www.sisweb.com/mstools/isotope.htm

7 Magnetic properties of Co clusters and Rh doped Co clusters

In this chapter we study the magnetic properties of pure and Rh-doped Co clusters. Co clusters have been studied by several groups and shown magnetic moments that are typically larger than those of the bulk. The aim of this chapter is to study Rh doping of Co clusters to compare them with both pure Co clusters as well as with the existing data on Co_nRh^+ cation clusters. The large magnetic moment of the 3d materials in combination with a high spin-orbit coupling of the 4d or 5d materials give rise to a material with a large magnetization and a strong magnetic anisotropy, thus making them ideally suitable in for example magnetic storage devices. Especially for clusters, which already have a higher magnetic moment compared to the bulk, these alloys can profit from the cooperative role of alloying and size reduction in order to obtain magnetically stable materials with a large magnetic moment.

The results of our experiments have shown that in contrast to what happens for cations, no considerable changes are observed in neutral clusters when exchanging one Co atom by a Rh atom, as the difference in total magnetic moment is never larger than the 10% of the total value, which is within the measurement error.

7.1 Introduction

Cobalt clusters have been object of many studies. Some theoretical studies focused on the structure [1, 2], while experimentally IR-MPD (Infrared multiple photon dissociation) spectroscopy was used to determine the structure first of cations [3] and then of neutral clusters [4]. Photoionization studies obtained the ionization potentials [5]. As for its magnetic properties, in the cluster regime Co has also been proven to be ferromagnetic, both theoretically [2, 6, 7] and experimentally [8–10].

For their part, small rhodium clusters were found to possess some magnetic moments [11–13], up to 1 μ_B per atom, which makes it the only 4d element with ferromagnetic order at the nanoscale. Also some theoretical works studied the magnetic and structural properties of Rh clusters [14, 15], where size dependence of the magnetic properties of the Rh_n clusters was found in rough agreement with the previously mentioned experimental works [11, 12].

Co clusters have large magnetic moments, due to their 3d electrons, while Rh has the typical strong spin-orbit coupling of the 4d-5d metals. The combination of the two might be able to make clusters which possess the combination of large magnetic moments with strong magnetocrystalline anisotropy. The capability of the 3d electrons to induce magnetic moments on the 4d electrons in alloys has already been demonstrated in the bulk [16], as well as for chemically prepared nanoparticles in a polymer matrix [17]. Rh-doped Co clusters have also been a subject of theoretical studies, some of which did take into account the spin-orbit coupling [18, 19] and others did not [20, 21]. Interestingly, the cations of Rh-doped Co were already studied by X-Ray Magnetic Circular Dichroism (XMCD), and the results demonstrated drastic changes upon the exchange of one Co atom for the Rh atom for some cluster sizes [22]. For instance, an increase in the orbital moment of 150% was observed when going from Co_{13}^+ to $Co_{12}Rh^+$ [22].

The goal of the present study was to verify whether a similar behavior could also be observed for neutral Co_nRh clusters.

7.2 Results of magnetic deflections experiments on pure and Rh-doped Co clusters.

The deflection experiments shown in this chapter were carried out in a similar way as the ones described in the previous chapters. There are only some small technical differences, such as the skimmer had a 2 mm diameter, while in the previous chapters its width was just 1 mm. The source was slightly different here, in particular the extension tube was shorter, just 20 mm instead of the one of 25 mm used for the rest of the measurements.

The most important difference relies on the voltages used for the time of flight, as the voltage on the extractor was 3.8 kV instead of 3.6 kV used in all the previous chapters. The reason to use a different voltage is to achieve a better

resolution in exchange of position sensitivity, to improve the signal/noise ratio as well as the separation of peaks with different compositions. As can be seen in Fig. 2.13, the difference in position sensitivity by using 3.8 kV instead of 3.6 kV is about 50%; for instance for Co_{10} the sensitivity for an extractor voltage of 3.8 kV is 5.42 ns/mm, while using 3.6 kV it would be 9.63 ns/mm. One of the consequences of these changes is that the obtained peaks look broader when the calibration was used.

The clusters were thus produced in the source chamber by ablation of a $Co_{1-y}Rh_y$ (y = 10%) rod with a Nd:YAG laser producing 532 nm light. Beside pure Co clusters, Rh-doped Co clusters were created, not only $Co_{n-1}Rh$ clusters, but also $Co_{n-2}Rh_2$ and $Co_{n-3}Rh_3$, even though the signal for the latter was very low.

In Figs 7.1, 7.2 and 7.3 the deflections for the 3 species obtained at a 60 K are shown. The velocity of the clusters was 685 m/s, while the He pressure was 1.8 bar. Two different magnetic fields were used, 0.5 and 1 T. In these figures pure Co clusters between Co_9 and Co_{22} are shown, and next to them are shown both Co_nRh and Co_nRh_2.

As can be seen at Figs. 7.1, 7.2 and 7.3 all the studied clusters are superpara-magnetic, characterized by deflections towards the region of the strongest magnetic field. Further, the magnetic moments are large, especially when compared to those shown in the previous chapters. The summary of magnetic moments obtained from these measurements is presented in Fig. 7.4. It can clearly be seen that for all the studied clusters the magnetic moments exceed the bulk value for Co, which is 1.72 μ_B per atom. All the studied sizes for the three species have magnetic moments between 2.5 and 3 μ_B per atom, except from Co_9 to Co_{12} whose magnetic moment is between 3 and 3.5 μ_B per atom and from Co_9Rh to $Co_{11}Rh$ and from $Co_{10}Rh_2$ and $Co_{12}Rh_2$. The largest magnetic moment is for $Co_{10}Rh$, 3.6 μ_B per atom. For the three species it can be seen that the larger magnetic moments per atom are found for the smallest clusters; then all three series show a tendency to decrease.

In general no drastic changes are observed when adding a Rh atom or even two, meaning that the added Rh atoms do not change much the magnetic moment of Co part. In particular, the doping with single Rh atom does not change the total magnetic moment at all - if any, a slight increase can be noticed. The largest change is for the case of Co_{22} whose magnetic moment is 2.12 μ_B per atom and after gaining a Rh atom achieves a magnetic moment of 2.50 μ_B per atom. Co_{11} increases its magnetic moment of 3.09 μ_B per atom upon Rh doping to 3.43 μ_B per atom and Co_{17} increases its magnetic moment from 2.41 μ_B per atom to 2.64 μ_B per atom after doping.

The doping with two Rh atoms leads to some decrease of the total magnetic moment. For the smallest clusters it decreases the total magnetic moment rather significantly, up to 0.5 μ_B per atom, which is the case for Co_9, whose magnetic moment is decreased from 3.07 μ_B per atom to 2.61 μ_B per atom. Another cluster whose magnetic moment significantly decreases after acquiring two Rh atoms is
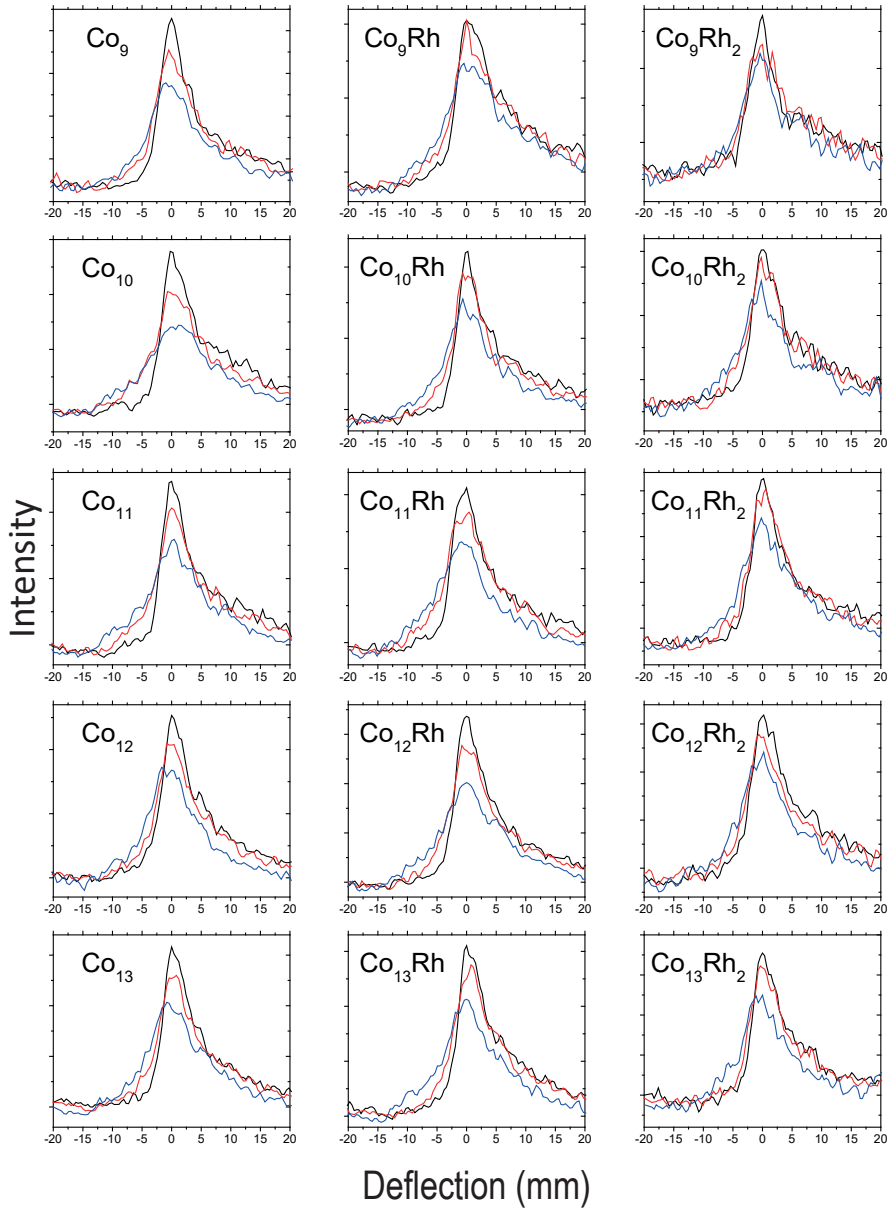
Figure 7.1: Magnetic deflections of Co_n, Co_nRh and Co_nRh_2 for $9 \leq n \leq 13$ at 60 K. Black line is for no magnetic field, while red and blue lines correspond to the field of 0.5 and 1 T.
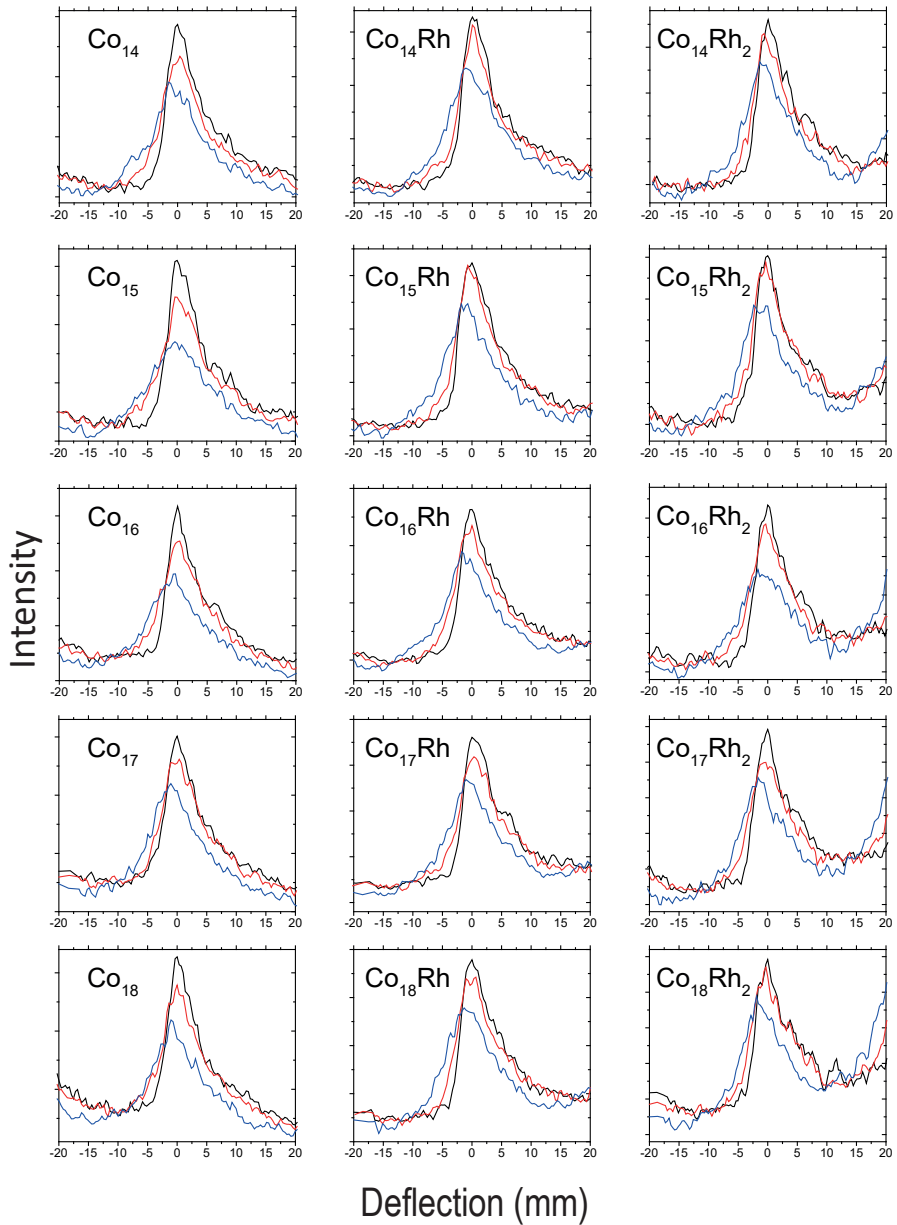
Figure 7.2: Magnetic deflections of Co_n, Co_nRh and Co_nRh_2 for $14 \leq n \leq 18$ at 60 K. Black line is for no magnetic field, while red and blue lines correspond to the field of 0.5 and 1 T.
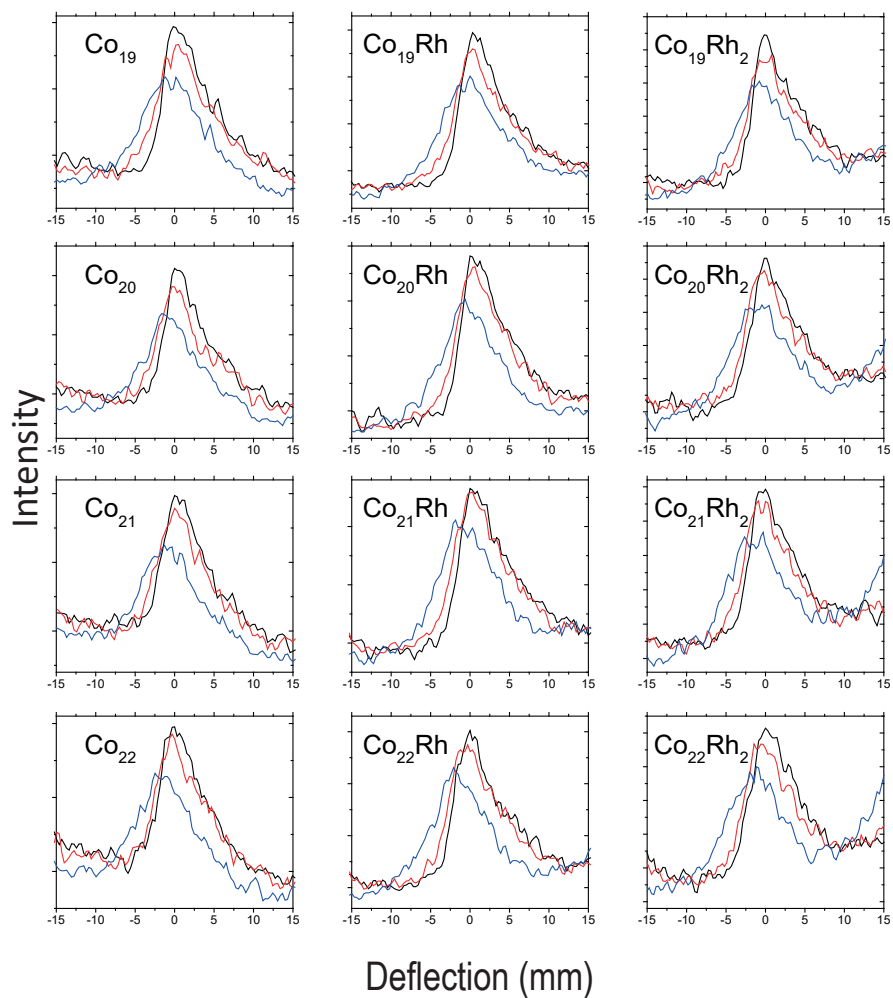
Figure 7.3: Magnetic deflections of Co$_n$, Co$_n$Rh and Co$_n$Rh$_2$ for 19≤n≤22 at 60 K. Black line is for no magnetic field, while red and blue lines correspond to the field of 0.5 and 1 T.
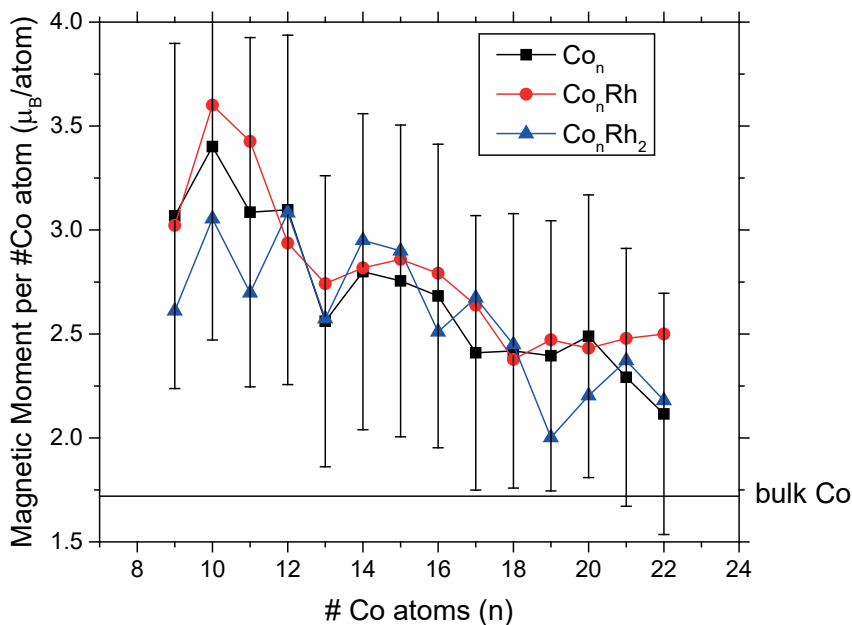
Figure 7.4: Magnetic moments of Co_n, Co_nRh and Co_nRh_2 clusters as function of the number of Co atoms. To ease the eye only the error bars for pure Co clusters are shown.

Co_{19} as its magnetic moment is decreased from to 2.39 μ_B per atom to 2.00 μ_B per atom. There are also some clusters whose magnetic moment is somewhat increased after double Rh doping. The most significant case is Co_{17} whose magnetic moment got increased from 2.41 μ_B per atom to 2.67 μ_B per atom, after the addition of 2 Rh atoms .

Taking all these results into account, and taking the error bar into account we do not find any single case where the Rh doping greatly increases the total magnetic moment, as all the previously mentioned changes lie within the error bar.

Unfortunately in the Stern-Gerlach experiment no distinction between the spin and the orbital contribution can be done, thus we can not directly verify the results of Ref. [22] where $Co_{12}Rh^+$ has its orbital magnetic moment increased by an impressive 160% with respect to Co_{13}^+. However, one should note a different line of reasoning there: instead of comparing $Co_{12}Rh^+$ with Co_{13}^+, one could consider $Co_{12}Rh^+$ with Co_{12}^+. In Ref. [22], no large increase for the total magnetic moment
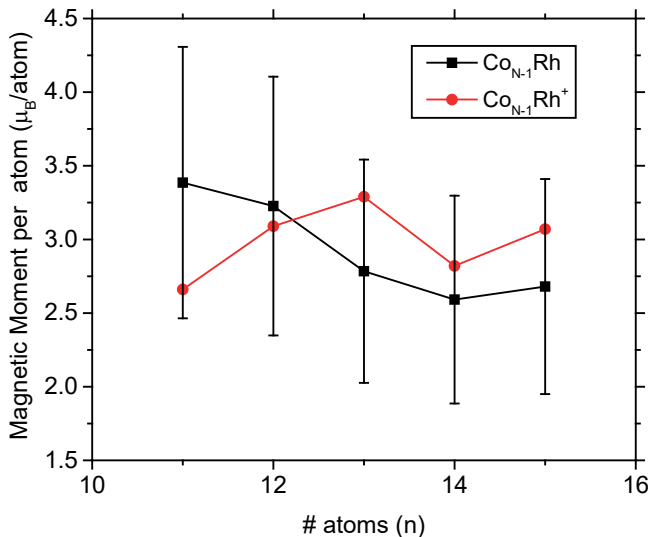
Figure 7.5: Comparison of total magnetic moments for $Co_{n-1}Rh$ for neutral clusters (this study) and $Co_{n-1}Rh^+$ [22]

was found. There, the most interesting cases were clusters whose spin- or orbital magnetic moments were strongly enhanced upon the exchange of one Co atom by a Rh atom. In any case no straightforward comparison can be make, as the removal of an electron might result in structural, electronic and magnetic changes. Fig. 7.5 shows the results of both studies. It can be seen that the cationic magnetic moments lie within the error bar of our data for the neutrals. Interestingly, $Co_{10}Rh$ has a magnetic moment of 3.39 μ_B per atom while after ionization the value is decreased to 2.66 μ_B. On the other hand $Co_{12}Rh$ has a magnetic moment of 2.78 μ_B per atom which after ionization is increased to 3.29 μ_B per atom.

It is also interesting to compare the results obtained for pure Co clusters with those of other works, as it was previously mentioned that such clusters were subject of several earlier studies. The results of some of the most relevant theoretical works are shown in Fig. 7.6(a). It can be concluded that our results provide slightly larger magnetic moments than those predicted by the majority of the references. One should however take into account the fact that the theoretical values are limited to the spin moments only.

The results of some of the most relevant experimental works are shown in Fig. 7.6(b). Our results for the smallest sizes, from Co_9 to Co_{12} are similar to those of Ref. [9] even though for larger sizes they differ by about 0.5 μ_B/atom. For the larger values our values are similar to the ones shown in Ref. [23], where Co_{12}
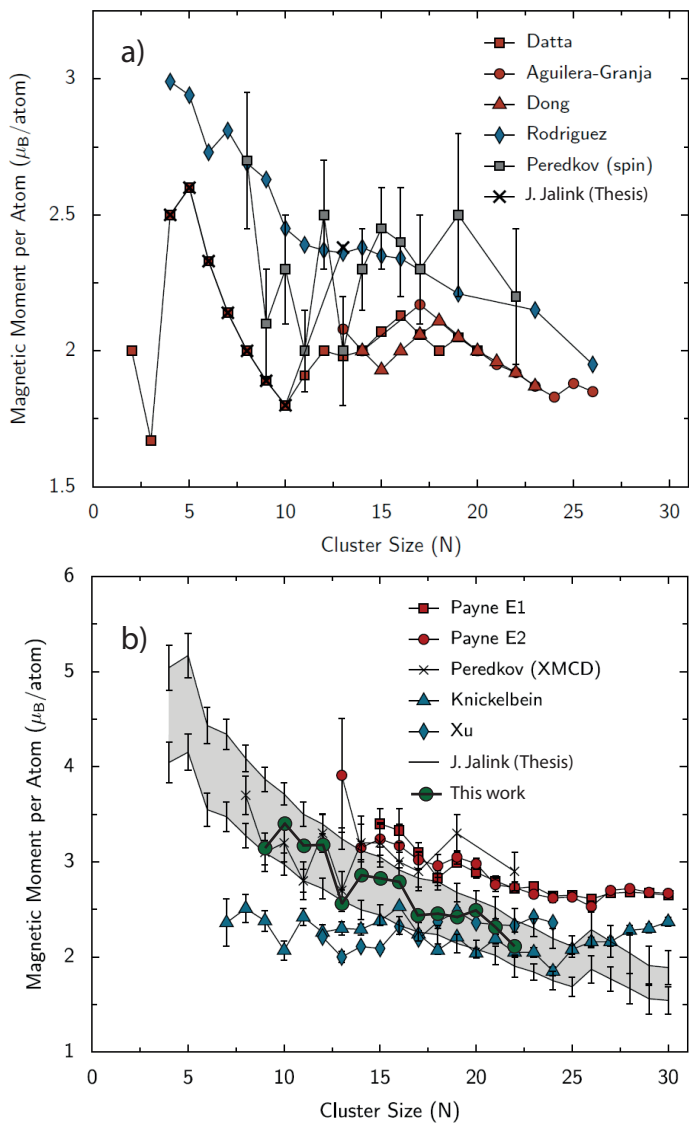
Figure 7.6: Literature for: a) theoretical magnetic moments from Refs. [2, 6, 7, 9, 24, 25] and b) experimental magnetic moments from Refs. [9, 23, 25–27] for Co clusters. Adapted from J. Jalink, Ph.D. thesis [25]

was the smallest size studied. The rest of the studies deviate quite significantly from our data as well as between themselves.

Thus we can conclude that our results are generally in line with other previ-

ous studies, both theoretical and experimental. There are many different studies showing rather different results, but at least this rather preliminary study gives values comparable to them.

There are no data for Co clusters doped with two Rh atoms available, at least to our knowledge. In Chapter 4 we have shown that Co electrons within the Nb host have a tendency to hybridize, while here we can see that when doping the other way around, a 3d metal, Co, with a 4d metal, Rh, we may achieve the same effect, a hybridization of some 3d electrons with those of impurity, and because of this the total magnetic moment is reduced. This seems reasonable to expect, given the generally non-magnetic (or weakly magnetic) behavior of Rh.

7.3   Conclusions and outlook

After studying both Co and Rh doped Co clusters we found all of them being magnetic, deflecting in a superparamagnetic way as expected. Though their magnetic moments clearly depend on the cluster size, no real change of the Co magnetism was observed. Doping Co clusters with two Rh atoms in general lead to a certain decrease of their magnetic moments, specially for the smallest clusters studied. Therefore, the previously observed strong changes in either spin or orbital magnetic moments could not be verified in our measurements.

As previously mentioned, it would be interesting to repeat these series of experiments under better conditions, in order to improve the signal-to-noise ratio.

Taking into account the results of Ref. [22], it would also be interesting to study Au doped Co clusters. From Ref. [28] we learn that Au as host barely interacts with magnetic impurities. In the previous work, with Au being the impurity itself [22], it was shown how it might be responsible for changes in the magnetic properties.

References

[1] C. Jamorski, A. Martinez, M. Castro, and D. R. Salahub, "Structure and properties of cobalt clusters up to the tetramer: A density-functional study," Phys. Rev. B **55**, 10905 (1997).

[2] J. Rodríguez-López, F. Aguilera-Granja, K. Michaelian, and A. Vega, "Structure and magnetism of cobalt clusters," Phys. Rev. B **67**, 174413 (2003).

[3] R. Gehrke, P. Gruene, A. Fielicke, G. Meijer, and K. Reuter, "Nature of Ar bonding to small Co_n^+ clusters and its effect on the structure determination by far-infrared absorption spectroscopy," J. Chem. Phys. **130**, 034306 (2009).

[4] J. Jalink, J. M. Bakker, Th. Rasing and A. Kirilyuk, "Channeling Vibrational Energy To Probe the Electronic Density of States in Metal Clusters," J. Phys. Chem. Lett. **6**, 750-754 (2015).

[5] S. Yang and M. B. Knickelbein, "Photoionization studies of transition metal clusters: Ionization potentials for Fe_n and Co_n," J. Chem. Phys. **93**, 1533 (1990).

[6] S. Datta, M. Kabir, S. Ganguly, B. Sanyal, T. Saha-Dasgupta, and A. Mookerjee, "Structure, bonding, and magnetism of cobalt clusters from first-principles calculations," Phys. Rev. B **76**, 014429 (2007).

[7] F. Aguilera-Granja, A. Vega, and L. C. Balbás, "A new family of star-like icosahedral structures for small cobalt clusters," Chem. Phys. **415**, 106 (2013).

[8] I. M. Billas, A. Châtelain and W. A. de Heer, "Magnetism from the atom to the bulk in iron, cobalt, and nickel clusters," Science **265**, 1682 (1994).

[9] S. Peredkov, M. Neeb, W. Eberhardt, J. Meyer, M. Tombers, H. Kampschulte and G. Niedner-Schatteburg, "Spin and Orbital Magnetic Moments of Free Nanoparticles," Phys. Rev. Lett. **107**, 233401 (2011).

[10] M. Niemeyer, K. Hirsch, V. Zamudio-Bayer, A. Langenberg, M. Vogel, M. Kossick, C. Ebrecht, K. Egashira, A. Terasaki, T. Möller, B. v. Issendorff and J. T. Lau, "Spin Coupling and Orbital Angular Momentum Quenching in Free Iron Clusters," Phys. Rev. Lett. **108** 057201 (2012).

[11] A. Cox, J. Louderback, and L. Bloomfield, "Experimental observation of magnetism in rhodium clusters," Phys. Rev. Lett. **71**, 923-926 (1993).

[12] A. Cox, J. Louderback, S. Apsel and L. Bloomfield, "Magnetism in 4d-transition metal clusters," Phys. Rev. B **49**, 12295-12298 (1994).

[13] L. Ma, R. Moro, J. Bowlan, A. Kirilyuk, and W. A. de Heer, "Multiferroic Rhodium Clusters," Phys. Rev. Lett. **113**, 157203 (2014).

[14] Y. Jinlong, F. Toigo, and W. Kelin, "Structural, electronic, and magnetic properties of small rhodium clusters," Phys. Rev. B **50**, 7915-7924 (1994).

[15] Z. Li, J. Yu, K. Ohno and Y. Kawazoe, "Calculations on the magnetic properties of rhodium clusters," J. Phys.: Condens. Matter **7**, 47-53 (1995).

[16] G. Harp, S. Parkin, W. O'Brien and B. Tonner, "Induced Rh magnetic in Fe-Rh and Co-Rh alloys using x-ray magnetic circular dichroism," Phys.

Rev. B **51**, 37-40 (1995).

[17] D. Zitoun, M. Respaud, M.-C. Fromen, M. Casanove, P. Lecante, C. Amiens, and B. Chaudret, "Magnetic Enhancement in Nanoscale CoRh Particles," Phys. Rev. Lett. **89**, 037203 (2002).

[18] M. Muñoz Navia, J. Dorantes-Dávila, D. Zitoun, C. Amiens, B. Chaudret, N. Jaouen, A. Rogalev, M. Respaud, and G. M. Pastor, "Tailoring the magnetic anisotropy in CoRh nanoalloys," App. Phys. Lett. **95**, 233107 (2009).

[19] H. K. Yuan, H. Chen, A. L. Kuang, B.Wu and J. Z.Wang, "Structural and magnetic properties of small 4d transition metal clusters: role of spin-orbit coupling," J. Phys. Chem. **116**, 11673-84 (2012).

[20] L. E. Díaz-Sánchez, J. Dorantes-Dávila and G. M. Pastor, "Local and chemical environment dependence of the magnetic properties of CoRh core-shell nanoparticles," Phys. Rev. B **88**, 134423 (2013).

[21] E. Berlanga-Ramírez , F. Aguilera-Granja, J. Montejano-Carrizales, A. Díaz-Ortiz, K. Michaelian and A. Vega, "Magnetism in segregated bimetallic CoRh nanoclusters," Physica B: Cond. Matt. **354**, 278-281 (2004).

[22] D. Dieleman, M. Tombers, L. Peters, J. Meyer, S. Peredkov, J. Jalink, M. Neeb, W. Eberhardt, Th. Rasing, G. Niedner-Schatteburg, and A. Kirilyuk, "Orbit and spin resolved magnetic properties of size selected [Co$_n$Rh]$^+$ and [Co$_n$Au]$^+$ nanoalloy clusters," Phys. Chem. Chem. Phys. **17**, 28372-28378 (2015).

[23] X. Xu, S. Yin, R. Moro, and W. de Heer, "Magnetic Moments and Adiabatic Magnetization of Free Cobalt Clusters," Phys. Rev. Lett. **95**, 237209 (2005).

[24] C. Dong and X. Gong, "Magnetism enhanced layer-like structure of small cobalt clusters," Phys. Rev. B **78**, 020409 (2008).

[25] J. Jalink, Ph.D. thesis, "Metal clusters: from geometric to electronic and magnetic properties", Radboud University, Nijmegen, The Netherlands (2014).

[26] F. W. Payne, W. Jiang, J. W. Emmert, J. Deng, and L. A. Bloomfield, "Magnetic structure of free cobalt clusters studied with Stern-Gerlach deflection experiments," Phys. Rev. B **75**, 094431 (2007).

[27] M. B. Knickelbein, "Magnetic moments of bare and benzene-capped cobalt clusters," J. Chem. Phys. **125**, 044308 (2006).

[28] K. Hirsch, V. Zamudio-Bayer, A. Langenberg, M. Niemeyer, B. Langbehn, T. Möller, A. Terasaki, B. v. Issendorff, and J. T. Lau, "Magnetic Moments of Chromium-Doped Gold Clusters: The Anderson Impurity Model in Finite Systems," Phys. Rev. Lett. **114**, 087202 (2015).

Appendix

In this section, the magnetic moments of all cluster species studied in this manuscript are shown.

Table 7.1: Total magnetic moments of V_n clusters. Values shown on Fig. 3.3.

Cluster	M_{exp} (μ_B)
V_3	1.25 ± 0.35
V_4	0.01 ± 0.24
V_5	0.78 ± 0.25
V_6	0.01 ± 0.25
V_7	0.86 ± 0.28
V_8	0.00 ± 0.25
V_9	0.83 ± 0.27
V_{10}	0.00 ± 0.25
V_{11}	0.91 ± 0.30
V_{12}	-0.02 ± 0.25
V_{13}	2.40 ± 0.94
V_{14}	0.00 ± 0.25
V_{15}	2.00 ± 0.89
V_{16}	0.02 ± 0.25
V_{17}	0.71 ± 0.23
V_{18}	0.01 ± 0.25
V_{19}	0.91 ± 0.30
V_{20}	0.00 ± 0.25
V_{21}	1.02 ± 0.33
V_{22}	1.44 ± 0.54
V_{23}	0.90 ± 0.29
V_{24}	-0.03 ± 0.35
V_{25}	0.68 ± 0.32
V_{26}	2.83 ± 0.93
V_{27}	0.78 ± 0.35
V_{28}	2.64 ± 0.96
V_{29}	0.78 ± 0.35
V_{30}	0.01 ± 0.35
V_{31}	0.91 ± 0.40
V_{32}	0.01 ± 0.35
V_{33}	5.58 ± 1.71
V_{34}	0.01 ± 0.35
V_{35}	0.84 ± 0.37

Table 7.2: Total magnetic moments of Nb_n clusters. Values shown on Fig. 3.14.

Cluster	M_{exp} (μ_B)
Nb_3	1.03 ± 0.35
Nb_4	0.10 ± 0.25
Nb_5	1.07 ± 0.35
Nb_6	0.00 ± 0.25
Nb_7	2.82 ± 0.94
Nb_8	0.00 ± 0.25
Nb_9	1.01 ± 0.33
Nb_{10}	0.00 ± 0.25
Nb_{11}	1.00 ± 0.33
Nb_{12}	0.00 ± 0.25
Nb_{13}	0.75 ± 0.24
Nb_{14}	0.00 ± 0.25
Nb_{15}	3.02 ± 0.84
Nb_{16}	-0.02 ± 0.25
Nb_{17}	1.05 ± 0.34
Nb_{18}	0.02 ± 0.25
Nb_{19}	0.56 ± 0.18
Nb_{20}	-0.01 ± 0.25
Nb_{21}	1.05 ± 0.34
Nb_{22}	1.23 ± 0.25
Nb_{23}	1.06 ± 0.35
Nb_{24}	0.03 ± 0.25
Nb_{25}	1.04 ± 0.34
Nb_{26}	0.03 ± 0.25
Nb_{27}	1.14 ± 0.37
Nb_{28}	1.39 ± 0.25
Nb_{29}	1.08 ± 0.35
Nb_{30}	0.08 ± 0.25
Nb_{31}	1.24 ± 0.41
Nb_{32}	0.11 ± 0.25

Table 7.3: Total magnetic moments of Ta_n clusters. Values shown on Fig. 3.20.

Cluster	M_{exp} (μ_B)
Ta_2	-0.01 ± 0.35
Ta_3	2.73 ± 0.99
Ta_4	-0.01 ± 0.39
Ta_5	2.45 ± 0.90
Ta_6	0.00 ± 0.34
Ta_7	2.16 ± 0.81
Ta_8	0.01 ± 0.29
Ta_9	1.69 ± 0.65
Ta_{10}	-0.01 ± 0.23
Ta_{11}	2.26 ± 0.84
Ta_{12}	0.08 ± 0.28
Ta_{13}	0.73 ± 0.34
Ta_{14}	0.02 ± 0.33
Ta_{15}	1.28 ± 0.52
Ta_{16}	0.03 ± 0.34

Table 7.4: Total magnetic moments of $Nb_n Co$ clusters. Values shown on Fig. 4.5.

Cluster	M_{exp} (μ_B)
$Nb_3 Co$	4.14 ± 1.35
$Nb_4 Co$	5.60 ± 2.13
$Nb_5 Co$	0.00 ± 0.12
$Nb_6 Co$	5.33 ± 2.17
$Nb_7 Co$	-0.01 ± 0.12
$Nb_8 Co$	1.08 ± 0.26
$Nb_9 Co$	2.37 ± 0.78
$Nb_{10} Co$	1.15 ± 0.38
$Nb_{11} Co$	1.91 ± 0.63
$Nb_{12} Co$	2.71 ± 0.89
$Nb_{13} Co$	2.16 ± 0.71
$Nb_{14} Co$	1.02 ± 0.26
$Nb_{15} Co$	0.08 ± 0.26
$Nb_{16} Co$	1.13 ± 0.32
$Nb_{17} Co$	0.21 ± 0.26
$Nb_{18} Co$	1.10 ± 0.36
$Nb_{19} Co$	-0.05 ± 0.36
$Nb_{20} Co$	1.13 ± 0.37
$Nb_{21} Co$	0.05 ± 0.36
$Nb_{22} Co$	0.89 ± 0.59
$Nb_{23} Co$	-0.06 ± 0.36

Table 7.5: Total magnetic moments of V_nCo clusters. Values shown on Fig. 4.14.

Cluster	M_{exp} (μ_B)
V_3Co	2.98 ± 0.97
V_4Co	0.83 ± 0.27
V_5Co	0.10 ± 0.26
V_6Co	0.85 ± 0.28
V_7Co	2.57 ± 0.84
V_8Co	0.81 ± 0.26
V_9Co	0.15 ± 0.26
V_{10}Co	0.96 ± 0.31
V_{11}Co	3.30 ± 1.08
V_{12}Co	0.98 ± 0.32
V_{13}Co	0.05 ± 0.26
V_{14}Co	1.08 ± 0.35
V_{15}Co	0.12 ± 0.26
V_{16}Co	0.98 ± 0.32
V_{17}Co	0.11 ± 0.26
V_{18}Co	1.00 ± 0.33
V_{19}Co	0.09 ± 0.26
V_{20}Co	0.97 ± 0.32
V_{21}Co	1.50 ± 0.49
V_{22}Co	0.98 ± 0.32
V_{23}Co	0.18 ± 0.26
V_{24}Co	0.91 ± 0.30
V_{25}Co	2.97 ± 0.97
V_{26}Co	0.95 ± 0.31
V_{27}Co	1.21 ± 0.39

Table 7.6: Total magnetic moments of V_nTb clusters. Values shown on Fig. 5.2.

Cluster	M_{exp} (μ_B)
V_3Tb	16.11 ± 4.34
V_4Tb	14.64 ± 4.21
V_5Tb	16.88 ± 4.54
V_6Tb	15.68 ± 5.41
V_7Tb	14.51 ± 5.42
V_8Tb	13.91 ± 4.79
V_9Tb	13.47 ± 5.37
V_{10}Tb	14.36 ± 5.24
V_{11}Tb	15.31 ± 5.58
V_{12}Tb	17.29 ± 5.99
V_{13}Tb	14.93 ± 5.12
V_{14}Tb	13.87 ± 4.77
V_{15}Tb	15.33 ± 5.98
V_{16}Tb	17.00 ± 6.06
V_{17}Tb	17.88 ± 6.90
V_{18}Tb	16.24 ± 7.92
V_{19}Tb	12.59 ± 6.29
V_{20}Tb	12.65 ± 5.85
V_{21}Tb	12.51 ± 3.30
V_{22}Tb	16.21 ± 6.84
V_{23}Tb	12.95 ± 5.88
V_{24}Tb	19.47 ± 7.19

Table 7.7: Total magnetic moments of $Nb_n Tb$ clusters. Values shown on Fig. 5.8.

Cluster	M_{exp} (μ_B)
$Nb_2 Tb$	13.80 ± 4.71
$Nb_3 Tb$	12.83 ± 4.38
$Nb_4 Tb$	18.30 ± 6.25
$Nb_5 Tb$	15.47 ± 5.28
$Nb_6 Tb$	17.77 ± 6.07
$Nb_7 Tb$	20.69 ± 7.06
$Nb_8 Tb$	20.65 ± 7.05
$Nb_9 Tb$	20.64 ± 7.05
$Nb_{10} Tb$	20.84 ± 7.11
$Nb_{11} Tb$	20.28 ± 6.92
$Nb_{12} Tb$	21.25 ± 7.25
$Nb_{13} Tb$	20.12 ± 6.87
$Nb_{14} Tb$	19.80 ± 6.76
$Nb_{15} Tb$	12.45 ± 4.25
$Nb_{16} Tb$	21.40 ± 7.30
$Nb_{17} Tb$	13.62 ± 4.65
$Nb_{18} Tb$	15.30 ± 5.22
$Nb_{19} Tb$	20.68 ± 7.06
$Nb_{20} Tb$	18.39 ± 6.28
$Nb_{21} Tb$	14.83 ± 5.06
$Nb_{22} Tb$	16.03 ± 5.47
$Nb_{23} Tb$	21.99 ± 7.51
$Nb_{24} Tb$	16.10 ± 5.49
$Nb_{25} Tb$	10.53 ± 3.59

Table 7.8: Total magnetic moments of Sm_nO clusters. Values shown on Fig. 6.5.

Cluster	M_{exp} (μ_B)
Sm_2O	1.49 ± 7.02
Sm_3O	-1.32 ± 5.99
Sm_4O	-0.75 ± 3.07
Sm_5O	1.60 ± 3.63
Sm_6O	9.42 ± 5.46
Sm_7O	9.98 ± 5.59
Sm_8O	3.65 ± 4.11
Sm_9O	5.90 ± 4.63
$Sm_{10}O$	4.22 ± 4.24
$Sm_{11}O$	3.35 ± 4.04
$Sm_{12}O$	5.56 ± 4.56
$Sm_{13}O$	11.39 ± 5.92
$Sm_{14}O$	10.29 ± 5.67
$Sm_{15}O$	2.56 ± 3.85
$Sm_{16}O$	4.94 ± 4.41
$Sm_{17}O$	3.32 ± 4.03
$Sm_{18}O$	4.56 ± 4.32

Table 7.9: Total magnetic moments per atom of Co_n clusters. Values shown on Fig. 7.4.

Cluster	M_{exp} (μ_B/atom)
Co_9	3.07 ± 0.83
Co_{10}	3.40 ± 0.93
Co_{11}	3.09 ± 0.84
Co_{12}	3.10 ± 0.84
Co_{13}	2.56 ± 0.70
Co_{14}	2.80 ± 0.76
Co_{15}	2.76 ± 0.75
Co_{16}	2.68 ± 0.73
Co_{17}	2.41 ± 0.66
Co_{18}	2.42 ± 0.66
Co_{19}	2.39 ± 0.65
Co_{20}	2.49 ± 0.68
Co_{21}	2.29 ± 0.62
Co_{22}	2.12 ± 0.58
Co_{23}	2.47 ± 0.67
Co_{24}	2.52 ± 0.69

Table 7.10: Total magnetic moments per atom of $Co_n Rh$ clusters. Values shown on Fig. 7.4.

Cluster	M_{exp} (μ_B/atom)
Co_9Rh	3.44 ± 0.94
$Co_{10}Rh$	2.81 ± 0.76
$Co_{11}Rh$	3.39 ± 0.92
$Co_{12}Rh$	3.23 ± 0.88
$Co_{13}Rh$	2.78 ± 0.76
$Co_{14}Rh$	2.59 ± 0.71
$Co_{15}Rh$	2.68 ± 0.73
$Co_{16}Rh$	2.76 ± 0.74
$Co_{17}Rh$	2.67 ± 0.73
$Co_{18}Rh$	2.53 ± 0.69
$Co_{19}Rh$	2.28 ± 0.62
$Co_{20}Rh$	2.38 ± 0.65
$Co_{21}Rh$	2.34 ± 0.64
$Co_{22}Rh$	2.39 ± 0.65
$Co_{23}Rh$	2.42 ± 0.66
$Co_{24}Rh$	2.41 ± 0.66

Table 7.11: Total magnetic moments per atom of $Co_n Rh_2$ clusters. Values shown on Fig. 7.4.

Cluster	M_{exp} (μ_B/atom)
Co_9Rh_2	3.11 ± 0.84
$Co_{10}Rh_2$	3.07 ± 0.83
$Co_{11}Rh_2$	2.14 ± 0.58
$Co_{12}Rh_2$	2.55 ± 0.69
$Co_{13}Rh_2$	2.28 ± 0.62
$Co_{14}Rh_2$	2.64 ± 0.72
$Co_{15}Rh_2$	2.23 ± 0.61
$Co_{16}Rh_2$	2.58 ± 0.70
$Co_{17}Rh_2$	2.56 ± 0.70
$Co_{18}Rh_2$	2.23 ± 0.61
$Co_{19}Rh_2$	2.39 ± 0.65
$Co_{20}Rh_2$	2.20 ± 0.60
$Co_{21}Rh_2$	1.81 ± 0.49
$Co_{22}Rh_2$	2.00 ± 0.55
$Co_{23}Rh_2$	2.17 ± 0.59
$Co_{24}Rh_2$	2.00 ± 0.54

Summary and outlook

What in Mathematics is an extremely simple calculation, 1+1=2, in Physics, if the ones are replaced by any physical property of free atoms, is not trivial at all, and the result is far from being 2, or twice the physical property relative to each atom. If the physical property is the magnetic moment, the result can be even smaller for the sum of both atoms, the dimer, than for each single atom left alone. And more interestingly if one keeps adding atoms, the changes due to each single addition can not be predicted according to what was found with the previous addition. This interesting behavior reveals itself in many different phenomena. For instance, the orbital magnetic moments are decreased strongly due to the electronic Coulomb interaction. Further the discrete atomic levels merge into bands when the number of atoms is large enough. The previously mentioned dimer is just the first species in the long row of so called atomic clusters. In this thesis we studied how the magnetic properties evolve for the smallest clusters, from 2 atoms to tens of them. Since the clusters are the intermediate link between atoms and the bulk matter, the properties are a mixture of both. An introduction to the Physics of clusters is given in Chap. 1.

In order to study the magnetic properties of such small clusters experimentally, the performance of the setup is essential. The optimization of it was the first goal of this thesis, since the ratio signal to noise was relatively low. To improve signal, the introduction of a new time of flight mass spectrometer (TOFMS) which includes a flying tube was required. It allowed to achieve a better resolution while keeping a reasonable sensitivity which allows to distinguish peaks within few atomic masses distance, especially for the smaller sizes. Further the design of a new and more powerful magnet (larger magnetic gradient and field), was required in order to be able to achieve larger deflections so that small magnetic moments of relatively large clusters could be detected. This was extremely useful to be able to detect the different features found in Chap. 3, since deflections at 1.2 T did not show 3 or 2 peaks distinguishable by eye without a fit. Similarly, this relatively large magnetic field assisted to study Sm_nO in Chap. 6. The performance and the calibrations of both the time of flight and the magnet together with the source and every other single part of the setup are described in details in Chap. 2.

The second and main goal of this thesis was to study the magnetic properties of transition metal and rare earth clusters with strong focus on doping. Like this, in Chap. 3 we studied the magnetic properties of V, Nb and Ta clusters. The results show the alternation of non-magnetic behavior for the majority of even-numbered clusters while weak magnetism is found for odd-numbered ones. Interestingly, not only the magnetic moments were found to depend on the number of atoms but also the coupling between the magnetic moments and the cluster's lattice. This coupling was found to strongly depend on the carrier gas pressure, the shape

of the nozzle and the volume of the formation chamber. Doping such structures with a magnetic impurity was the aim of Chaps. 4 and 5. In Chap. 4 we used a transition metal as impurity, Co, which was proven to be incapable of inducing any magnetism in the both hosts, V and Nb. Surprisingly, Nb_5Co is completely non-magnetic, while Nb_6Co has a magnetic moment of 5 μ_B which upon gaining an additional atom becomes again non-magnetic. We demonstrated that this is due to the hybridization of the 3d electrons of Co, which in turn are responsible for its magnetic properties; this means that when the hybridization is large, magnetism is weak or non-existing and when hybridization is low the magnetic moments are at least 3 μ_B. Further we studied the geometry by means of infrared spectroscopy experiments and then compared with the calculation of the vibrational spectra by means of the density functional theory (DFT) implementation of the Vienna ab initio simulation package (VASP). In Chap. 5, we tried an impurity of different origin, Tb, whose 4f electrons responsible of its magnetic properties are much more localized and turned out to be able not only to retain such properties when placed within V and Nb as host, but also to be able to induce spin polarization on both hosts. In Chap. 6 we tried to study the magnetic properties of Sm_n clusters, since the atom is non magnetic while bulk Sm is magnetic. The transition was predicted for n>8. Only oxygen doped samarium could be found, thus we studied their magnetic properties, finding a strong dependence on size, but no transition at n = 8. In the last chapter of this thesis, Chap. 7, we studied the opposite of what was done in Chaps. 4 and 5, i.e. to dope a magnetic material, Co, with a non-magnetic impurity, since the large spin-orbit coupling of rhodium could improve the magnetic properties of Co clusters. However the results showed that the impact of such doping is very low and that for the majority of sizes, the magnetic moments decrease upon doping.

We believe that the performance of the setup can still be improved.

Further, in order to achieve a better understanding of the magnetic properties in clusters it would be interesting to be able to pump vibrational and rotational energy levels by means of infra red light, this is to couple the setup with the Free Electron Laser for Infrared eXperiments (FELIX). This would allow to see how such excitations affect the deflections. This would provide a better understanding of the magnetic properties for clusters.

Samenvatting en Vooruitblik

In de wiskunde is 1+1=2 een extreem makkelijke berekening. Een dergelijke berekening is in het algemeen echter verre van triviaal in de natuurkunde als we de enen vervangen door fysische eigenschappen . Bijvoorbeeld als twee dezelfde magnetische atomen bij elkaar gebracht worden, hoeft het totale magnetische moment van het ontstane dimeer helemaal niet tweemaal zo groot te zijn als dat van het individuele atoom. Het kan kleiner, maar ook groter zijn geworden. Nog interessanter wordt het als we dit proces van atomen toevoegen blijven blijven voortzetten. In het algemeen kan het resultaat van toevoegen van een atoom niet simpelweg geëxtrapoleerd worden van de verandering die toevoeging van het vorige atoom tot gevolg had. Dit interessante gedrag kan berusten vele verschillende fenomenen. Bijvoorbeeld het orbitaal moment kan sterk afnemen door interacties met andere atomen. Verder veranderen de discrete atomaire energieniveaus in banden naarmate het systeem meer en meer atomen bevat.

Het al kort vernoemde dimeer is het kleinste zogenaamde atomaire cluster. In dit proefschrift bestuderen we hoe de magnetische eigenschappen zich ontwikkelen van het dimeer tot clusters van ongeveer tien atomen groot. Aangezien het regime van de clusters zich tussen dat van de atomen en de vaste stof bevindt, zal het eigenschappen van beide kunnen hebben. In hoofdstuk 1 wordt een inleiding gegeven over de fysica van clusters.

Om de magnetische eigenschappen van zulke kleine clusters te kunnen bestuderen, moesten we de signaal-ruisverhouding van de bestaande experimentele opstelling verbeteren. Om deze verhouding te verbeteren hebben we een nieuwe vluchttijdsmassaspectrometer (time-of-flight-mass-spectrometer, TOFMS) gebouwd. Met deze nieuwe TOFMS kunnen we clusters met een massaverschil van slechts enkele atomische massa-eenheden (amu) onderscheiden. Naast de TOFMS hebben we ook een nieuwe en sterkere magneet ontworpen, met zowel een grotere gradiënt als een hogere veldsterkte. Dit is met name nodig om zware clusters met een klein magneetveld te kunnen detecteren. Voorbeelden hiervan zijn V, Nb en Ta clusters, zoals beschreven in hoofdstuk 3. Een ander voorbeeld is dat van de SmnO clusters die worden bestudeerd in hoofdstuk 6. Een uitgebreide beschrijving van de prestaties en kalibraties van de TOFMS, de magneet en de gehele experimentele opstelling wordt gegeven in hoofdstuk 2.

Naast het verbeteren van de opstelling was het hoofddoel van dit proefschrift het bestuderen van de magnetische eigenschappen van overgangsmetalen en zeldzame aarde clusters met name onder invloed van doping. Voor de groep van de overgangsmetalen V, Nb en Ta vonden we voor de meeste clusters met een even aantal atomen dat ze niet magnetisch zijn, terwijl voor een oneven aantal atomen deze clusters zwak magnetisch zijn. Een andere interessante vondst is dat naast het magnetische moment ook de manier waarop het magnetisch moment gekoppeld is met het rooster afhangt van de clustergrootte. Veder bleek deze

koppeling met het rooster af te hangen van de druk van het 'draaggas', de vorm van de uitlaat en het volume van de kamer waar de clusters gevormd worden.

Het toevoegen van magnetische onzuiverheden (doping) aan V en Nb clusters wordt in de hoofdstukken 4 en 5 bestudeerd. In hoofdstuk 4 gebruikten we het magnetische overgangsmetaal Co als onzuiverheid. Het bleek dat Co niet in staat is om alle V en Nb clusters magnetisch te maken. Verrassend is verder dat Nb_5Co niet magnetisch is terwijl Nb_6Co een magnetisch moment van maar liefst 5 μ_B bezit. We hebben aangetoond dat dit het gevolg is van de verschillende hybridisatie van het Co atoom met de Nb gastheer in Nb_5Co en Nb_6Co. In het algemeen geldt dat magnetisme zwak of afwezig is als de hybridisatie met de gastheer sterk is. Omgekeerd is het magnetisme sterk als de hybridisatie zwak is. Naast het magnetisme hebben we ook de geometrie van de clusters bestudeerd aan de hand van infrarood spectroscopie in combinatie met dichtheidsfunctionaaltheorie (density-functional theory, DFT) berekeningen, waarvoor het Vienna ab initio simulation package (VASP) softwarepakket is gebruikt.

In hoofdstuk 5 hebben we een ander soort magnetische onzuiverheid, Tb, aan de Nb clusters toegevoegd. Tb is een zeldzame aarde atoom dat gekarakteriseerd wordt door hun sterk gelokaliseerde 4f elektronen. In het geval van Tb zorgen deze 4f elektronen voor een sterk gelokaliseerd magneetveld. Het blijkt dat Tb zijn magnetische eigenschappen grotendeels behoudt als het toegevoegd wordt aan de V en Nb clusters. Daarnaast induceert het nog een spin moment in V and Nb gastheer.

In hoofdstuk. 6 hebben we in eerste instantie geprobeerd pure Sm clusters te bestuderen. Aangezien een Sm atoom niet magnetisch is en de vaste stof van Sm wel, is het interessant om te weten bij welke grootte Sm clusters magnetisch worden. Op grond van theoretische berekeningen is voorspeld dat Sm clusters bij een grootte van 8 atomen magnetisch worden. Door de sterke oxidatie van Sm clusters konden pure Sm clusters helaas niet bestudeerd worden, maar de deels geoxideerde Sm_n clusters lieten een interessant magnetisch gedrag zien als functie van hun grootte, maar geen overgang op n = 8.

In het laatste hoofdstuk van dit proefschrift, hoofdstuk 7, hebben we het omgekeerde gedaan van wat beschreven is in hoofdstukken 4 en 5. In plaats van een niet-magnetisch systeem te doperen met een magnetisch atoom, hebben we nu een magnetisch system gedopeerd met een niet-magnetisch atoom. Door Rh te kiezen als onzuiverheid wilden we de invloed van de sterke spin-baan-koppeling van dit atoom in een Co cluster gastheer bestuderen. Het bleek dat deze invloed in de praktijk erg klein is en dat in het algemeen de magnetische momenten wat afnemen.

Voor de toekomst ben ik van mening dat de prestaties van de gebruikte experimentele set-up nog verder verbeterd kunnen worden.

Tot slot, om een beter begrip van de magnetische eigenschappen van de clusters te krijgen, is het interessant om de mogelijkheid te hebben om zowel vibrationele en rotationele energietoestanden te kunnen aanslaan met infrarood licht. Dit zou bijvoorbeeld kunnen door de gebruikte experimentele opstelling te

verbinden met de vrije elektronenlaser FELIX. Dergelijke experimenten zouden inzicht kunnen geven in de invloed van vibrationele en rotationele excitaties op de mate van magnetische deflectie.

List of publications

A. Diaz-Bachs, M. I. Katsnelson, and A. Kirilyuk, "Kramers degeneracy and relaxation in vanadium, niobium and tantalum clusters," New J. Phys. **20**, 043042 (2018).

A. Diaz-Bachs, L. Peters, R. Logemann, V. Chernyy, J. M. Bakker, M. I. Katsnelson, and A. Kirilyuk, "Magnetic properties of Co-doped Nb clusters," Phys. Rev. B **97**, 134427 (2018).

A. Diaz-Bachs, L. Peters, and A. Kirilyuk, "Magnetic properties of oxygen doped samarium clusters," J. Phys.: Condens. Matter **31**, 074002 (2019).

V. Chernyy, R. Logemann, A. Diaz-Bachs, D. M. Kiawi, J. Jalink, A. Kirilyuk, and J. M. Bakker, "The geometric structure and magnetism of V_n and Fe_n clusters (n = 12, 13)," submitted for publication.

Curriculum Vitae

Albert Diaz Bachs
born 28 November 1983
in Barcelona, Catalunya

2012 BSc in Physics
Universitat de Barcelona, Faculty of Physics, Barcelona

2013 MSc in Nanoscience and nanotechnology
Universitat de Barcelona, Faculty of Physics, Barcelona

2013-2018 PhD Candidate
Radboud Universiteit, Faculty of Science, Nijmegen, The Netherlands
Supervisor: Prof. dr. Andrei Kirilyuk